The performance characterization of carbazole/dibenzothiophene derivatives in modern OLEDs

Dissertation

zur Erlangung des akademischen Grades

doctor rerum naturalium

(Dr. rer. Nat.)

im Fach Physik

eingereicht an der

Mathematisch-Naturwissenschafrlichen Fakultät

der Humboldt-Universität zu Berlin

Von

M.Sc. Junming Li

Präsident der Humboldt-Universität zu Berlin

Prof. Dr.-Ing. Dr. Sabine Kunst

Dekan der Mathematisch-Naturwissenschaftlichen Fakultät

Prof. Dr. Elmar Kulke

Gutachter: 1. Prof. Norbert Koch

2. Prof. Christoph T. Koch

3. Prof. Liangsheng Liao

Tag der mündlichen Prüfung: 19.12.2016

Abstract

A particularly interesting organic light-emitting diodes (OLEDs) design adopts a host-guest strategy by dispersing a small amount of highly efficient emitter (the guest) into an appropriate transport matrix (the host). The host is utilized to transfer excitons to the emitter and to prevent triplet exciton quenching, thus high device performance can be achieved.

The present thesis focuses on the relationship between the molecular structure and opto-electrical properties of carbazole/dibenzothiophene derivatives. The investigation encompasses seven of these derivatives for the host, in which the carbazole unit acts as a donor and the dibenzothiophene as an acceptor while they are linked through phenyl spacer(s). This choice of host materials enables to assess the impact of extended phenyl spacers and different acceptor to donor molar ratios. It was found that decreasing the phenyl spacer length enhances the device performance due to the larger both hole and electron densities in the emitting layer; and a 1:1 carbazole to dibenzothiophene ratio is favorable for device performance, since it balances the charge carriers in the emitting layer. Using these host materials, the work presented in this thesis demonstrates high-performance blue FIrpic-based phosphorescent OLEDs (PhOLEDs) and green 4CzIPN-based thermally activated delayed fluorescence (TADF) OLEDs. The blue PhOLEDs and green TADF OLEDs with *m*DCP showed efficiencies of 43 cd/A (18.6%) and 66 cd/A (21%), respectively.

Keywords: phosphorescent organic light emitting diodes, thermally activated delayed fluorescence organic light emitting diodes, carbazole, dibenzothiophene, host materials.

Kurzfassung

Ein vielversprechendes Design für organische lichtemittierende Dioden (OLEDs) verwendet eine Wirt-Gast-Strategie durch Dispergieren einer kleinen Menge eines hocheffizienten Emitters (der Gast) in eine passende Transportmatrix (der Wirt). Die Aufgabe des Wirts ist den Exzitonentranport zum Emitter sicherzustellen und den Zerfall von Triplet-Exzitonen zu verhindern, und damit eine hohe Bauteilperformance zu erreichen.

Die vorliegende Arbeit konzentriert sich auf die Beziehung zwischen Molekülstruktur und optoelektrischer Eigenschaften von Carbazol/Dibenzothiophen-Derivaten. Die Untersuchung umfasst sieben dieser Derivate für den Wirt, bei denen die Carbazoleinheit als Donator und die Dibenzothiopheneinheit als Akzeptor fungiert, wobei beide durch einen oder mehrere Phenylabstandshalter verbunden sind. Diese Wahl der Wirtsmaterialien erlaubt es den Einfluss der erweiterten Phenylabstandshalter und der unterschiedlichen molaren Verhältnisse von Akzeptor zu Donator zu untersuchen. Es ergab sich, dass eine kürzere Phenylabstandshalterlänge die Bauteilperformance durch eine größere Löcher- und Elektronendichte in der Emitterschicht verbessert; und ein 1:1 Carbazol-zu-Dibenzothiophen-Verhältnis der Bauteilperformance zuträglich ist, da es zu einem Ladungsträgergleichgewicht in der Emitterschicht führt. Diese Arbeit zeigt, unter Verwendung dieser Wirtsmaterialien, blaue FIrpic-basierte phosphoreszierende OLEDs (PhOLEDs) und grüne 4CzIPN-basierte thermisch aktivierte verzögerte Phosphoreszenz (TADF) OLEDs. Die blauen PhOLEDs und grünen TADF OLEDs mit *m*DCP zeigten Effizienzen von 43 cd/A (18.6%) beziehungsweise 66 cd/A (21%).

Stichwörter: phosphoreszierende organische lichtemittierende Dioden, thermisch aktivierte verzögerte Phosphoreszenz organische lichtemittierende Dioden, Carbazol, Dibenzothiophen, Wirtsmaterialien

Table of Contents

Abbreviations

DSC	differential scanning calorimetry
EA	electron affinity
EML	emission layer
EQE	external quantum efficiency
ETL	electron transport layer
EIL	electron injection layer
FWHM	full-width-at-half-maximum
HIL	hole injection layer
HOMO	highest occupied orbital
HTL	hole transport layer
IE	ionization energy
LUMO	lowest unoccupied molecular orbital
OLEDs	organic light emitting diodes
PhOLEDs	phosphorescent organic light emitting diodes
PL	photoluminescence
SCLC	space charge limited current
TADF	thermally activated delayed fluorescence
TGA	thermogravimetric analysis
UPS	ultraviolet photoelectron spectroscopy
UV-Vis	ultraviolet and visible
XPS	X-ray photoelectron spectroscopy
E_{vac}	vacuum level
S_0	the ground state

S_1	the lowest excited singlet state
T_1	the lowest excited triplet state
η_{ext}	external quantum efficiency
η_{int}	internal quantum efficiency

List of Chemical Names

4CzIPN	1,2,3,5-tetrakis(carbazol-9-yl)-4,6-dicyanobenzene
Al	aluminum
Ag	silver
CBP	4,4′-bis(9-carbazolyl)-2,2′-dimethyl-biphenyl
HAT-CN	hexaazatriphenylene hexacarbonitrile
FIrpic	iridium (III) bis [4, 6-di-fluorophenyl-pyridinato-N, $C^{2'}$] picolinate
ITO	indium tin oxide
Liq	lithium quinolate
MoO_3	molybdenum oxide
*m*BPDBT	3,3'-bis(dibenzo[b,d]thiophen-4-yl)-1,1'-biphenyl
*m*CBP	3,3-di(9H-carbazol-9-yl) biphenyl
*m*DCBP	9-(3'-(dibenzo[b,d]thiophen-4-yl)-[1,1'-biphenyl]-3-yl)-9H-carbazole
*m*DCP	9-(3-(dibenzo[b,d]thiophen-4-yl)phenyl)-9H-carbazole
*m*DCTP	9-(3"-(dibenzo[b,d]thiophen-4-yl)-[1,1':3',1"-terphenyl]-3-yl)-9H-carbazole
*m*D2CBP	9-(3',5'-bis(dibenzo[b,d]thiophen-4-yl)-[1,1'-biphenyl]-3-yl)-9H-carbazole
*m*DC2BP	9,9'-(3'-(dibenzo[b,d]thiophen-4-yl)-[1,1'-biphenyl]-3,5-diyl)bis(9H-carbazole)
PEIE	polyethylenimine ethoxylated
TAPC	di-[4-N,N-ditolyl-amino-phenyl] cyclohexane
TCTA	4,4',4"-tris(N-carbazolyl)-triphenylamine
TmPyPB	tetra(m-pyrid-3-yl)phenyl-[1,1']-biphenyl

Chapter 1

Introduction

Electroluminescence is a phenomenon characterized by the luminescence generated by electrical excitation. Electroluminescence from an organic semiconductor was first reported in the 1950s via a cellulose film doped with acridine orange [1], and was developed further using an anthracene single crystal sandwiched between two electrodes in the 1960s [2]. This investigation involved the basic processes of organic electroluminescence: charge carrier injection from two electrodes, charge carrier transporting, exciton formation in the recombination zone, and radiative decay of the exciton. However, there was no possible application of this technology due to its poor device performance. Advancement in organic electroluminescence was spurred on in 1987 by Tang and Van Slyke, who demonstrated an efficient organic light emitting diodes (OLEDs) with a single heterojunction structure [3]; another notable breakthrough was the discovery of electroluminescence from polymer materials at the University of Cambridge in 1990 [4]. After that, OLEDs had shown considerable potential for flat panel displays and lighting source applications due to several advantages over other similar techniques, including low power consumption, low weight, high luminous efficiency, full-color capability, wide viewing angle, high contrast, and the use of non-toxic metals. There are several OLEDs flat-panel displays and lighting products available in the current market. For example, since 2014, Samsung and Apple have both used OLEDs displays in the Galaxy Note Edge and Apple Watch, respectively. In 2015, LG Display unveiled a 55-inch OLED TV that was only 1 mm thick and weighs only 1.9 kg. Despite the remarkable progress that has been made, there are still many further research may lead to further improvement of OLEDs performance.

Under the electrical excitation in OLEDs, the external quantum efficiency (EQE) is expressed as follows [5]:

$$\eta_{ext} = \eta_{\mathrm{C}}\eta_{\mathrm{int}} = \eta_{\mathrm{C}}\times r_{\mathrm{st}}\times\Phi_{\mathrm{f}}\times\gamma \quad (1.1)$$

where η_{ext} is the external quantum efficiency, defined as the number of emitted photons divided by the number of injected charge carriers; η_{C} is the fraction of photons that can escape from the device (typically 20-30% with flat glass substrates) [6-8]; η_{int} is the internal quantum efficiency, defined as the number of photons produced within the device divided by the injected charge carriers; r_{st} is the probability that radiative decay will occur; and Φ_f is the fluorescent quantum efficiency or the fraction of excitons that can undergo radiative decay. In a high performance organic emitter, Φ_f can approach nearly 100%. And γ is the probability that holes and electrons recombine to form excitons to maximize γ (i.e. ensure a highly efficient device), an appropriate balance between two types of charge carriers is necessary. That said, each of these parameters represents an individual route toward device optimization (as will be discussed later in this thesis).

Under electrical excitation, charge recombination in the emitting layer produces singlet and triplet excitons with a ratio of 1:3, i.e., 25% singlet excitons and 75% triplet excitons. According to the spin statistics, conventional fluorescent OLEDs can only harvest singlet excitons (25% of the formed excitons). All triplet excitons (75% of the formed excitons) decay non-radiatively. Thus the maximum internal quantum efficiency of conventional fluorescent OLEDs is only 25%.

Several approaches have been proposed to harvest the triplet excitons to improve OLEDs efficiency. Efficiency can be significantly increased by introducing of transition heavy metal atoms (usually platinum, osmium, or iridium) into organic molecules in phosphorescent OLEDs (PhOLEDs) [9-11]. For phosphorescent emitters (phosphors), the singlet excitons can be fast and efficiently converted to triplet excitons via intersystem crossing process, then all triplet excitons can exhibit radiative decay to the ground state ($T_1 \rightarrow S_0$ transition) due to the spin-orbital coupling effect of the heavy central metal [11]. Another successful route to harvesting triplet excitons is based on the thermally activated delayed fluorescence (TADF) mechanism. Generally, in TADF emitters, the triplet excitons can be converted into singlet excitons via thermally activated reverse intersystem crossing due to small electron exchange energy (singlet-triplet splitting), then all singlet excitons are possible to emit either prompt fluorescence or delayed fluorescence [12]. Both phosphors and TADF emitters are able to approach an internal quantum efficiency of 100% [9, 13-15].

Generally, the efficient PhOLEDs and TADF OLEDs contain a doped emitting layer, which consists of a dopant that is dispersed in a suitable host matrix to avoid unwanted triplet exciton quenching, such as: triplet-triplet annihilation, triplet-polaron quenching and concentration self-quenching [16-18]. Meanwhile, the high energy host donors transfer the excitons to the high efficiency dopant acceptors through the Förster or Dexter mechanism, resulting in highly efficient emission from the dopant. To this effect, the host materials play a key role in the overall performance of the OLEDs.

In principle, an ideal host material possesses certain criteria: first, as the major component of the emitting layer, the highest occupied orbital (HOMO) and lowest unoccupied molecular orbital (LUMO) levels of host materials must be matched with the adjacent layers and emitters to ensure effective charge injection. The HOMO level of the host materials should be deeper than that of the emitters, while the LUMO level of the host materials should be shallower than that of the emitters. Then, both the singlet or triplet energies of the host should be higher than that of the dopant to guarantee efficient forward energy transfer from the host to the dopant and to confine the excitons on the dopant. For the host materials in blue OLEDs, triplet energy (T_1) higher than 2.6 eV is preferred because the lowest triplet energy of a typical sky blue triplet emitter is 2.6 eV. In addition, good charge carrier transport properties are another important consideration for host materials since positive and negative charge carriers are required to be balanced in OLEDs to secure high device efficiency and low device efficiency roll-off. In addition to these host material criteria, good thermal stability, simple structure, and ease of preparation are necessary for industrial manufacture. Developing host materials which can maximize the light-emitting performance of phosphors and TADF emitters, thus, is a rather popular research object.

The host materials for PhOLEDs and TADF OLEDs have several requirements in common, however, the two different emitters have different HOMO/LUMO levels and singlet/triplet energies, which make it challenging to develop highly efficient PhOLEDs and TADF OLEDs with the same host material. In the search for such high-efficiency host materials, organic chemists have focused on a limited range of units. In terms of the classic hole transporting host, carbazole is an important constructing unit in host material design since the report of 4,4′-bis(9-carbazolyl)-2,2′-dimethyl-biphenyl (CBP) [19]. The strong electron donating nature endows the carbazole derivatives with decent hole mobility, and the T_1 of carbazole is 3.0 eV, leaving several possibilities for structural modification. To obtain high triplet energy for blue hosts, carbazole derivatives are given fewer conjugative configurations such as twist linkage or non-

conjugative linkage [20-28]. Recently, another heterocyclic unit similar to carbazole, dibenzothiophene was utilized for constructing host material. It also has high T_1 (3.04 eV), like carbazole, but less electron donating capability. Dibenzothiophene containing host materials have more neutral molecular structure compared to carbazole derivatives, exhibit high triplet energies (> 2.7 eV), and have shown excellent device performance in PhOLEDs and TADF OLEDs [29-33].

This thesis focuses mainly on the differences in physical properties between carbazole and dibenzothiophene units and the structure-property relationships of carbazole/dibenzothiophene derivatives, including thermal stability, photo-physical properties, electrical properties, and device performance in blue PhOLEDs and TADF OLEDs.

The remainder of this thesis is organized as follows. Chapter 2 contains a review of the basic physics of organic semiconductor materials, including the excited states in organic molecular and inter-molecular energy transfer, which are critical for a comprehensive understanding of this work. The history and general device physics of OLEDs are then reviewed, followed by a discussion on the two kinds of high-performance OLEDs mentioned above, PhOLEDs and TADF OLEDs.

In Chapter 3, the principles of the experimental methods (thermal vacuum evaporation and spin coating) are described. Additional experimental analysis methods and facilities such as differential scanning calorimetry (DSC), thermogravimetric analysis (TGA), photoluminescence (PL) spectroscopy, ultraviolet and visible (UV-Vis) absorption spectroscopy, and transient photoluminescence decay (transient PL decay) are also covered. The experimental setups, sample preparation procedures, and data processing procedures are explained. Furthermore, the materials used in this work (including organic materials, electrode, and substrates) are outlined at the end of this chapter.

Chapter 4 presents and discusses the experimental results. This chapter is divided into three parts corresponding to three different host molecule systems. In Chapter 4.1, a high performance host material, 9-(3'-(dibenzo[b,d]thiophen-4-yl)-[1,1'-biphenyl]-3-yl)-9H-carbazole (*m*DCBP), which combines a strong electron-donating carbazole moiety and a weaker electron-donating dibenzothiophene moiety was investigated; its thermal, photophysical and electrical properties were characterized in detail as well as the device performance of blue PhOLEDs and green TADF OLEDs based on it. All of the characterizations were comparatively analyzed with corresponding carbazole or

dibenzothiophene counterparts bearing the same molecular configuration with well-established properties.

Chapter 4.2 discusses how the linking spacer between carbazole and dibenzothiophene moieties affect their optical and electrical properties. The thermal, photophysical, and electrical properties two new host materials are comprehensively investigated: 9-(3-(dibenzo[b,d]thiophen-4-yl)phenyl)-9H-carbazole (*m*DCP) and 9-(3"-(dibenzo[b,d]thiophen-4-yl)-[1,1':3',1"-terphenyl]-3-yl)-9H-carbazole (*m*DCTP), with carbazole and dibenzothiophene groups connected by extended phenyl spacers. Thermal stability increased with the extended phenyl spacer while photophysical properties were unaffected. The device performance of blue PhOLEDs and green TADF OLEDs based on both materials were detailed investigated and good device performance were obtained. With the extended phenyl spacer, the device performance slightly decreased.

Chapter 4.3 elucidates the structure-function relationship of the number and ratio of carbazole to dibenzothiophene moieties. Two host materials are investigated: 9-(3',5'-bis(dibenzo[b,d]thiophen-4-yl)-[1,1'-biphenyl]-3-yl)-9H-carbazole (*m*D2CBP) and 9,9'-(3'-(dibenzo[b,d]thiophen-4-yl)-[1,1'-biphenyl]-3,5-diyl)bis(9H-carbazole) (*m*DC2BP), with different carbazole to dibenzothiophene groups ratios connected by biphenyl spacers. Their thermal, photophysical and electrical properties were characterized in detail. And gain, the device performance of blue PhOLEDs and green TADF OLEDs based on them were characterized in detail. A 1:1 ratio of carbazole to dibenzothiophene moieties in this series of host materials resulted in the best performance of PhOLEDs and TADF OLEDs.

Chapter 5 provides a summary of this work as well as a brief discussion on the outlook of this field and possible further research directions.

Chapter 2

Fundamentals

This chapter introduces the physical fundamentals necessary for this thesis. First, a brief introduction into the basic physics of small molecule organic semiconductors is given; the basic working principles of organic light emitting diodes are then presented, followed by an illustration of two notable types of high-performance OLEDs: PhOLEDs and TADF OLEDs.

2.1 Basic physics of organic semiconductors

Organic semiconductors have garnered a great deal of research interest in developing efficient opto-electronic devices, as they have been shown to play a major role in overall device performance. There are two classes of organic semiconductors: low molecular weight materials and polymers. The process for fabricating thin films differs based on which class of materials are utilized: thermal evaporation technique in a vacuum chamber is common for low molecular weight material deposition, while spin coating and print techniques are common for polymers [34].

In general, the molecular of these materials are mainly comprised of carbon atoms and the chemical bonds are mainly determined by the electronic configuration of the basis atomic carbon in the ground state [34]. In addition to carbon, other frequently employed heteroatoms are sulphur, nitrogen, and oxygen. A carbon atom has six electrons in the ground state ($1s^2 2s^2 2p^2$), two of them are in an inner core shell and other four are in an outer shell. Only the electrons in the outer *2s* and *2p* orbitals are the valance electrons which can form hybrid orbitals sp^3 ($1s^2 2s^2 2p_x p_y p_z$), sp^2, and *sp* [35].

Generally, carbon-carbon bonds in the organic molecules are either described as σ-bonds or π-bonds [36]. A σ-bond resulting from the formation of a molecular orbital by the end-to-end overlap of atomic orbitals and a π-bond resulting from the formation of a molecular orbital by side-to-side overlap of atomic orbitals lie along a plane perpendicular to a line connecting the nuclei of the atoms. This is exemplified in Figure 2.1 with an example ethene ($H_2C{=}CH_2$), in which two carbon atoms are linked by one σ-bond and one π-bond.

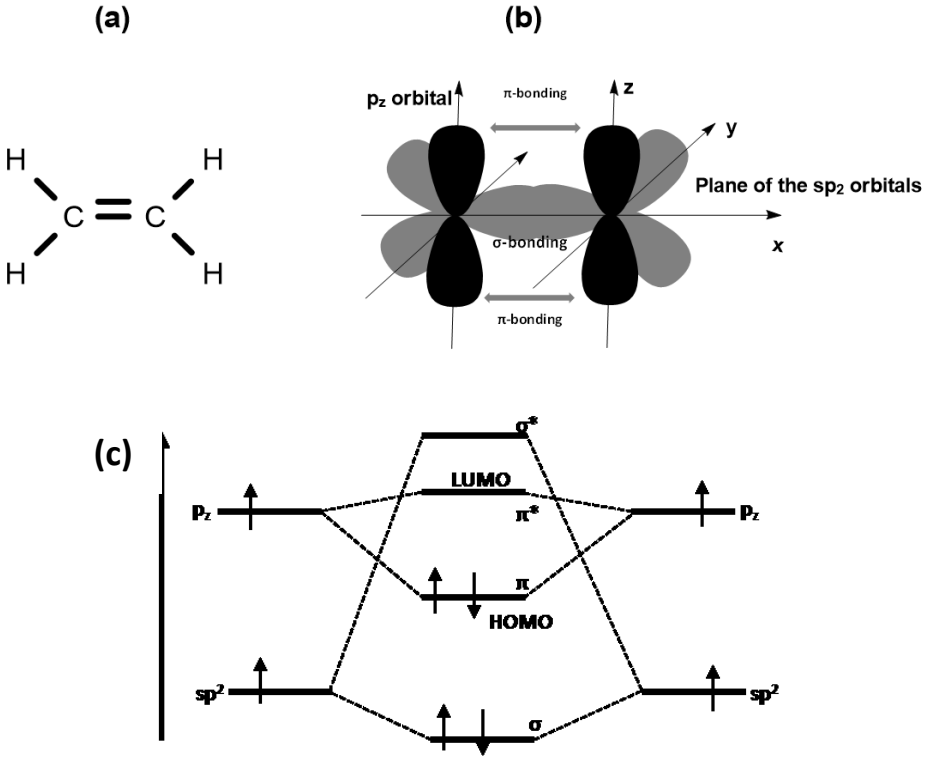

Figure 2.1: (a) Molecular structure; (b) illustration of σ- and π- bonds; and (c) energy levels in a double-bonded ethane molecule, adopted from the literature [36].

Due to the strong overlap, σ bonds generally make stronger chemical bonds than π-bonds. The delocalized electron clouds mainly above and below the plane of the atoms form the π-bond. Negatively charged π-clouds on either side of the symmetry plane are compensated by the positive charges of the atomic nuclei in the molecular plane. As a result, there are two opposite dipoles pointing toward the centered molecular plane canceling the dipole moment. This results in quadrupolar and higher order moments. In ground states, all orbitals are fully filled with electrons up to the HOMO level, and all orbitals are empty from the lowest LUMO level. Thus, the HOMO and LUMO levels are given by π and π*, respectively [37]. For organic molecules, the σ bonds are the stronger chemical bonds which predominantly determine the chemical properties, while the delocalized π electron system is mainly responsible for the electrical and optical properties of the materials [34, 38].

2.1.1 Excited states in organic molecules

By the excitation (e.g., optical excitation) of the organic molecule, an electron from the HOMO level is lifted into the LUMO level, leaving a positively charged hole in the HOMO level. The electron and hole located on same molecule form a Coulomb-bound pair, described

as an exciton [39]. Due to weak intermolecular van der Waals forces and strong Coulomb coupling, these excitons are strongly localized in a single molecule as Frenkel exciton and with a binding energy of 0.1 eV to 1 eV [38-41]. Excitons can also be formed by the recombination of electrons and holes under electrical excitation, where electrons and holes approach the HOMO and LUMO levels of molecules, respectively.

Both electrons and holes have a spin quantum number of $s=1/2$, which leads to a total exciton spin of S=0 (antiparallel spins) or S=1 (parallel spins). According to the multiplicity M=2S+1, electrons with antiparallel spin occupy a singlet state (M=1) and electrons with parallel spin a triplet state (M=3). In a two particles system, the spin wave function of the particles with the spin can be written as follows [34, 42]:

Table 2.1 Possible spin states for two paired electrons

Exciton	Spin Wavefunctions	S	M_s
Singlet	$\|0,0\rangle=\frac{1}{\sqrt{2}}\{\uparrow\alpha\downarrow\beta-\downarrow\alpha\uparrow\beta\}$	0	1
Triplet	$\|1,1\rangle=\uparrow\alpha\uparrow\beta$	1	1
	$\|1,0\rangle=\frac{1}{\sqrt{2}}\{\uparrow\alpha\downarrow\beta+\downarrow\alpha\uparrow\beta\}$	1	0
	$\|1,-1\rangle=\downarrow\alpha\downarrow\beta$	1	-1

Here, electrons are represented by α and β, $\downarrow$ and $\uparrow$ symbols are the possible spin states of each electron, and S and M_s are the total and magnetic spin quantum numbers, respectively. There is one realization possible for S=0 and there are three realizations possible for S=1.

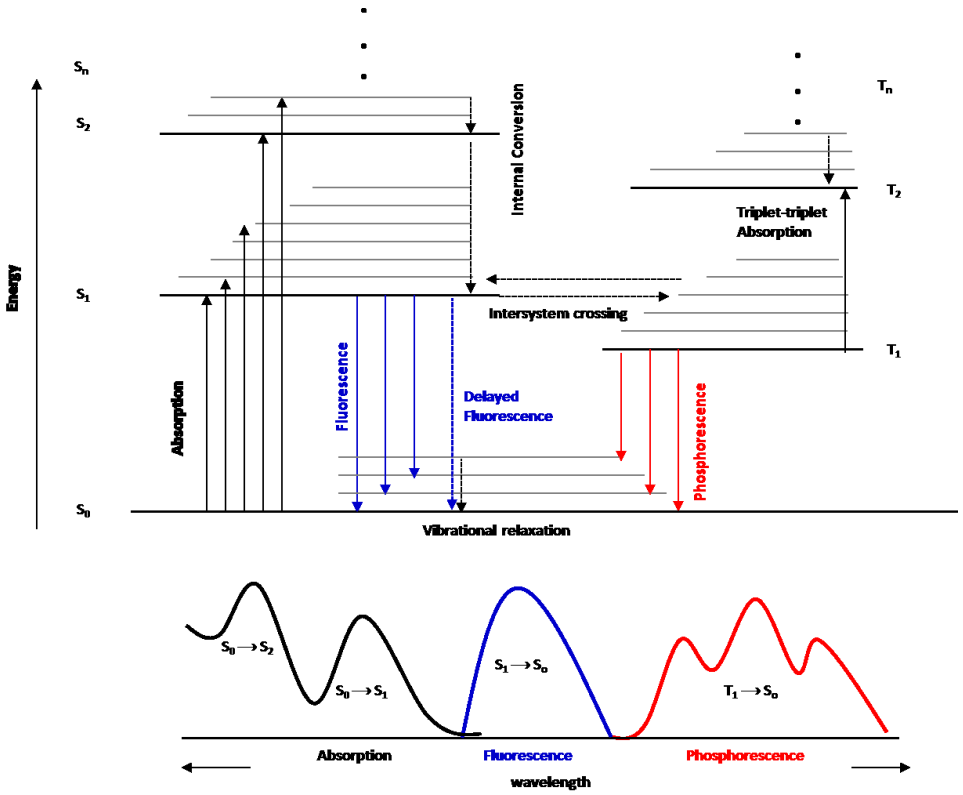

Figure 2.2: Optical transitions of a single molecule depicted in a Jablonski diagram. Non-radiative processes (internal conversion and intersystem crossing) are marked by dashed lines.

A useful approach to understanding the excitation and emission process in molecules was first established by Alexander Jablonski in the 1930s, as depicted in Figure 2.2 [43-46]. The diagram schematically displays the singlet ground state S_0, the first two excited singlet states S_1 and S_2, the first two excited triplet states T_1 and T_2, and the corresponding vibrational modes. This diagram represents the possible processes within an organic molecule: photon absorption, internal conversion, fluorescence, intersystem crossing, delayed fluorescence, and phosphorescence.

Absorption

The ground state (S_0) of an organic molecule is a singlet state, because all electrons are paired and have opposite spin orientations (a total spin quantum number S=0) according to Pauli's exclusion principles [39]. When talking about the ground state, a molecule may still have sub-level of S_0 with excess vibrational and rotational energy. By absorption of a photon with an energy larger than the HOMO-LUMO energy difference, an electron which is originally placed on the S_0 is excited to a higher singlet state S_1, S_2 …S_n according to the Frank-Condon principle [34]. This absorption process occurs very rapidly (~10^{-15}s) compared to other

processes [44]. The molecule is then said to be in an excited state. All absorbed energy is eventually relaxed, and vibrational relaxation and radiative decay are the chief ways that the molecule returns to the low-energy ground state.

Internal conversion

Internal conversion is a non-radiative transition between two electronic states of the same spin multiplicity. When an organic molecule is excited to an energy level higher than the lowest vibrational level of the first electronic state, the higher vibrionic state within S_1 relaxes to the lowest vibrational level of S_1 state through vibrionic relaxation, while higher energy singlet states such as $S_2 \ldots S_n$ relax to the lowest vibrational level of the S_1 state via non-radiative internal conversion processes under Kasha's rule [47]. From S_1, internal conversion to S_0 is possible but is less efficient than conversion from S_2 to S_1 due to the much larger energy gap between S_1 and S_0.

Fluorescence

On the left side of the diagram (Figure 2.2) are the singlet states, denoted as S_0, S_1, $S_2 \ldots S_n$. These states maintain the paired $+^1/_2$ and $-^1/_2$ spin states of the electrons, with each electron in a pair having opposite spins. S_1, S_2, and S_n are excited singlet states in which an outer electron of the molecule is boosted into a different orbital. S_2 contains more energy than S_1 and S_1 contains more energy than the ground state. The S_1 state can be generated by direct $S_0 \rightarrow S_1$ excitation or by intersystem crossing $S_2 \rightarrow S_1$. The relaxation from S_1 to S_0 (spin-allowed transition) with radiative emission is called fluorescence. These emitters, which emit solely from the singlet state, are called fluorescent emitters.

The transitions from S_1 to ground state are not necessarily radiative; they can also occur non-radiatively via internal conversion. The total quantum yield Φ_q is:

$$\Phi_q = \frac{k_r}{k_r + k_{nr}} \tag{2.2}$$

where k_r and k_{nr} are the radiative and non-radiative transition rates, respectively.

Due to vibrational relaxation in the excited state (energy loss), the fluorescence spectrum is located at higher wavelength (lower energy) than that of absorption spectrum, as shown in the Franck-Condon diagram (Figure 2.3) [48]. The gap (expressed in wavelength) between the first absorption band and first fluorescence peak is called Stokes shift. In room temperature, the

absorption spectrum partly overlaps the fluorescence spectrum; because a small fraction of molecules is in a vibrational level higher than level 0 in the ground state as well as in the excited state.

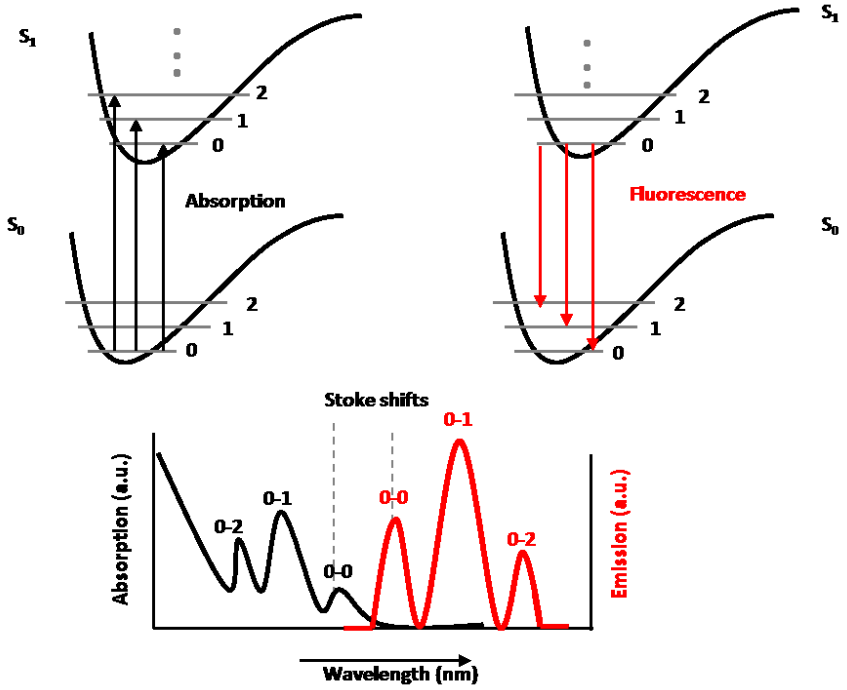

Figure 2.3: Schematic Franck-Condon diagram, adopted from the literature [48].

Intersystem crossing

Intersystem crossing is a non-radiative transition between two electronic states with different spin multiplicities. Fluorescence emission is not the only way for singlet excited states to relax their energy. In many organic molecules, the triplet state's vibrational energy levels overlap with the energy level of S_n. An excited molecule in the S_n state can move to the vibrational level of excited triplet states (T_n), or conversely, T_n can move to S_n [43].

Phosphorescence

On the right side of the diagram (Figure 2.2) are the triplet states, denoted as T_1, T_2...T_n. Because the transition probability of direct excitation from $S_0 \rightarrow T_1$ is quite small, the lowest triplet states are produced through intersystem crossing from $S_1 \rightarrow T_1$ transitions. The higher energy triplet states such as $T_2 \ldots T_n$ can also relax to the T_1 state via non-radiative internal conversion. From quantum theory, transitions between triplet states and ground state (which is singlet state) are, in principle, forbidden; therefore, the triplet state is mainly deactivated by internal non-radiative relaxation. However, by utilizing heavy metal atoms (e.g. platinum,

osmium, or iridium), it is possible to induce spin-orbit coupling and increase intersystem crossing rate between the singlet and triplet states. The relaxation from T_1 to S_0 with radiative emission is called phosphorescence ($T_1 \rightarrow S_0 + h\nu$), and the emitters are called phosphors [11]. The phosphorescence spectrum is located at a higher wavelength than that of fluorescence, because the energy of the lowest excited triplet state is lower than that of the lowest excited singlet state.

Under high concentration conditions, a collision between two molecules in the T_1 can provide enough energy to promote one of them into the excited singlet state (S_n), which can ultimately undergo radiative decay. This up-conversion process, called triplet-triplet annihilation (TTA), can lead to a delayed fluorescence emission [49]. In a fluorescent system, the TTA process may enhance the device performance [50, 51]. In a phosphorescent system, any singlet exciton formed during the TTA process can quickly transfer back into a radiative triplet state via intersystem crossing, however, at least one triplet exciton will be lost in the process, thus significantly degrading the device performance. A molecule in T_1 can absorb another photon at a different energy because triplet-triplet transitions are spin allowed. These transitions can be observed when the population of molecules in the triplet state is sufficiently large.

Thermally activated delayed fluorescence

Reverse intersystem crossing T_n to S_n can occur when the energy difference between T_1 and S_1 (ΔE_{st}) is small and when the lifetime of T_1 is sufficiently lengthy. This results in an emission with the same spectrum as normal fluorescence but with a much longer lifetime, because the molecules remain in the triplet state before emitting from S_1 [52]. Because this fluorescence emission is thermally activated, the efficiency generally increases as temperature increases.

2.1.2 Intermolecular energy transfer

When a molecule is in an excited state, monomolecular deactivation is not the only way to relaxes to the ground state; it can also transfer the energy to neighboring molecules. This process is referred as

$$D^* + A \rightarrow D + A^* \tag{2.3}$$

where D is the donor molecule providing energy; and A is the acceptor molecule harvesting energy. Energy transfer between organic molecules can be classified into radiative and non-radiative energy transfer. Non-radiative energy transfer can take place via dipole-dipole

interactions (Förster transfer) and electron exchange (Dexter transfer), as discussed below.

Reabsorption

Radiative energy transfer is a two-step process: radiative relaxation of the donor and followed by re-absorption of this photon by acceptor. This is expressed as follows:

$$D^* \longrightarrow D + h\upsilon$$
$$A + h\upsilon \longrightarrow A^* \tag{2.4}$$

where $h\upsilon$ is the photon energy. The interaction radius of the reabsorption process is in the range of more than 10 nm. For the realization of efficient OLEDs, it is necessary to prevent the re-absorption of emitted light. Fortunately, due to the strong Stokes shift in organic semiconductors, this process is mostly negligible during the use of organic emitters in OLEDs [39].

Förster transfer

The energy released from an excited donor can simultaneously excite the ground-state acceptor based on the Coulomb interaction between these two molecules (Figure 2.4). This direct energy transfer process is called as Förster transfer [53], and it is based on a dipole-dipole electromagnetic interaction which consequently depends on the overlap between acceptor's absorption spectrum and the donor's emission spectrum. The energy transfer efficiency is proportional to r^{-6} and expressed as follows [53]:

$$E = \left(1 + (\frac{r}{r_0})^6\right)^{-1} \tag{2.5}$$

where E is energy transfer efficiency, r is donor-acceptor distance, and r_0 is the Förster distance of donor and acceptor pair at which E=0.5. This process occurs in several nanometers (up to ~ 10 nm). The spin conservations of both donor and acceptor must be obeyed in this process. And only the singlet-singlet interaction is very efficient in Förster transfer:

$$D_S^* + A_S \rightarrow D_S + A_S^* \tag{2.6}$$

where the "S" marks the spin of the excited state.

Dexter transfer

The process based on electron exchange between two neighboring molecules is called Dexter

transfer [54]. In this energy transfer process, electron exchange is dependent on the orbital overlapping of donor and acceptor (Figure 2.4), so the transfer rate decays exponentially as the distance of donor-acceptor increases. Thus, this energy transfer is a short-range process (typically ~1 to 3 nm). Furthermore, only the total spin of donor and acceptor must be conserved, so both singlet and triplet transfer can be realized in this process, as shown in the following expressions:

$$D_S^* + A_s \rightarrow D_S + A_S^*$$
$$D_T^* + A_T \rightarrow D_T + A_T^*$$

(2.7)

where the "S" and "T" mark the spin of the excited state.

Exciton Diffusion

Excitons in an amorphous organic layer are strongly localized on individual molecules. Although they cannot move freely, they can still move in a series of uncorrelated hopping steps by means of Förster or Dexter transfer from molecule to molecule [55]. In most OLEDs, the exciton generation zone is at an interface between two layers and can be assumed to be very thin. The excitons have limited diffusion length

$$L_D = \sqrt{D\tau} \tag{2.8}$$

where L_D is the diffusion length; D is the diffusion coefficient; and τ is exciton lifetime. Triplet excitons can have a much larger diffusion length (tens of nm) than singlet excitons (<10 nm) due to their longer lifetime [56]. When triplet concentration is high, the exciton diffusion length is significantly reduced by the TTA process. Specific organic compounds have different diffusion lengths of singlet and triplet excitons, so they can be utilized for emission layer design in OLEDs.

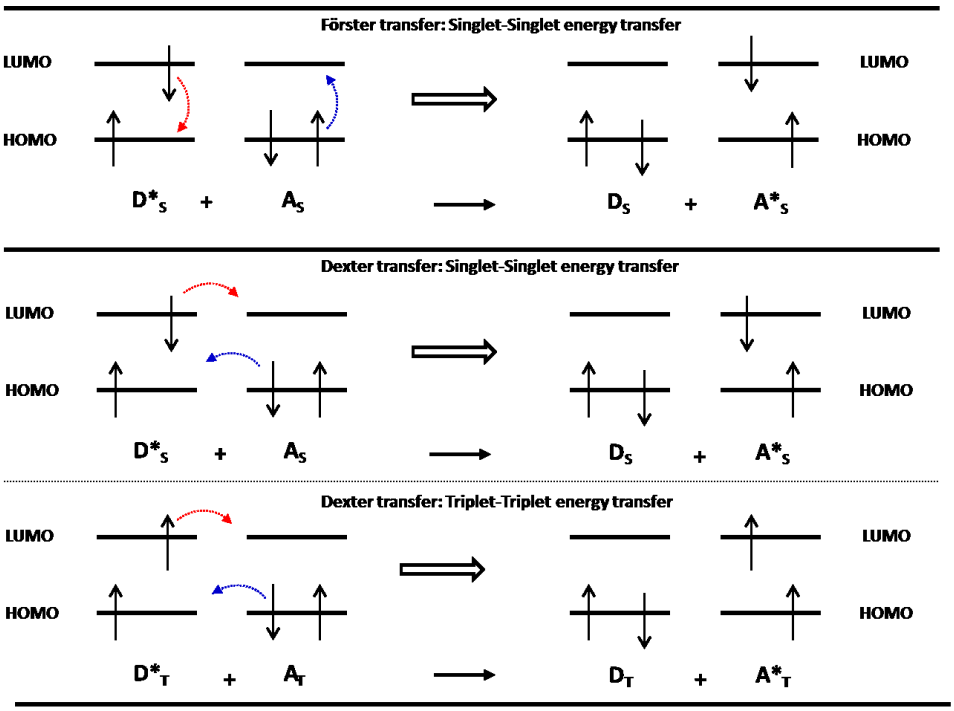

Figure 2.4: Schematic diagram of Förster transfer in singlet-singlet and Dexter transfer in singlet-singlet and triplet-triplet energy transfer. Notes: The electrons remain at the same molecule in Förster transfer while the electrons of two molecules are exchanged in Dexter transfer; electron transition is indicated by dotted arrows; and the "S" and "T" mark the spin of the excited state.

2.2 Organic light-emitting diodes

2.2.1 OLEDs evolution

Electroluminescence is a phenomenon where light emission is generated by electrical excitation. Electroluminescence from organic materials was first discovered in 1953 using a cellulose film doped with acridine orange [1], and was developed using an anthracene single crystal sandwiched between two electrodes in 1963 [2]. This investigation involved the basic process of organic electroluminescence: charge carrier injection from two electrodes, charge carrier transport, exciton formation in the recombination zone, and radiative decay of exciton. The operate voltage was as high as 400 V and the thickness of crystals was about 10-20 μm. In an attempt to reduce the drive voltage, Vincett et al. used thin organic films (about 0.6 μm) prepared by vacuum vapor deposition, and the visible electroluminescence in a normal room lighting was obtained at applied voltage as low as 30 V [57]. Several drawbacks (e.g., low light output efficiency, poor stability) make these early devices rather impractical.

In 1987, a thin film organic device with sandwiched structure was constructed by Tang and

VanSlyke from Kodak Inc. It comprised tris(8-hydroxyquinoline)aluminum (Alq_3) as an electron transporting and emissive layer and diamine as a hole transporting layer [58]. The novel design achieved a good balance of the charge carriers in the emitting layer and high brightness (> 1000 cd/m^2, suitable for commercial display) at a driving voltage below 10 V. Electroluminescence from conjugated polymer was first reported by the Cambridge group in 1990 [59], using poly(p-phenylene vinylene) (PPV) as the active layer between metallic electrodes. The reasonably high efficiency, low driving voltage (below 14 V) and simple fabrication process suggested that these polymers would also be readily commercialized for display and lighting applications. Indeed, since then, they have received increasing research attention due to their potential use in flat-panel displays and illumination sources. In 1993, Kido and co-workers developed the first white OLEDs with three emitting layers. White light, over 2000 cd/m^2, nearly as bright as a fluorescent lamp was achieved at a drive voltage of 15-16 V [60]. In 1998, Forrest and Baldo reported the discovery of phosphorescent emitters 2,3,7,8,12,13,17,18-octaethyl-21H,23H-porphine platinum(II) (PtOEP) in OLEDs which provided a significant boost in device efficiency [11]. By the end of the 1990s, OLEDs had entered the commercialization stage and were generally considered to be promising candidates for the next generation of flat-panel displays and illumination sources [61, 62]. Very recently, in 2012, Adachi's group developed a series of innovative TADF emitters based on carbazolyl dicyanobenzene (CDCB) to harvest triplet excitons for fluorescence through facilitated reverse intersystem crossing ($T_1 \rightarrow S_1$ transition), thus leading to an internal quantum efficiency in excess of 90%, which was comparable to that achieved from high-efficiency PhOLEDs [12].

OLEDs already meet the requirements for commercial flat panel display application, they merit further research to eliminate certain persistent drawbacks in their design, engineering, and fabrication [63-66]. In particular, a fundamental and universal understanding of the working principle of OLEDs is the crucial prerequisite for the success of OLEDs technology in the future.

2.2.2 Operation mechanism

The general structure of OLEDs consists of a sequence of organic layers between two electrodes. Figure 2.5 illustrates the architecture of a typical bottom-emitting OLEDs, which consists of a transparent metal oxide anode, hole injection layer (HIL), hole transport layer (HTL), emission layer (EML), electron transport layer (ETL), electron injection layer (EIL), and cathode.

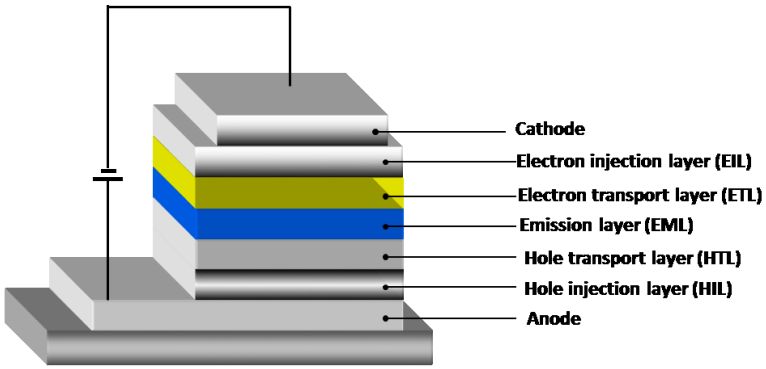

Figure 2.5: Layer sequence of OLEDs with separate hole, electron injection, and transport layers.

The basic physical processes in typical OLEDs can be roughly divided into four steps, as depicted schematically in Figure 2.6. For simplicity, the spatial variation of the molecular energy levels is drawn in a band-like fashion, however, we have to bared in mind that the organic molecules are in actuality disordered materials without a well-defined band structure. The four steps are as follows:

1) Charge carrier injection from the electrode;

2) charge carrier transport towards the opposite electrode;

3) exciton formation due to the coulomb interaction;

4) radiative decay of excitons.

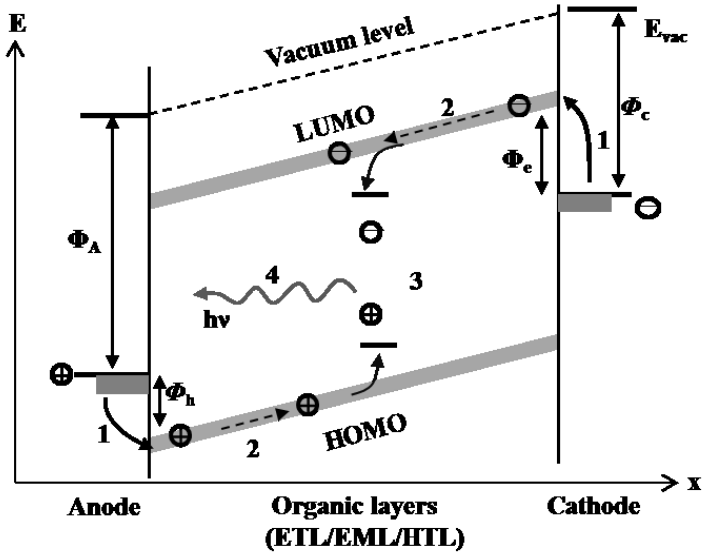

Figure 2.6: Schematic energy level diagrams of OLEDs and basic steps of EL. 1) charge carrier injection; 2) charge carrier transport; 3) exciton formation; and 4) radiative exciton decay.

Energy level alignment

Metal-organic and organic-organic interfaces play an important role in charge carrier injection and transport through OLEDs. Before discussing these interfaces, several additional parameters should be defined [67-69]. The vacuum level (E_{vac}) is the minimum potential energy of a free electron which is not in a bound state of the molecule or solid material. The Fermi level (E_F) is the energy up to which all states of a metal are occupied by electrons at absolute zero. The work function (WF) is the difference between E_F and the vacuum level. The electron affinity (EA) is the amount of energy released when an electron is added to a neutral atom or molecule in the gaseous state to form a negative ion, and in the solid state material, this refers to the energy difference between LUMO and E_{vac}. The minimum energy required to eject an electron from the HOMO level into vacuum is called ionization energy (IE).

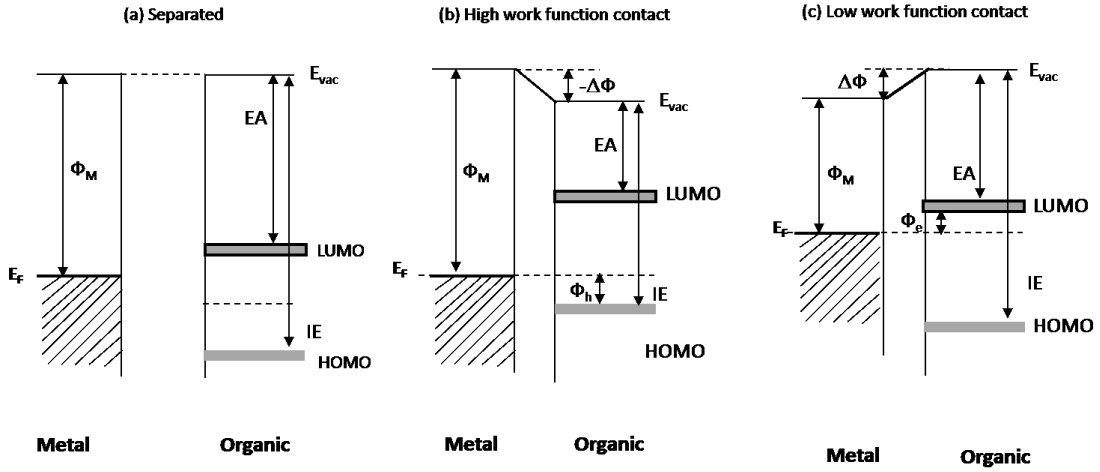

Figure 2.7: Schematic energy level diagrams for interface between electrodes and organic materials. (a) Separated; (b) low work function contact; and (c) high work function contact.

When the electronic property of MO interface was first explored, it was generally assumed that they follow the rules of commonly known inorganic MO interfaces: namely the Schottky-Mott limit. According to this rule, the hole injection barrier (Φ_h) and electron injection barrier (Φ_e) can be pre-calculated once the properties of the separated constituents are known. Subsequent work on a wide variety of MO interfaces proved that the situation is more complex. Usually, an interface dipole is formed leading to a shift of the vacuum level compared to the separated constituents [68]. This interface dipole is caused by rearrangement of the electron density distribution at the metal/molecule surface. A qualitative image of the interface energetics in the case of weak organic-

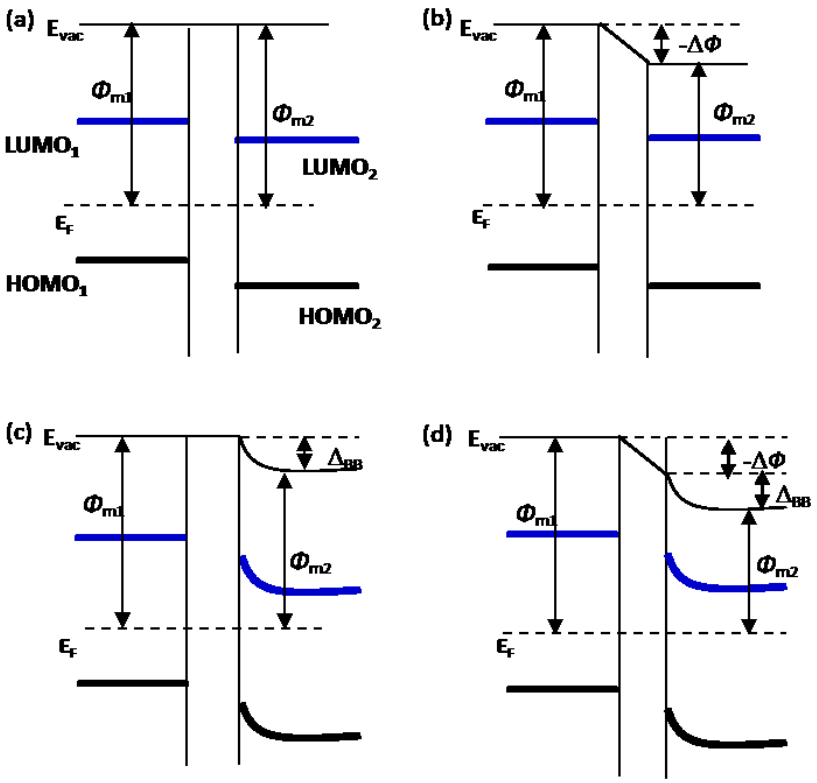

Figure 2.8. Schematic energy level diagrams of organic/organic interfaces: (a) with flat energy levels in both organics; (b) with an interfacial dipole and no energy level bending; (c) with energy level bending but no interfacial dipole; and (d) with an interfacial dipole and energy level bending.

metal interactions are shown in Figure 2.7. Φ_h and Φ_e can be changed by the vacuum energy shift $\Delta\Phi$, thus the high work function metal electrode is used for hole injection and the low work function metal electrode is used for electron injection.

The charge carrier injection process at the organic/organic interface is well known to have great influences on the performance of organic optoelectronic devices. As shown in Figure 2.8, it is generally believed that the organic/organic heterointerfaces commonly forms vacuum level alignments, this energy level alignment is attributed to the weak intermolecular and intramolecular Van der Waals interactions between organic materials. Therefore, the charge carrier injection barriers can be calculated by using the following equations:

$$\phi_h = |IE_{m1} - IE_{m2}|$$
$$\phi_e = |EA_{m1} - EA_{m2}| \quad (2.9)$$

where Φ_h and Φ_e are hole and electrons injection barriers, respectively; IE and EA are the ionization energy and electron affinity, respectively; and the subscript "$_{m1}$" and "$_{m2}$" mean the organic material 1 and organic material 2, respectively. However, in the most of cases, the

presence of interfacial dipoles and energy level bending tends to result in a discontinuity of the vacuum level at the O/O interface (as shown in Figure 2.8 b-d) [68-70]. As a result, the interfacial energy barriers have to be modified as

$$\phi_h = |IE_{m1} - IE_{m2} - \Delta\Phi - \Delta_{BB}|$$
$$\phi_e = |EA_{m1} - EA_{m2} - \Delta\Phi - \Delta_{BB}| \quad (2.10)$$

where IE and EA are the ionization energy and electron affinity, respectively; $\Delta\Phi$ is the interfacial dipole; and Δ_{BB} is the energy level bending at the interface, the subscript "$_{m1}$" and "$_{m2}$" mean the organic material 1 and organic material 2, respectively. Note that the energy barrier would be underestimated if the $\Delta\Phi$ and Δ_{BB} are not taken into consideration. However, in an experimental measurement, usually it is difficult to quantitatively predict the magnitude of dipoles and energy level bending, due to manifold factors that contribute to the formation of O/O interfacial energy level alignments, including the molecular orientations, density of gap states, substrate effects, et all.

Charge carrier injection from electrode

The active organic layers are sandwiched between a high work function anode and a low work function cathode. At least one of the electrodes must be transparent to allow light to be emitted from the device. If an external voltage is applied between the two electrodes, electrons are injected from the cathode into the ETL LUMO beyond a threshold Φ_e and holes are injected into the HTL HOMO from the anode beyond a threshold voltage Φ_h. The charge carrier injection into the organic layers is determined by the interface formed between the electrode and the organic layer. Early models were adapted from inorganic semiconductor injection theory such as Schottkey injection and Fowler-Nordheim field emission, while more recent theories generally assert that the injection current from a metal electrode into an organic semiconductor can be adapted from equations for Schottky contacts for inorganic semiconductors [71]. To get injected, charge carriers have to get across the energy barrier between the work function of the electrode and the HOMO or LUMO levels of the organic semiconductor (depending on hole or electron injection). The current density J across this energy level is given by:

$$J = J_0 \left[exp\left(\frac{qV}{nkT}\right) - 1 \right] \quad (2.11)$$

where J_0 is the saturation current density, q is the elementary charge, V is the applied voltage, n is the ideality factor, and T is the temperature. For the saturation current density, it is assumed that the charge carriers from the electrode can be injected once acquiring sufficient

thermal energy to pass the injection barrier. Many studies have found close agreement between experimental data and the thermionic emission mode [72-74], where the saturation current density J_0 is given by the following equation:

$$J_0 = A^* T^2 exp\left(-\frac{q\Phi_B}{kT}\right) \quad (2.12)$$

where A^* is the effective Richardson constant, given by $A^* = 4\pi q m^* k^2/h^3$ (m^* is the effective charge carrier mass, k is the Boltzmann constant, and h is Planck constant), T is the temperature, k is the Boltzmann constant, and Φ_B is the injection barrier for charges (Φ_e *or* Φ_h, as shown in Figure 2.6).

In OLEDs, large barriers of Φ_h or Φ_e lead to poor performance. For the commonly used anode indium tin oxide (ITO, WF=4.3-5 eV) and air-stable cathode aluminum (Al, *WF*=4.1 eV) [75, 76], most organic materials have a charge injection barrier. In order to realize the most efficient charge carrier injection into organic layers, thin charge injection layer between electrode and charge transport layer is needed. For hole injection, molybdenum oxide (MoO_3) and 1, 4, 5, 8, 9, 11-hexaazatriphenylene hexacarbonitrile (HAT-CN) have attracted a great deal of research attention due to their remarkable hole injection barrier lowering properties [77-79]. In the case of MoO_3, the Fermi level is located close to the conduction band. In the HTL/MoO_3 heterojunction, an interface dipole is formed as the organic material transfers electrons to the injection layer. The resulting shift in Fermi level of the HTL layer enables the injection of holes by efficient electron extraction via the MoO_3 conduction band. Moreover, a gap state in the HTL assists Ohmic hole injection at the interface [79]. In the case of HAT-CN, it's a good conducting molecular with the LUMO level is very close to the Fermi level. This enables an easy excitation of electrons from HTL HOMO to HAT-CN LUMO, which forms a charge carrier generation interface [80]. As an alternative strategy, the use of appropriate surface treatments (e.g., UV-Ozone treatment, plasma treatment) for anode to minimize the injection barrier are also quite useful [81, 82]. A typical example of electron injection is the use of an ultra-thin mono (8-quinolinolato) lithium (Liq) layer as cathode interface layer in combination with Al. In the case of Liq, the alkaline metal ions in the complexes are reduced to free metal by the reaction between the complexes and thermally activated Al in vacuum. The free alkaline metal then reacts with the electron transporting material, forming radical anions which facilitate electron injection from the Al cathode [83].

Charge carrier transport in organic layers

In the presence of an electric field, the injected charge carriers travel through the active organic layers and move towards the opposite electrode. The charge transport layers in OLEDs

generally play the role of accepting charge carrier injection from the electrodes and transporting the injected charge carrier to the active emitting layer.

The difficulty in extending the charge carrier transport theory from inorganic semiconductors to organic semiconductors arises because of the absence of extended delocalized states in organic materials. Charge carrier transport is typically not a coherent motion in well-defined bands but rather a stochastic process of hopping between localized states [84]. The strong current injection into low-mobility organic materials inevitably leads to charge accumulation in the organic layers. Hence, the charge carrier transport exhibits Ohmic and injection-limited behavior in the low voltage range and space-charge limited current (SCLC) behavior in the high voltage range [85]. In the case of a steady current with a linear response to an applied voltage, Ohmic charge carrier transport obeys Ohm's law [86]

$$j_{Ohmic} = en_0\mu\frac{V}{d} \tag{2.13}$$

where e is the elemental charge, n_0 is the electron density, μ is the charge carrier mobility, V is the applied voltage, and d is the thickness of the organic layer. The occurrence of SCLC requires that at least one contact has good injection properties to provide an inexhaustible carrier reservoir. For a perfect insulator without intrinsic carriers or traps, and in case of charge carrier mobility is independent of the electric field, the SCLC obeys the Mott-Gurney equation [87, 88]

$$j_{SCLC} = \frac{9}{8}\varepsilon\varepsilon_0\mu\frac{V^2}{d^3} \tag{2.14}$$

where ε is the relative dielectric constant; ε_0 is the vacuum permittivity; μ is the charge carrier mobility; V is the applied voltage; and d is the thickness of the organic layer. The threshold voltage V_0 at which current transforms from Ohmic to SCLC mode can be found by equating the two currents as follows [88]:

$$V_0 = \frac{8}{9}en_0\frac{d^3}{\varepsilon\varepsilon_0} \tag{2.15}$$

where e is the elemental charge; n_0 is the electron density; d is the thickness of the organic layer; ε is the relative dielectric constant; and ε_0 is the vacuum permittivity.

Exciton formation

When an electron and a hole with a random spin state encounter each other while drifting through the organic layers, the attractive Coulomb force between them can lead to exciton formation. Exciton formation is governed by spin statistics, which create singlet excitons or

triplet excitons with a ratio of 1:3 according to the four spin-dependent states. The singlet and triplet excitons generated in amorphous organic materials are strongly localized on individual molecules (Frenkel excitons). In organic materials, exciton formation is a bimolecular process following Langevin theory with the generation rate K_{L} [89, 90]:

$$K_{\mathrm{L}} = \frac{q(\mu_e+\mu_h)}{\varepsilon\varepsilon_0} \tag{2.16}$$

where q is the elementary charge, μ_e and μ_h are electron and hole motilities, respectively, ε is the relative dielectric constant, and ε_0 is the vacuum permittivity.

Radiative decay

Once excitons are formed, their corresponding energy can be transferred via several available channels. There are two possible relaxation paths involved in light emission: fluorescence from the $S_1 \rightarrow S_0$ transition and phosphorescence from the $T_1 \rightarrow S_0$ transition.

For fluorescent materials, according to the spin-forbidden transition, singlet excitons can relax into the ground state by relaxing energy in the form of light, while triplet excitons relax in a non-radiative thermal process. Therefore, 75% of the excitons are lost for emission and their energy is transferred into heat in fluorescent OLEDs.

For phosphors, central heavy metal ions induce significant spin-orbit coupling that is allowed under the radiative transition from $T_1 \rightarrow S_0$, which increases the intersystem cross rate from singlet and triplet states. Accordingly, almost 100% of the generated excitons can be harvested in PhOLEDs [11]. Among the known triplet harvesting concepts, an alternative approach is the up-conversion of triplet into singlet states. There are two possible pathways for this: TTA OLEDs and TADF OLEDs. In TTA OLEDs, two triplet excitons are converted into a singlet exciton when there is a large energy gap between S_1 and T_1 ($2T_1 > S_1$). Thus, the maximum internal quantum efficiency can be further improved to a maximum of 25%+0.5×75%=62.5% [50, 51]. In TADF OLEDs, all electrical generated triplet excitons can be up-converted to singlet states through reverse intersystem crossing because of the small energy gap between S_1 and T_1, then the light emission is extracted as a delayed fluorescence from S_1 to the ground state ($S_1 \rightarrow S_0$ transition). Therefore, the maximum internal quantum efficiency can be enhanced up to 100% [12, 91].

2.3 Highly efficient OLEDs

Electrons and holes are injected into the device from the electrodes by the driving voltage. The spins of the injected electrons and holes are stochastically distributed. If electrons and

holes recombine, according to known spin statistics, they will form 25% singlet excitons and 75% triplet excitons [92, 93]. For fluorescent emitters, only the radiative decay to the ground state from the singlet excited state (25% of formed excitons) is allowed; the radiative decay of triplet excitons (75% of formed excitons) to the ground state is forbidden under quantum theory. The EQE of OLEDs is expressed as follows:

$$\eta_{ext} = \eta_{\mathrm{C}} \times r_{\mathrm{st}} \times \Phi_{\mathrm{f}} \times \gamma \tag{2.17}$$

where η_{ext} is the external quantum efficiency, defined as the number of emitted photons from OLEDs divided by the number of injected charge carriers [5]; η_{C} is the fraction of photons that can escape from the device, which is typically 20-30% with flat glass substrates[6-8]; r_{st} is the probability that radiative decay will occur; and Φ_f is the fluorescent quantum efficiency or the fraction of excitons that can undergo radiative decay. In high performance organic emitter, Φ_f can approach 100%. γ is the probability that holes and electrons will recombine to form excitons; and to maximize γ, it is necessary to ensure a good balance between two types of charge in high efficiency devices. The equation can be further simplified as follows:

$$\eta_{ext} = \eta_{int} \eta_C \tag{2.18}$$

where η_{int} is the internal quantum efficiency, which is defined as the ratio of the number of photons that can be extracted to the number of injected charge carriers. Simple statistics predict that η_{int} was only up to 25% in fluorescent OLEDs [92, 94]. Many previous researchers have attempted to utilize non-radiative triplet excitons to increase OLEDs efficiency.

2.3.1 Phosphorescent OLEDs

One successful way of utilizing triplet excitons is incorporating heavy metals into the organic aromatic framework to enhance spin-orbit coupling. Strong spin-orbit coupling effectively promotes intersystem crossing and enhances the subsequent radiative decay from the lowest triplet excited state to the ground state [11, 13]. By harvesting both triplet excitons and singlet excitons to photon emission, η_{int} of PhOLEDs of nearly 100% has been demonstrated (as shown in Figure 2.9) [13, 95-100].

In 1998, Baldo et al. improved luminescence quantum efficiency by doping phosphor into appropriate host materials in PhOLEDs [11]. The doped device generated saturated red emission with external and internal quantum efficiencies of 4% and 23%, respectively. Triplet excited states have long lifetime, typically in the microsecond to millisecond range, thus they

can be quenched by two bimolecular interactions (e.g., TTA and triplet-polaron quenching), especially at high current density [101, 102]. This effect can be reduced when suitable spacer groups are included on the organic materials [103].

Previous researchers have provided numerous innovative phosphors with suppressed quenching and have achieved impressive device efficiency. The triplet lifetime of phosphor can be changed by selecting different metal center. To date, a large number of phosphors have been successfully used in PhOLEDs with different metal complexes containing transition metals such as iridium, platinum, and osmium [9, 10, 104], etc. These devices exhibit a series of desirable properties such as emission wavelength covering the entire visible spectrum, long device lifetimes, and high quantum yields [105-107].

2.3.2 Thermally activated delayed fluorescence OLEDs

Triplet excitons can also potentially be exploited via reverse intersystem conversion, which involves transition from the lowest excited triplet state to the lowest excited singlet state. In this way, all excitons contribute to luminescence. Correspondingly, a molecule with efficient TADF requires a small energy gap between its lowest excited singlet and triplet states, which enhances the $T_1 \longrightarrow S_1$ intersystem crossing rate [108, 109]. It was previously assumed that the energy in S_1 is considerably higher (0.5-1.0 eV) than that in T_1, because of the electron exchange energy

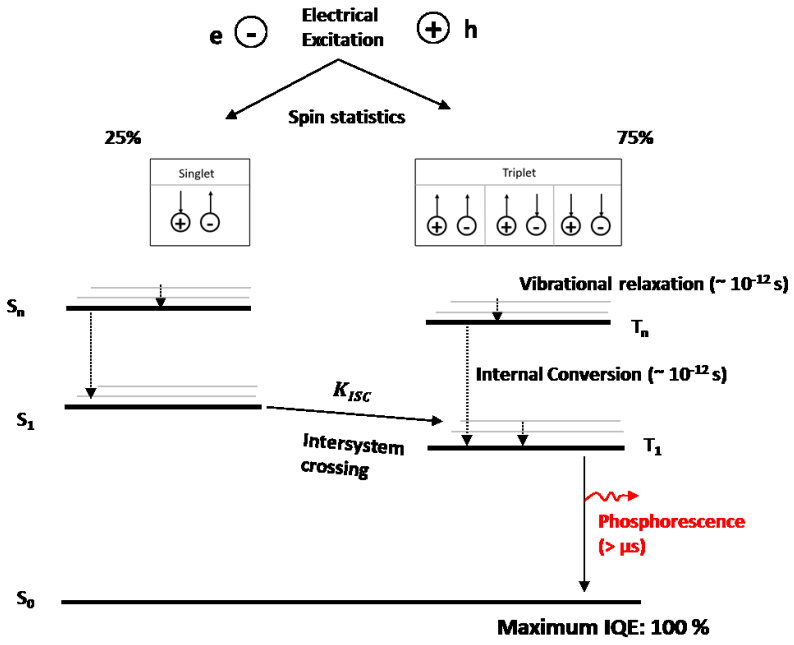

Figure 2.9: Schematic diagram of phosphorescence mechanism in PhOLEDs

between these levels [12]. Careful design of organic molecules can ensure a small energy gap between the lowest singlet and lowest triplet states. In 2012, Adachi et al. proposed a method of achieving internal quantum efficiency of OLEDs nearly 100% through the up-conversion of triplet excited states to singlet excited states using thermal energy [11]. The critical point of this molecular design is the combination of a ΔE_{ST} smaller than 100 meV, with a reasonable radiative decay rate (higher than 10^6/s) to overcome competitive non-radiative decay pathways leading to highly luminescent TADF materials.

The TADF emission occurs through four successive processes, as shown in Figure 2.10. First, singlet and triplet excitons with a ratio of 1:3 are formed via electron and hole recombination. Second, the high energy exciton states are transferred to the lowest excited states via vibrational relaxation and internal conversion; Third, the accumulated triplet excitons at T_1 are back transferred to S_1 via rapid and efficient reverse intersystem conversion; and finally, the singlet excitons at S_1 are formed by either direct electronic excitation or from T_1 by radiative decay to the ground state with prompt fluorescence and delayed fluorescence [44]. The cycle $S_1 \rightarrow T_1 \rightarrow S_1$ may repeat several times before delayed fluorescence take place.

During these processes, the efficient thermally activated reverse intersystem conversion from T_1 to S_1 is the key to harvesting triplet excitons. Theoretically, the triplet to singlet excited states conversion rate corresponds to an activated process [110-113]:

$$k_{RISC} = Aexp\left(-\frac{\Delta E_{ST}}{k_B T}\right) \tag{2.19}$$

where k_{RISC} is the reverse intersystem crossing rate, A is a constant, ΔE_{ST} is the energy gap, k_B is the Boltzmann constant, and T is the temperature.

The prompt fluorescence component has no temperature dependence, whereas the delayed fluorescence intensity increases proportionally with temperature. The results of evaluating ΔE_{ST} using Berberan-Santos equation are based on the following equation [114, 115]:

$$ln\left[\frac{\Phi_p}{\Phi_d} - \left(\frac{1}{\Phi_T} - 1\right)\right] = ln\left(\frac{K_r + k_{nr}^T}{K_{RISC}}\right) + \left(\frac{\Delta E_{ST}}{RT}\right) \tag{2.20}$$

where Φ_p is the prompt fluorescence efficiency, Φ_d is the delayed fluorescence efficiency, Φ_T is the triplet formation efficiency, k_r is the phosphorescence rate, k_{RISC} is the rate of reverse intersystem crossing, k_{nr}^T is the non-radiative decay rate of T_1 to ground state, R is the gas

constant, and T is the temperature. A kinetic scheme of TADF OLEDs is shown in Figure 2.10.

2.3.3 Host-guest system

For efficient electroluminescence by harvesting both singlet and triplet excitons, the exciton quenching associated with relatively lengthy excited state lifetime must be reduced [18, 116]. The emitting layer in high performance OLEDs normally formed with a host-guest system, which is employed by co-evaporating a small amount of guest emitter uniformly dispersed in the suitable matrix host material [117-120]. The host-guest system minimizes the aggregation of guest emitters to reduce the triplet exciton density thus reducing TTA and triplet-polaron quenching. The matrix host excitons formed in the host can simultaneously be transferred to the guest emitter, where the final emission take place, as shown in Figure 2.11 [11, 12]. The transfer of excitation energy to the guest is promoted by three processes, long range Förster transfer of singlet excitons generated on the host to the guest, short-range Dexter transfer of singlet and triplet excitons generated on the host to the guest, and direct generation of singlet and triplet excitons on the guest (where the host solely acts as a charge carrier transporting matrix) [121].

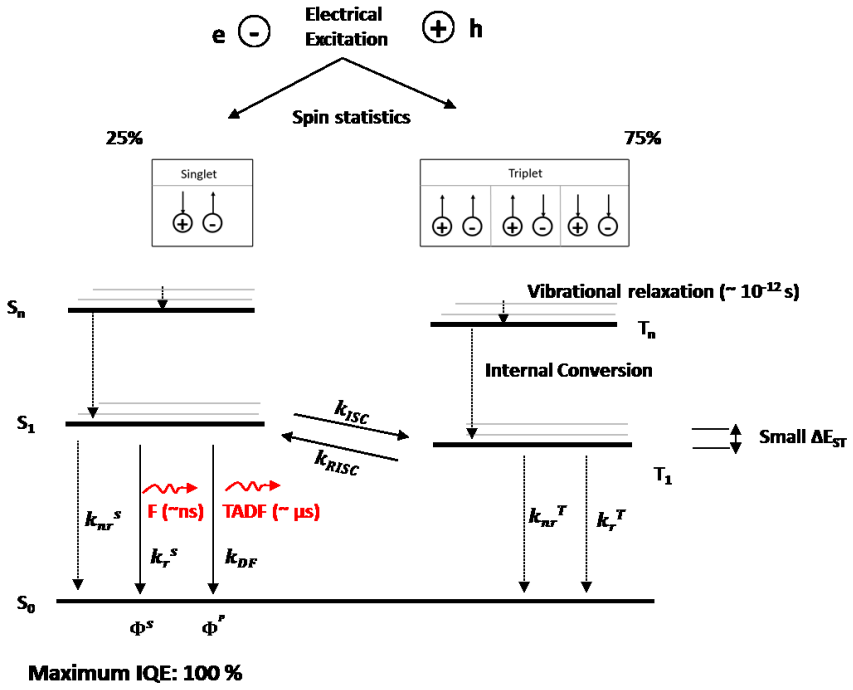

Figure 2.10: Kinetic scheme of TADF OLEDs. Note: k_{ISC} is the intersystem crossing rate; k_{RISC} is the reverse intersystem crossing rate; k_r^S is the prompt luminescence rate; k_{DF} is the delayed fluorescence rate; k_{nr}^S and k_r^S are the non-radiative decay rate and radiative rate of S_1 to the ground state, respectively; k_{nr}^T and k_r^T are the non-radiative decay rate and radiative decay rate

of T_1 to the ground state, respectively.

For Förster transfer, a significant overlap in the emission spectrum of the matrix host and the absorption spectrum of the guest is necessary. The efficiency of this energy transfer is expressed as follows [48, 122]:

$$\eta_{ET} = \frac{K_{ET}}{K_{ET}+K_R+K_{NR}} \tag{2.21}$$

where η_{ET} is the Förster transfer efficiency, K_{ET} is the Förster transfer rate from host to guest, and K_{R} and K_{NR} are radiative and non-radiative rates of the host and guest, respectively. Based on this equation, Förster transfer is efficient if $K_{ET} > K_R + K_{NR}$.

For Dexter transfer, the energies of the singlet and triplet excitons on the host should be higher than that of the guest to prevent reverse energy transfer from the guest back to the host and to confine the triplet excitons in the emitting layer. For a blue OLEDs, designing such materials has proven challenging because the triplet energy level (E_{T}) of the host materials must be larger than that of blue emitter [123]. A representative example using bis [(4,6-difluorophenyl)-pyridinato-N, $C^{2\prime}$] (picoinate) iridium (III) (FIrpic, E_{T}=2.64 eV) as blue emitter doped into two host molecules, 4-4′-N,N′-dicarbazole-biphenyl (CBP, E_{T}=2.55 eV) and 4,4′-bis(9-carbazole)-2,2′-dimethyl-biphenyl (CDBP, E_{T}=2.79 eV) was presented by Tokito [20, 124]. OLEDs which use CDBP:FIrpic exhibit a high EQE of 10.4%, much higher than that (5.1%) of devices using CBP:FIrpic. For FIrpic in a CBP host, the forward and backward energy transfers from the FIrpic triplet states to the CBP triplet states was found, which result in the low performance [124].

For a direct carrier trapping on the guest, significant offset of the HOMO and LUMO energies of the host and guest materials is necessary; thus, wide energy gaps (E_{g}) are needed for the host materials. The guest emitter molecules are believed to act as potential charge traps for electrons and holes in the emitting layer [117]. A high doping concentration minimizes the charge trapping but results in exciton quenching thereby reducing the device performance.

The relative competition among these three energy transfer processes require a reasonable balance between exciton quenching and charge trapping. For singlet-singlet exciton transfer, although all three mechanisms operate to some extent, Förster transfer generally dominates; for triplet-triplet exciton transfer, the Dexter transfer mechanism is the major mode.

Consequently, the selection of host materials is of great importance to ensure highly efficient OLEDs.

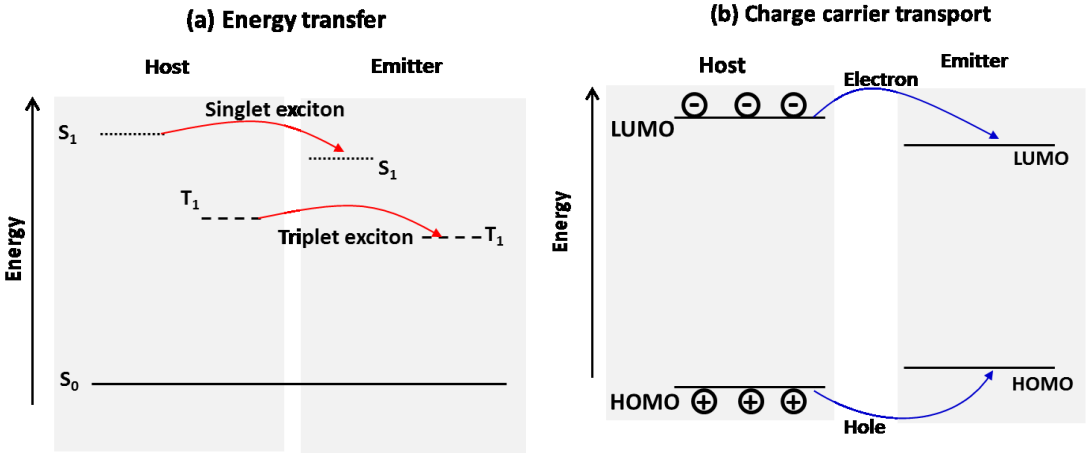

Figure 2.11: Simplified illustration of three transfer processes from host to guest: (a) energy transfer and (b) charge carrier transport.

Chapter 3

Methodology and materials

This chapter presents the techniques that can be used to prepare organic thin films and OLEDs, as well as the techniques used to characterize the host materials and OLEDs. The sample preparation details, sample characterization conditions, and processing of experimental data in the present study are also discussed below. The organic materials used in this work were also introduced here, including their molecular structures and relevant physical properties.

3.1 Experimental techniques and details

3.1.1 Sample fabrication

In terms of the growth methods, thin film preparation can typically be divided into two categories: vacuum deposition and solution processing.

Thermal vacuum deposition

Thermal vacuum deposition is a physical vapor deposition technique used to deposit thin films via the condensation of a vaporized form of the material. A schematic drawing of thermal vacuum deposition is shown in Figure 3.1. The material is placed with an evaporation source at the bottom of a vacuum chamber while the substrates are placed in a sample holder at the top of the vacuum chamber. The material is heated by passing a large current through the evaporation source. Above a certain temperature, the vapor is liberated from the solid source material, then leaves the crucible as a cone shaped flux of molecules or atoms, then travels atomistically (or molecularly for compounds) though the vacuum, finally condensing into a solid on the substrate or vacuum chamber walls [125]. The deposition rate and film thickness are monitored with a quartz crystal microbalance (QCM). The co-evaporation of materials was controlled according to the deposition rate used to prepare the doped organic layers. To measure the deposition rate of the host and dopant molecules independently, one QCM was placed near the substrate and another was placed short distance above the dopant source. During the co-evaporation in this work, the doping concentration is denoted in weight-percentage (wt%), which indicates the mass fraction of the dopant with respect to the dopant:host system

$$wt\% = \frac{m_{dopant}}{m_{doant}+m_{host}} * 100\% \quad (3.1)$$

In this work, all organic small molecule materials were deposited by thermal evaporation technique under high vacuum conditions between 4×10^{-6} and 1×10^{-6} mbar. The organic materials were placed in a quartz crucible on tantalum boat. The typical deposition rate for HTL, EML and ETL was 2 Å/s. For HIL and EIL, a low evaporation rate of 0.2-0.3 Å /s was used. For Al evaporation, a boron nitride crucible on a tantalum boat was used. The Al electrode was also prepared by thermal evaporation. During Al electrode deposition, a shadow mask was used to define the active area of the OLEDs (3 mm×3 mm= 0.09 cm^2) as well as the shape of the cathode. All the QCMs were calibrated by comparing the thickness of the film (deposited on silicon wafer) measured by QCM to that measured by spectroscopic ellipsometry (M-2000UI J. A. Woollam Co.). During the film deposition, shutter blades were used to prevent unwanted materials from being deposited on the substrate, and the substrate holders were rotated to compensate for the influence of the chamber's geometry. Two thermal evaporation tools were used in this work: PhOLEDs were fabricated in a single chamber deposition tool from FANGSHENG GmbH (FS-300), and the remaining samples were fabricated in a single chamber deposition tool from Trovato Inc. There are 12 evaporation sources in the FANGSHENG system and 16 in the Trovato system, which allowed us to fabricate samples without vacuum braking during the process. With the same sample layout system in these two deposition tools, 16 samples can be produced on a 4×4 wafer in one run and under identical conditions. To investigate the influence of changes in the OLEDs structure such as varied layer thickness or varied doping concentration, different samples were prepared using slit masks for every row and column of substrate. After the multilayer evaporation process, to protect the devices from mechanical damage, the OLEDs were encapsulated with a glass lid and sealed with glue in air.

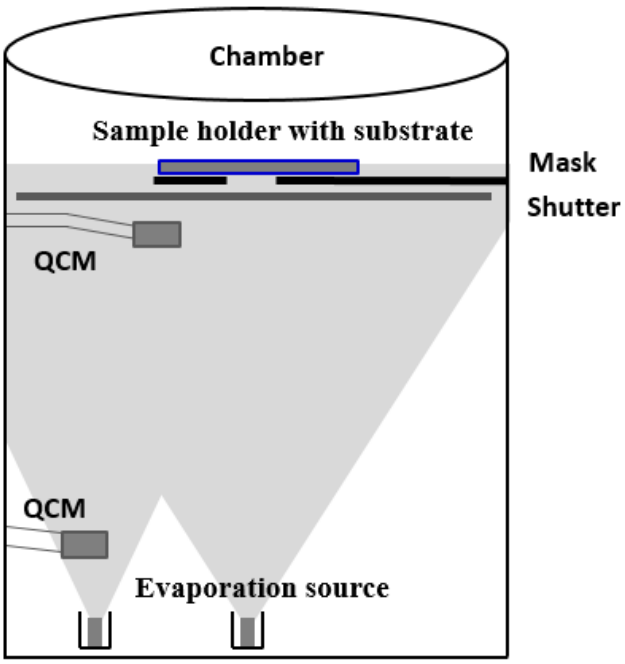

Figure 3.1: Schematic illustration of the thermal evaporation tool. Note: Materials in the crucible were thermally evaporated and deposited on the substrate. Deposition rate and thickness were monitored by QCM. Shutter blades were used to prevent unwanted material deposition and shadow masks were used to define the active area of the device.

Spin coating

Spin coating is a solution processing technique that can be used to prepare uniform thin films. During the spin coating process (Figure 3.2), a small amount of fluid material is deposited onto the center of a substrate which is either spinning at low speed or not spinning at all, the substrate is then rapidly accelerated to the desired rotation speed with the spin coater. Owing to the action of centrifugal force, the excess solution is ejected from the substrate, resulting in the formation of a homogeneous thin film [126, 127]. Once the spin coating process is complete, the substrate is typically placed onto a hotplate at a high temperature to remove the residual solvents.

In this work, thin polyethylenimine ethoxylated (PEIE) film was prepared on ITO glass with a spin coater from Laurell Inc. PEIE (MW=70000 g/mol) was dissolved in H_2O with a concentration of 35-40% when received from Sigma-Aldrich, then it was further diluted with 2-methoxyethanol to a weight concentration of 0.4%. The spin coating speed was ramped up to 5000 rpm in increments of 1000 rpm/s over 5 s. After this, the ITO/PEIE substrates were annealed at 100˚C on a hot plate for 10 min in ambient air. The thickness of the PEIE film was estimated to be around 10 nm [128].

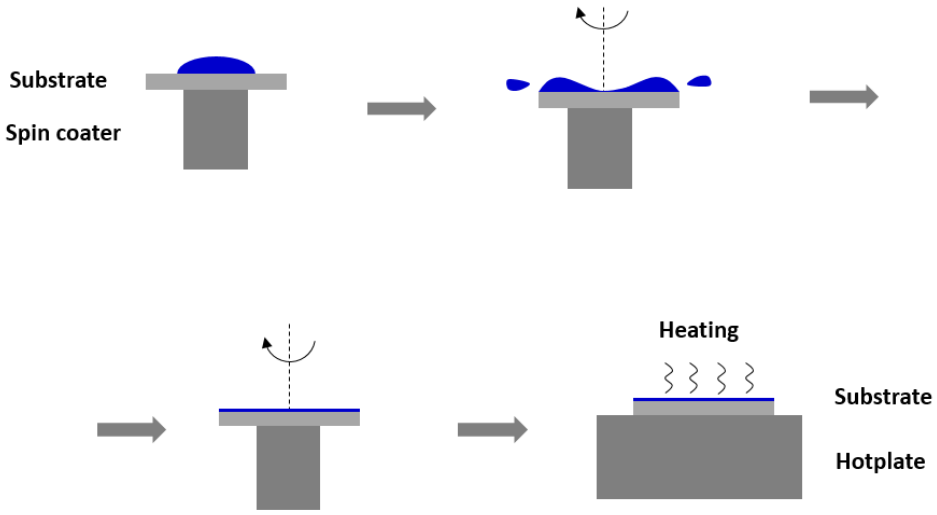

Figure 3.2: Schematic drawing of deposition and heating steps of the spin coating process. (Top left) deposition of coating fluid on the substrate; (top right) the substrate is accelerated to a high speed to distribute the solution; (bottom left) the rotation of the substrate is kept while the solvents evaporate; and (bottom right) the substrate is heated to remove the residual solvents.

3.1.2 Characterization of host materials

Various techniques were utilized to characterization the host materials, including differential scanning calorimetry (DSC), thermogravimetric analysis (TGA), photoluminescence (PL) spectroscopy, phosphorescence spectroscopy, ultraviolet and visible (UV-Vis) absorption spectroscopy, photoelectron spectroscopy (PES), and transit photoluminescence (PL) decay.

Differential scanning calorimetry

Differential scanning calorimetry is a thermal analysis technique that used to look how a material's heat capacity changes with temperature. The DSC process is illustrated in Figure 3.3a. A sample of known mass is heated or cooled and the changes in its heat capacity are tracked as changes in the heat flow. During the experiment, both the sample and reference are maintained at the same temperature (which varies linearly as a function of time). When the sample undergoes a physical transformation such as glass transition, more or less heat is needed to flow it compared to the reference at same temperature. Whether less or more heat is needed depends on whether the process is exothermic or endothermic. For example, as a solid sample melts to a liquid, it requires more heat flowing to the sample to increase its temperature than the reference, due to the absorption of heat by the sample as it undergoes exothermic phase transition from solid to liquid [129, 130].

In this work, DSC was performed on a TA DSC 2010 unit at a heating rate of 10°C/min under a nitrogen atmosphere. After the experiment, spectra were first converted to ASCII-

format and then imported into Origin 8 (OriginLab Corporation) for further processing. The temperature at the lowest point of the curve was considered the DSC temperature, or as T_g, as shown in Figure 3.3b.

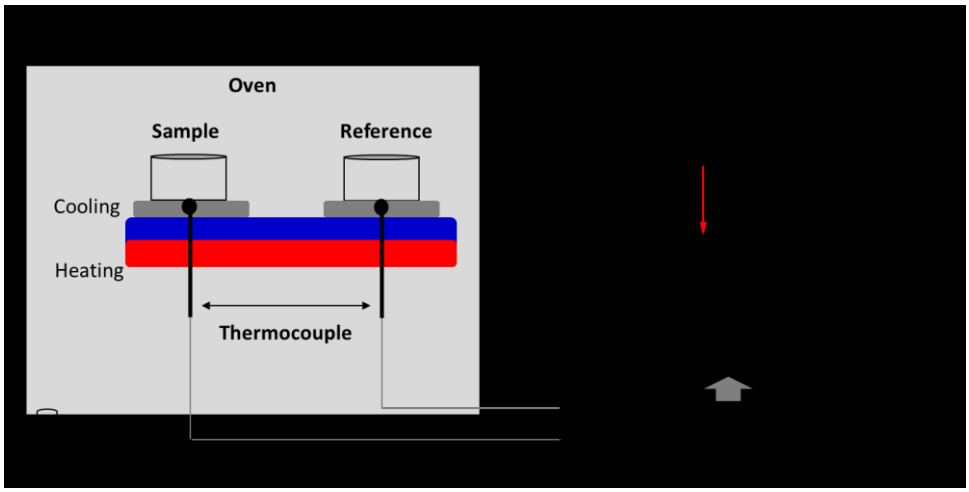

Figure 3.3: (a) Schematic setup for DSC and (b) schematic drawing of the procedure to derive T_g.

Thermogravimetric analysis

Thermogravimetric analysis is a thermal analysis technique that is used to measure weight changes in a material as a function of increasing temperature. As the temperature of the specimen increases, various components are decomposed and the weight percentage of each resulting mass change can be measured [131]. A typical TGA instrument consists of a high precision balance with a pan on which the sample is loaded. The pan is placed into a small electrically heated oven with a thermocouple to measure the temperature, and the mass of the sample is monitored throughout the experiment. The atmosphere is purged with an inert or a reactive gas that flows over the sample and exits through an exhaust. A sample weight or the percentage of the original sample weight, is measured and plotted as a function of either heating time or temperature. This obtained plot is called the TGA curve.

In this work, TGA was performed on a TA SDT 2960 instrument at a heating rate of 10°C/min under a nitrogen atmosphere. After the data was obtained, curves were first converted to ASCII-format and then imported into Origin 8 for further processing. Temperature at 5% weight loss was used as the decomposition temperature (T_d).

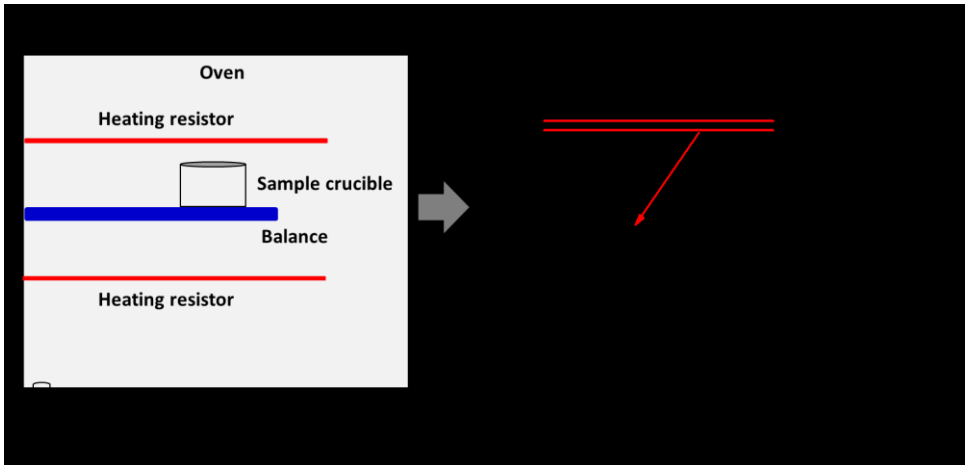

Figure 3.4: (a) Schematic setup for TGA and (b) schematic drawing of the procedure to derive T_d.

Photoluminescence spectroscopy

Photoluminescence spectroscopy is a technique used to measure the light emission from a material under optical excitation. As discussed in Chapter 2, photoluminescence was divided into two categories: fluorescence and phosphorescence. The emission of a photon from the singlet excited state to the ground state is called fluorescence. The average lifetime of fluorescence is only 10^{-9}-10^{-6} seconds. The emission of a photon from the triplet excited state to the ground state is called phosphorescence. The lifetime of phosphorescence is at least 10^{-6} seconds and possible as long as 10^{2} seconds [43, 44, 132, 133]. Because molecules occupy triplet states for a relatively long time during phosphorescence, the molecules have a very high probability of losing excess energy by non-radiative routes such as internal conversion, biomolecular collision, and photodecompositions. Therefore, phosphorescence is not routinely observed at room temperature. One of the most common techniques for observing phosphorescence is accomplished by dissolving the organic materials in an appropriate solvent, then freezing the resulting solution in liquid nitrogen (77 K) to minimize molecular collisions. In a photoluminescence spectroscopy instrument (Figure 3.5), the sample is illuminated with monochromatic light from a Xenon arc lamp, then the light emission from the sample is detected by a photomultiplier. The sample is usually positioned at 90° to the excitation light to minimize the amount of excitation light reaching the detector. The instrument for phosphorescence measurement must be able to discriminate phosphorescence and fluorescence from the sample. Because the lifetime of fluorescence is shorter than that of phosphorescence, this is achieved by incorporating a delay between the exciting source and the sample during measurement.

In this work, photoluminescence spectra were recorded with a luminescence spectrometer

(Hitachi spectrophotometer, F-4600). 60 nm organic films were deposited on quartz by thermal vacuum deposition for measurement. During the fluorescence measurement, photoluminescence excitation (PLE) spectrum was first recorded at the maximum of the PL spectrum, then the PL spectrum was measured at the maximum of the excitation spectrum. This process was repeated until the maxima of excitation and emission remained constant. The phosphorescence spectra were measured in frozen 2-methyltetrahydrofuran (2-MeTHF) matrix at 77 K, and the E_T were calculated from the first peak of the phosphorescence spectra.

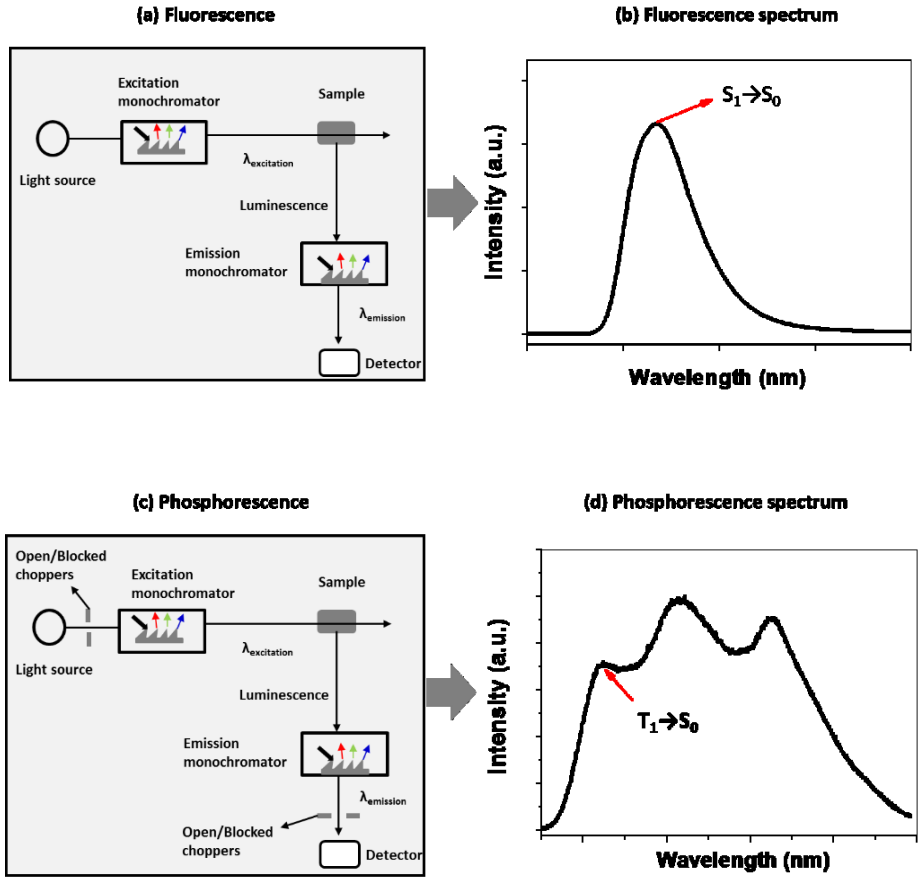

Figure 3.5: (a) Schematic setup for fluorescence spectroscopy and (b) schematic drawing of the procedure to derive the energy of S_1; (c) schematic setup for phosphorescence spectroscopy and (d) schematic drawing of the procedure to derive the energy of T_1.

Ultraviolet and visible absorption spectroscopy

Ultraviolet and visible absorption spectroscopy is a technique used to measure the attenuation of a light beam after it passes through a sample. For the absorption of organic solids, it is the sum of the absorption of each molecule. When a sample is exposed to light energy that matches the energy difference between possible electronic transitions within a molecule, a

fraction of the light energy is absorbed by the molecule and the outer electrons are promoted to the higher energy state orbital. The resulting plot of absorbance versus wavelength is the UV-Vis absorption spectrum.

For UV-Vis absorption spectroscopy, the light source is a combination of halogen and deuterium lamps that provide the ultraviolet and visible radiation. The output from the light source is through a monochromator which splits the incoming light into its components of different wavelengths. The light beams then pass through the sample which is held between a monochromator and a photodetector. A schematic drawing of the UV-Vis absorption setup is shown in Figure 3.6. Radiation across the whole of the ultraviolet and visible range is scanned, and radiation of the same frequency and intensity is simultaneously passed through a reference cell. Photocells then detect the radiation transmitted. The spectrometer records the absorption by comparing the difference between the intensity of the radiation passing through the sample and the reference cell. Experimentally, the efficiency of light absorption at a wavelength λ by an absorbing medium is characterized by the absorbance $A(\lambda)$ or transmittance $T(\lambda)$, which are defined as follows [134]:

$$A(\lambda) = log\frac{I_\lambda^0}{I_\lambda} = -logT(\lambda) \tag{3.2}$$

$$T(\lambda) = \frac{I_\lambda}{I_\lambda^0} \tag{3.3}$$

where I_λ^0 and I_λ are the light intensities (spectral radiant power P_λ) of the beams entering and leaving the sample, respectively.

In this study, UV-Vis absorption spectra were recorded with a PerkinElmer lambda 900 spectrometer. 40 nm thin films were deposited on quartz glass substrate via thermal vacuum deposition for measurement. In order to minimize the absorption from the quartz substrate, the baseline was first recorded with pure quartz and stored, then one pure quartz was replaced by the substrate with thin organic layer and the absorption spectrum of the organic material was recorded. After the data was obtained, curves were first converted to ASCII-format and then imported into Origin 8 for further processing. The energy gap E_g was determined by the onset of the UV-Vis spectra.

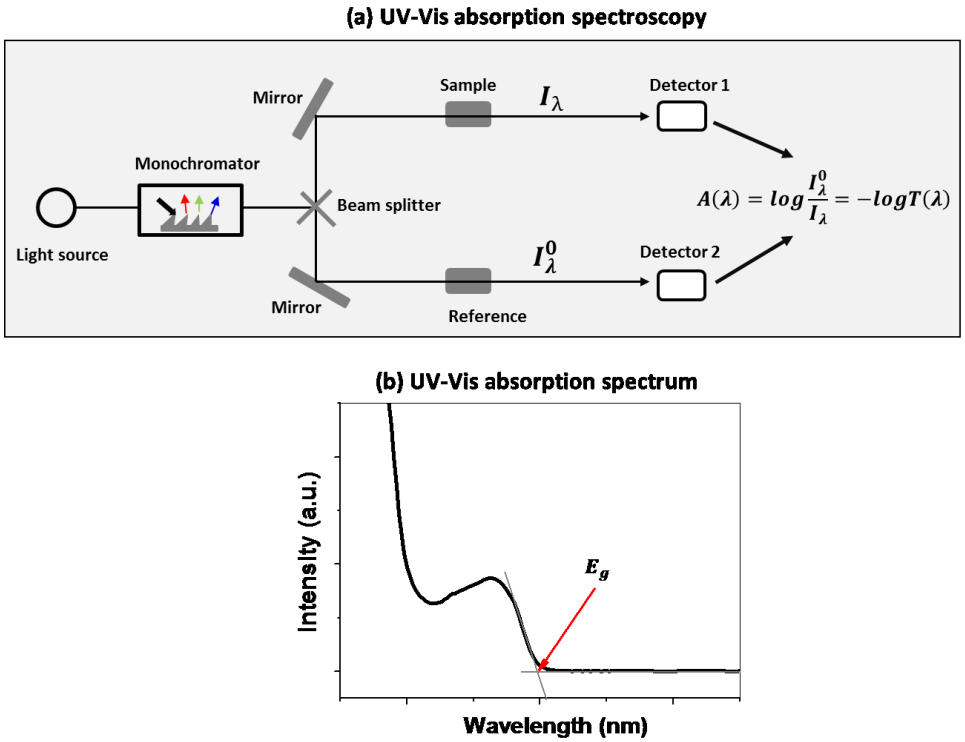

Figure 3.6: (a) Schematic representation of UV-Vis absorption spectroscopy setup and (b) schematic drawing of the procedure to derive the energy of E_g.

Photoelectron spectroscopy

Photoelectron spectroscopy is a surface sensitive technique used to determine the distribution of electronic states of a material [135, 136]. Based on Einstein relation [137], a sample is excited by an incident light beam with energy $h\upsilon$, then photoelectrons are emitted from the sample if their kinetic energy E_{kin} is larger than the binding energy of the material E_B:

$$E_{kin} = h\upsilon - E_B \tag{3.4}$$

where h is the Plank constant; υ is the frequency of the radiation; and E_B is the binding energy against the vacuum level. This is the photoemission of an electron by electromagnetic radiation or photoionization of a sample. For a solid surface, the binding energy E_b is conventionally measured with respect to the Fermi level rather than to the vacuum level, and the former equation is written in the following form:

$$E_{kin} = h\upsilon - E_b - WF \tag{3.5}$$

where, WF is the work function of the material and represents the energy barrier that prevents an electron at the Fermi level from escaping the solid. Depending on the excitation photon energies used, photoelectron spectroscopy is subdivided into ultraviolet photoelectron spectroscopy (UPS) with the exciting light source in the ultraviolet range, and X-ray photoelectron spectroscopy (XPS) with X-rays as the exciting radiation source. The energy of

the ultraviolet light source in UPS is normally between 10 and 100 eV, thus UPS releases valance electrons bound in the outer shells of atoms, molecules, and molecular solids. Hence UPS is used to determine the position and shape of the HOMO level of a molecule or molecular solid [138, 139]. The energy of X-ray source is typically in the range between 100-200 eV and 2000 eV, thus XPS is predominantly focused on core level electrons [138, 140].

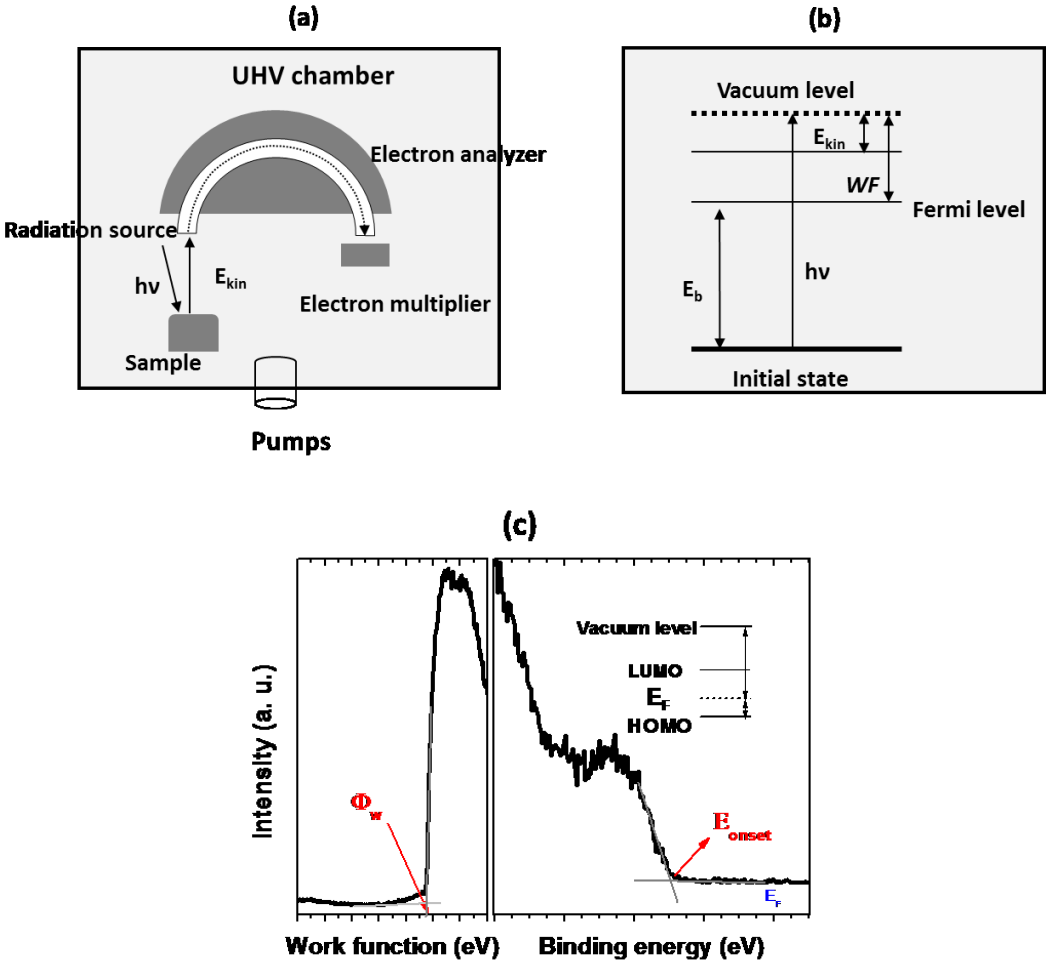

Figure 3.7: (a) Schematic representation of UPS system; (b) corresponding energy levels; and (c) derivation procedure. Note: the binding energy refers to the Fermi level.

In this study, the ionization energy of the host material was measured by UPS. The PES setup used in this work was a KRATOSAXIS ULTRA DLD supplied by KRATOS Analytical. The instrument was incorporated in an ultra-high vacuum chamber at a base pressure of 10^{-9} mbar. The He-I excitation line (21.22 eV) of a He discharge lamp was used as a light source for excitation. The kinetic energy of the electrons emitted from the illuminated sample was resolved with a hemispherical sector analyzer and a multi-channel electron multiplier was utilized for electron detection. 10 nm thin organic films deposited by thermal vacuum on ITO glass were used for investigation. After measurements were taken, spectra were first converted

to ASCII-format and then imported into Origin 8 for further processing.

Transient photoluminescence decay spectroscopy

The Transient photoluminescence decay technique is used to measure the exciton decay dynamics of luminescent molecules with a pulsed light excitation. The PL lifetime is one of main characteristics of luminescent emitters. It should be noted that the emission of a photon occurs as rapidly as the absorption of a photon (10^{-15} s). However, excited molecules stay in the low excited state for a certain time (a few tens of picoseconds to a few hundreds of microseconds, depending on the type of molecule) before emitting a photon or undergoing any other de-excitation process (e.g., internal conversion, intersystem crossing). Thus, after the excitation of a population of molecules by a very short pulse of light, the light intensity decreases exponentially with time. The PL lifetime also influenced by the chemical composition of its environment. Additional processes like Förster transfer, charge carrier transfer, or molecular rotation also have an effect on the decay kinetics. Therefore, lifetime changes can be exploited to gain information about the local chemical environment or to follow the reaction mechanism. In this technique, different setups can be built to measure transient PL decay. A common procedure is to illuminate the sample with an extremely short pulsed light source, then detect the resulting luminescence with a single-photon counter (or streak camera, or other relevant device) and then measure the subsequent decay in PL as a function of time. The general setup for this technique is shown in Figure 3.8. For the sake of comparison against an accurate measurement of the mean lifetime τ of the sample, an extremely fast flash (with duration much shorter than lifetime τ) should be used.

In this study, transient PL decays were detected by a single photon counting spectrometer from Horiba Jobin Yvon. The excitation source was a pulsed laser diode (nanoLED-300, Horiba Scientific) which emit at 293 nm with a <1 ns pulse. During the measurement, the pulsed laser triggered a time-amplitude converter (TAC) to “start” while the pulsed laser excited the PL of the sample. Part of the PL emission photons were passed through a long pass filter and mono-chronometer into a single-photon counter. The first emitted photon was detected by the PMT and sent a “stop” signal to the TAC. The experiment was repeated at the repetition rate of the laser (25 KHz). Given these statistics, a histogram with the order of 10^4 photon counts versus time was generated corresponding to the PL decay of the sample. PL decay measurements were performed at room temperature under a nitrogen atmosphere. After the data were obtained, curves were first converted to ASCII-format and then imported into Origin 8 for further processing. The data consisted of making a semi-logarithmic plot of the signal intensity (in arbitrary units) versus time. In some cases, additional analysis (i.e., lifetime

calculation) was done with decay analysis software (DAS 6, Horiba) by calculating the slope, which was proportional to the reciprocal of the desired mean lifetime.

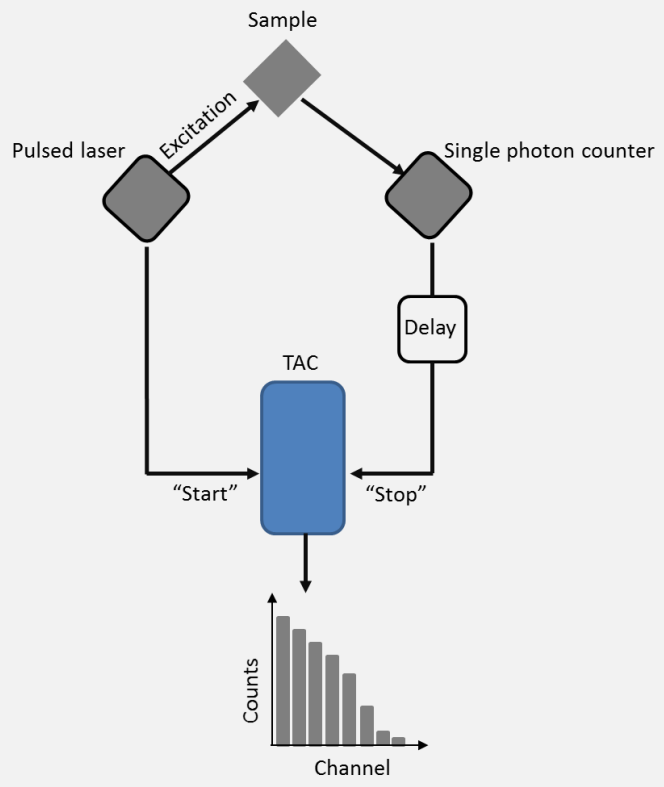

Figure 3.8: Schematic representation of the transient PL decay experiment setup.

3.1.3 Characterization of OLEDs

In order to comprehensively characterize OLEDs, their electrical and emission characteristics have to be investigated. The measurement setups for OLEDs characterization are explained below.

Current-voltage-luminance

Current-voltage-luminance characterizations of OLEDs were performed with a measurement robot. The electrical performance of OLEDs was characterized with an electrical source meter (SMU 2400, Keithley Inc.) which supplied a defined voltage V and detected the current I through the device. The current density j was obtained from the current I divided by the active area A of the device; simultaneously, the electroluminescence signal in the normal direction to the device surface (θ=0°) was detected with a SpectraScan spectroradiometer (PR655, Photo Research Inc.). The meter uses a calibrated Si photodiode to detect the light and convert the diode photon response into a luminance value. The measurement quantity is defined as the spectral radiant intensity per unit area I_0^{λ} (W/m^2) of the OLEDs in the forward direction (θ=0°) and the forward luminesce L_0 was obtained as follows:

$$L_0 = K_m \int_{380\,nm}^{780\,nm} I_0^{\lambda}(\lambda) V(\lambda) d\lambda \ \ [\mathrm{cd/m^2}] \tag{3.6}$$

where k_m=683 lm/W is the conversion coefficient and $V(\lambda)$ is the photopic spectral luminous efficiency function. A computer program based on Labview (National Instruments) was used to collect the experimental data from SMU 2400 and PR655.

Emission spectra

The emission spectrum of OLEDs may shift with increasing driving current due to changes in the position of the recombination zone. The spectrascan spectroradiometer (PR655, Photo Research Inc.) was used to record the emission spectra under different driving voltage.

Efficiency measurement

Three types of efficiencies are used to evaluate OLEDs efficiency in this study: current efficiency (η_C), power efficiency (η_{LE}) and external quantum efficiency (η_{EQE}). The efficiencies can be estimated from current-voltage-luminance measurement data assuming OLEDs exhibit Lambertian angular characteristic behavior, which spatial distribution of the emitted radiant intensity is given by:

$$I(\theta) = I_0 cos(\theta) \tag{3.7}$$

where I_0 is the radiant intensity in the forward direction and θ is the azimuthal angle.

The current efficiency (in cd/A) is defined as the ratio of the luminous intensity normally in the perpendicular direction to the substrate to the current flowing through the OLED [5]:

$$\eta_c = \frac{L_0}{j} \ \ [\mathrm{cd/A}] \tag{3.8}$$

where L_0 is the luminance in the forward direction and j is the current density passing through the device.

The power efficiency (in lm/W) is defined as the ratio of total light output (L_P) in lumens to electrical input power in Watts, and can be calculated from current efficiency η_c and the driving voltage [5]:

$$\eta_P = \frac{L_P}{IV} = \frac{\int\int K_m V(\lambda) I(\lambda,\theta) d\lambda d\theta}{IV} \tag{3.9}$$

where K_m is the maximum luminous efficiency for the photonic version, $I(\lambda, \theta)$ is azimuthal dependent spectral radiant intensity at a discrete current I, and $V(\lambda)$ is the spectral luminous efficiency function of the human eye. Assuming that OLEDs have a Lambertian emission from the device, where the light angular distribution $I(\lambda, \theta)$ within the half-sphere in the forward direction is equal to 1, the following holds:

$$f_D = \frac{1}{\pi I_0} \int_0^{\pi/2} \int_{-\pi}^{+\pi} I(\lambda,\theta) sin\theta d\lambda d\,\theta = 1 \tag{3.10}$$

Thus, the power efficiency calculation can be simplified to:

$$\eta_P = \frac{L_P}{IV} = \frac{\pi L_0}{jV} = \eta_c \frac{\pi}{V} \quad [\text{lm/W}] \tag{3.11}$$

The EQE (in %) is defined as the number of emitted photons from OLEDs divided by the number of injected charge carriers [5, 141]:

$$\eta_{ext} = \frac{\eta_P}{\eta_e} \times 100\% = \frac{\int\int \frac{2\pi I(\lambda,\theta)}{hc/\lambda} sin\theta d\theta d\lambda}{I/e} \times 100 \tag{3.12}$$

where $I(\lambda, \theta)$ is the azimuthal dependent spectral radiant intensity at a discrete current I, h is Planck constant, and c is the light velocity in vacuum. The total number of injected charge carriers are calculated from the OLEDs current divided by electron charge e.

3.2 Materials

The organic semiconductors used in this study are classified into charge injection materials, charge transport materials, and fluorescent or phosphorescent emitter materials. In addition to the molecular structures, a brief summary of their physical properties (HOMO and LUMO levels, triplet energy levels) is provided below. The properties of these organic materials (i.e., exciton dynamics) are discussed in detail in Section 4. Reference to key publications was given as sources for the data and for examples of application of the materials.

3.2.1 Electrode materials

The OLEDs studied throughout in this work were built in bottom emitting configuration. This means that the light was coupled out from a glass substrate. The devices were fabricated on glass substrates pre-coated with patterned ITO according to the layout shown in Figure 3.9. The thickness of ITO layer was around 100 nm and it had a sheet resistance of approximately 20 Ω/sq. Between the ITO layer and the glass, about 200 nm SiO_2 was incorporated as a passivation layer (HuaYu Co.). To clean the ITO glass substrates, they were first washed and mechanically scrubbed, then they were rinsed with copious amounts of de-ionized water (>18 M) and blown dry under a stream of nitrogen. They were then further clean sonically in acetone, ethanol, and isopropanol for 10 minutes each. The clean ITO glass substrates were stored in a sealed container containing pure isopropanol. A variety of surface treatments were used in this work. For ITO/MoO_3 and ITO/HAT-CN, the ITO substrates were put into an UV-ozone cleaner for 15 min prior to use to increase the ITO work function by increasing the oxygen concentration of the surface. The work function of the ITO/MoO_3 and ITO/HAT-CN were around 6.9 eV and 5.6 eV, respectively [142, 143]. For ITO/PEIE, no treatment was performed and its work function was about 3.3 eV [144]. On the opposite side, a 140 nm Al layer with work function about 4.1 eV was used as a reflective top cathode [76]. The work functions of

the investigated electrode materials are summarized in Table 3.1.

Table 3.1: Electrode materials and their work functions

Material	Work function	Comment
ITO/MoO_3	~ 6.9 eV	Anode for PhOLEDs and hole-only device
ITO/HAT-CN	~ 5.6 eV	Anode for TADF OLEDs and hole-only device
ITO/PEIE	~ 3.3 eV	Anode for electron-only device
Al	4.1 eV	Cathode

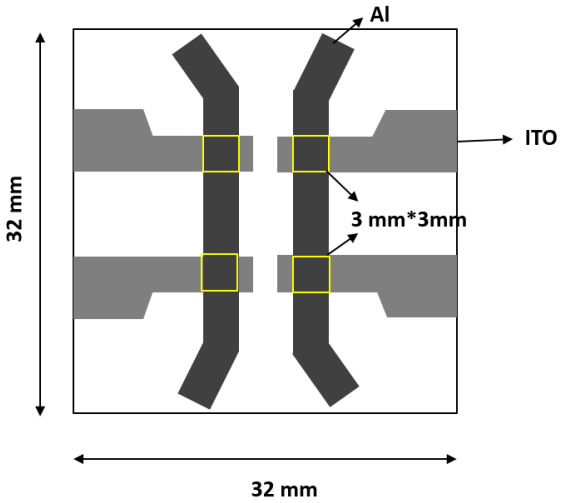

Figure 3.9: Layout of the pre-coated ITO on a 32 mm×32 mm glass substrate. Yellow squares denote the overlap of bottom ITO anode and top Al cathode (3 mm×3 mm).

3.2.2 Charge carrier injection materials

In order to more effectively inject charge carriers from the electrodes, thin injection layers were used in OLEDs. The injection layers were MoO_3 or HAT-CN for hole injection and Liq for electron injection [145, 146]. The molecular structures of HAT-CN and Liq are shown in Figure 3.10.

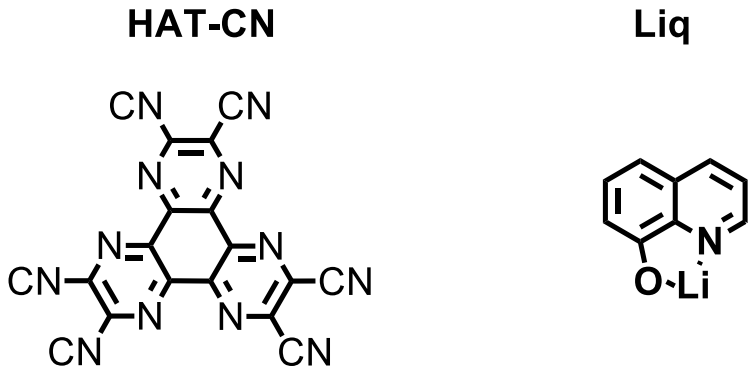

Figure 3.10: Chemical structures of HAT-CN and Liq.

3.2.3 Charge carrier transporting and charge carrier blocking materials

Before holes and electrons can meet in the emission layer, they must transport through the outer organic layers. In this study, di-[4-N,N-ditolyl-amino-phenyl] cyclohexane (TAPC) and 4,4',4"-tris(N-carbazolyl)-triphenylamine (TCTA) were used as hole transport layers and tetra(m-pyrid-3-yl)phenyl-[1,1']-biphenyl (TmPyPB) was used as electron transport layer [147-149]. All these materials were supplied by Lumitec. To prevent hole leakage from the emitting layer, the HOMO level of the hole blocking material must by noticeably higher than that of the emitting material in order to ensure a large energy barrier that the holes cannot overcome easily. The hole blocking material also must have a low hole mobility to effectively hinder hole transport. TmPyPB was used for this purpose; for the similar reasons, TAPC or TCTA was used as electron blocking materials. For PhOLEDs and TADF OLEDs, the triplet exciton diffusion length was same order of magnitude of the emitting layer thickness, so the excitons must be confined in the emitting layer. TAPC, TCTA and TmPyPB have higher triplet energies than that of the emitting materials, thus they can also be used as exciton blocking layers in OLEDs. Their corresponding chemical structures are shown in Figure 3.11.

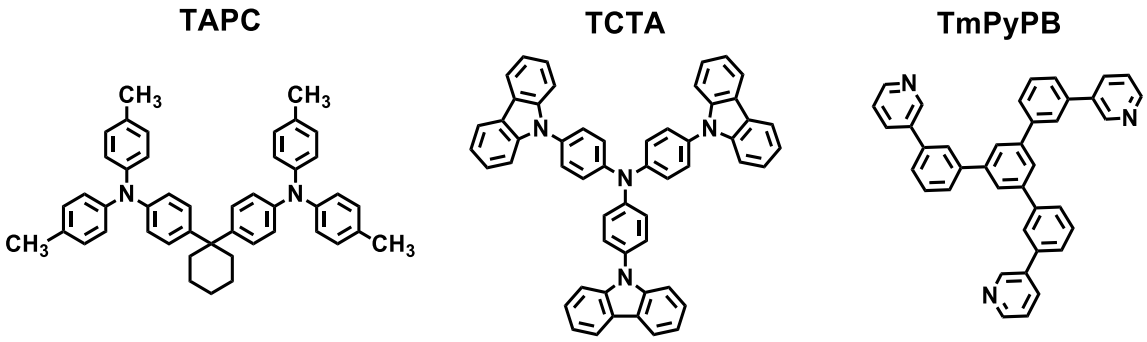

Figure 3.11: Chemical structures charge transport materials

3.2.4 Fluorescent and phosphorescent emitter materials

In this work, two highly efficient emitters were used in this study: FIrpic and green TADF emitter 1,2,3,5-tetrakis(carbazol-9-yl)-4,6-dicyanobenzene (4CzIPN) (purchased from Lumtec.) [12, 19]. Both were diluted in corresponding host material to avoid unwanted quenching [16]. The chemical structures of the emitters are depicted in Figure 3.12.

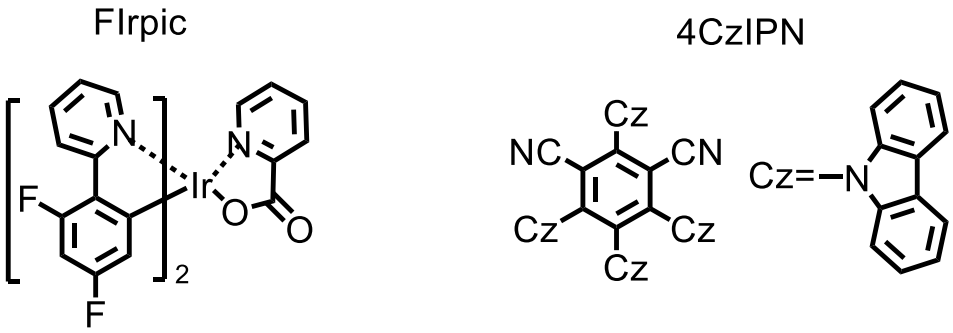

Figure 3.12: Chemical structures of phosphor and TADF emitters.

As discussed in Chapter 2, the electronic structure of organic molecules is great important for securing high performance OLEDs. Appropriate HOMO and LUMO levels of the host were required to realize efficient charge carrier recombination in the emitting layer. And appropriate triplet levels of the host and guest were required to achieve charge carrier transfer and good exciton confinement on the emitter sites. Figure 3.13 summarizes the HOMO/LUMO levels and triplet levels of the organic materials used in this study.

3.2.5 Host materials

Seven host materials were used in this study. 3,3-di(9H-carbazol-9-yl) biphenyl (*m*CBP) were purchased from Lumtec and the other six host materials [3,3'-bis(dibenzo[b,d]thiophen-4-yl)-1,1'-biphenyl (*m*BPDBT), *m*DCBP, *m*DCP, *m*DCTP, *m*D2CBP, and *m*DC2BP] were synthesized by the project partner (Dr. Shoucheng Dong) at Soochow University.

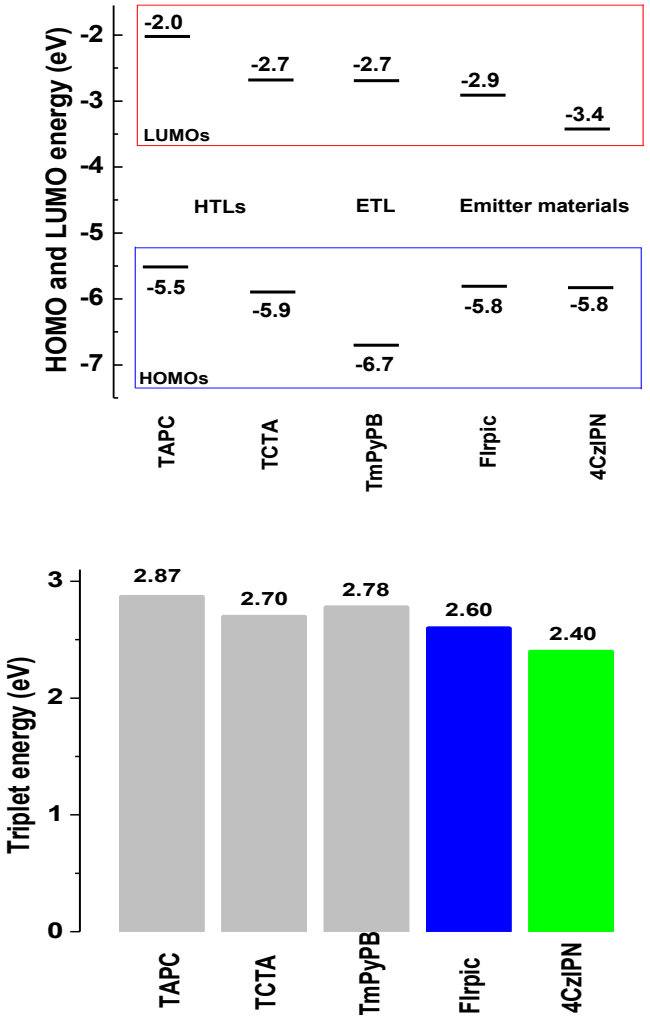

Figure 3.13: (a) HOMO and LUMO levels and (b) triplet energies of organic materials used in this study. Note: The materials were arranged according to their functionality; Hole transport materials, electron transport materials, and emitters are shown from left to right.

Chapter 4

Results and Discussion

In this chapter, a series of carbazole/dibenzothiophene derivatives were investigated as host materials for blue PhOLEDs and green TADF OLEDs. In the first section, a host material, with one carbazole and one dibenzothiophene moiety connected by biphenyl spacers, while biphenyl serving as a linkage between them and through the *meta* position, had been investigated. In the second section, three host materials with carbazole and dibenzothiophene moieties connected by extended phenyl spacers are investigated. And in the last section, three host materials with different ratios of carbazole to dibenzothiophene moieties and connected by biphenyl spacers were investigated. The physical properties of these host materials were comprehensively characterized and the device performance of blue PhOLEDs and green TADF OLEDs based on them were investigated in detail. The relevant conclusions derived from the investigations of the different molecular systems were presented in the appropriate sections.

4.1 Systematic study of carbazole/dibenzothiophene derivatives as host materials in modern OLEDs

4.1.1 Introduction

OLEDs have been rapidly developed since the outstanding contribution of Tang, who demonstrated efficient OLEDs with a single heterojunction structure in 1987 [3]. They are fascinating for the next generation of flat-panel displays and illumination sources due to several advantages qualities, e.g., low power consumption, low weight, high luminous efficiency, full-color capability, wide viewing angle, and high contrast. In OLEDs, under electrical excitation, charge carrier recombination can produce singlet and triplet excitons in a 1:3 ratio. According to the spin statistics, conventional fluorescent OLEDs can only harvest 25% singlet excitons. All triplet excitons (75% of the formed excitons) decay non-radiatively, so the maximum η_{int} is limited to 25% for traditional fluorescent molecules.

To improve η_{int} with the harvesting triplet excitons, several different approaches have been

proposed to date. The first notable breakthrough was made by Forrest, they proposed the concept of PhOLEDs utilized phosphors, which theoretically allowed η_{int} up to 100% [11, 13, 101]. In PhOLEDs, the generated singlet excitons can be converted into triplet excitons via intersystem conversion fast and efficient, then all the triplet excitons can radiative decay to ground state due to the strong spin-orbit coupling effect of the central heavy metal. Recently, Adachi demonstrated an alternative route to harvest triplet excitons by utilizing a TADF process that can achieve nearly 100% η_{int} [12, 52, 150-153]. In TADF OLEDs, triplet excitons can be up-converted to singlet state through reverse intersystem crossing due to a small energy gap between the lowest excited singlet state and the lowest excited triplet state; light emission is then extracted as a delayed fluorescence from the transition of S_1 to the ground state ($S_1 \rightarrow S_0$ transition).

Generally, efficient PhOLEDs and TADF OLEDs contain a doped emitting layer, which consists of a dopant dispersed in a suitable host matrix to prevent unwanted quenching pathways for triplet excitons such as triplet-triplet annihilation or triplet-polaron quenching [16]. Meanwhile, the high energy host donors transfer excitons to the highly efficient dopant acceptors through Förster or Dexter transfer, resulting in a high efficient emission from the dopant. Therefore, the host materials are quite important to determine the overall OLEDs performance.

In principle, an ideal host material should possess certain criteria. First, as the major component of the emitting layer, matching HOMO/LUMO levels of host materials with the adjacent layers and emitters are required to ensure effective charge injection. The HOMO of the host materials should be deeper than that of the emitters, while the LUMO of the host materials should be shallower than that of the emitters. Second, depends on the type of emitting dopant, either singlet or triplet energies of the host should higher than that of the dopant to guarantee efficient forward energy transfer from host to dopant and to confine the triplet excitons on the dopant. For the host materials in blue OLEDs, the lowest triplet energies higher than 2.6 eV was preferred for host as the lowest triplet energy of the typical sky blue triplet emitters is ca. 2.6 eV. Good charge carrier transport property is another important characteristic of host materials because positive and negative charge carriers are required to be balanced in OLEDs, thus leads to high efficiency and low efficiency roll-off. So host materials that contain both hole transporting and electron transporting moieties are utilized to facilitate charge carrier balance. Good thermal stability, simple structure, and facile preparation are also necessary in terms of industrial manufacture. The use of one single host for both high performance

PhOLEDs and TADF OLEDs would significantly facilitate the development of OLEDs.

Phosphors and TADF emitters have different HOMO/LUMO levels and singlet/triplet energies, which makes it rather challenging to develop efficient PhOLEDs and TADF OLEDs using the same host material. In the search for such highly efficient host materials, organic chemists have focused on a limited range of units. From the classic hole transporting host, carbazole has been considered as an important constructing unit in the design of host since CBP was reported [19]. Its strong electron donating nature ensures hole injection and endows carbazole-derivatives with decent hole mobility, and it is made up of only aromatic moieties with high bond dissociation energy and has a high triplet energy (3.0 eV), that leaving abundant molecule structural modification possibility. To obtain high triplet energy for blue host, carbazole-based derivatives always have less conjugative configuration such as twist linkage or non-conjugative linkage. Many high-performance PhOLEDs and TADF OLEDs based on them have been obtained [20-28]. Another heterocyclic unit similar to carbazole, dibenzothiophene, was recently utilized to construct new host material. It has high triplet energy (3.04 eV), like carbazole, but more neutral molecular structure. Its highly conjugated structure allows the delocalization of both injected holes and electrons, as well. According to previous reports on dibenzothiophene-derivatives as host materials, these compounds exhibit high triplet energies (> 2.7 eV) and show excellent performance in PhOLEDs and TADF OLEDs [29-33].

Is it possible to construct host materials with carbazole and dibenzothiophene units? Bearing in this in mind, in this study, *m*DCBP was designed to be a high performance host material. *m*DCBP has one carbazole and one dibenzothiophene unit, while biphenyl was introduced as a linkage between them through the *meta* position. The physical properties of this host material were comprehensively characterized and the device performance of blue PhOLEDs and green TADF OLEDs based on it were investigated in detail. All the characterizations were comparatively analyzed with corresponding carbazole or dibenzothiophene counterparts bearing same molecular configuration and with well-established properties. Fundamental principles on design strategies of host materials and the common relationship between molecular structure and optoelectronic properties based on carbazole/dibenzothiophene moieties were revealed in this study.

4.1.2 Molecular synthesis

The host material *m*DCBP was synthesized by the project partner (Dr. Shoucheng Dong) at

Soochow University. The synthesis was straightforward with a classic Suzuku-Miyaura reaction. Scheme 4.1.1 illustrates the synthesis route of *m*DCBP: 4-(3-bromophenyl) dibenzothiophene (1.00 g, 2.95 mmol), (3-(9H-carbazol-9-yl) phenyl) boronic acid (1.11 g, 3.87 mmol) were dissolved in tetrahydrofuran (THF)/2 M K_2CO_3 (45 ml, 3/1, v/v) in a Schlenk tube under argon, then the resulting mixture was refluxed for 12 h. After cooling to room temperature, the organic layer was collected and annealed to remove the solvent. The crude product was purified via column chromatography on silica gel with dichloromethane/petroleum (1/5, v/v) as eluent, followed by recrystallization from ethyl acetate/petroleum and vacuum sublimation successively. The final product was a white powder (1.10 g, 74.3 %). ^{1}H NMR (400 MHz, CDCl3) δ (ppm): 8.14-8.21 (m, 4H), 8.07 (t, J = 1.6 Hz, 1H), 7.92 (t, J = 1.6 Hz, 1H), 7.66-7.85 (m, 5H), 7.40-7.63 (m, 10H), 7.30 (t, J = 6.8 Hz, 2H). ^{13}C NMR (100 MHz, CDCl3) δ (ppm): 143.0, 141.5, 141.1, 140.9, 139.7, 138.8, 138.5, 136.8, 136.5, 136.0, 130.7, 130.6, 129.7, 127.9, 127.3, 127.1, 127.0, 126.4, 126.2, 126.0, 125.4, 124.7, 123.6, 122.9, 122.0, 120.9, 120.5, 120.2, 110.1. MS (EI): m/z 501.2 (M+). Anal. calcd for $C_{36}H_{23}NS$ (%): C 86.19, H 4.62, N 2.79; found: C 85.88, H 4.45, N 2.68.

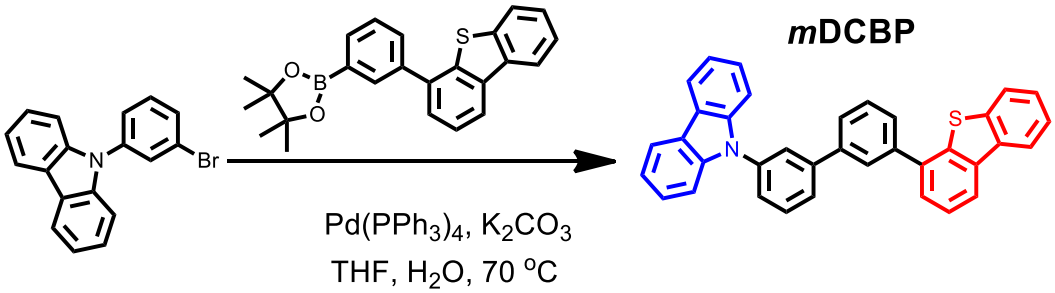

Scheme 4.1.1: Synthesis of carbazole/dibenzothiophene derivative.

4.1.3 Fundamental physical properties

Quantum chemical calculations

To understand the molecule structure-property relationship of *m*DCBP at the molecular level, the HOMO and LUMO orbital spatial distributions were obtained by the density function theory calculations at the (B3LYP)/6-31G (d) level with the Gaussian program [154]. Figure 4.1.1 shows the HOMO and LUMO distributions of *m*BPDBT, *m*CBP, and *m*DCBP. The HOMO of *m*DCBP was mainly distributed over the carbazole unit and adjacent phenyl ring due to the strong electron-donating nitrogen unit of carbazole. Whereas the LUMO of *m*DCBP was localized on the benzene ring and dibenzothiophene moiety (phenyl-dibenzothiophene unit) due to the electron-withdrawing sulfur group. These indicated that carbazole is a hole transport

moiety and dibenzothiophene is an electron transport moiety in *m*DCBP. Therefore, the *m*DCBP would exhibits electron accepting properties as well as hole accepting properties from charge transport materials. In the case of *m*BPDBT and *m*CBP, the two carbazole or dibenzothiophene moieties played the roles of hole transport property, thus the *m*DCBP was expected to have lower hole transport property than *m*BPDBT or *m*CBP.

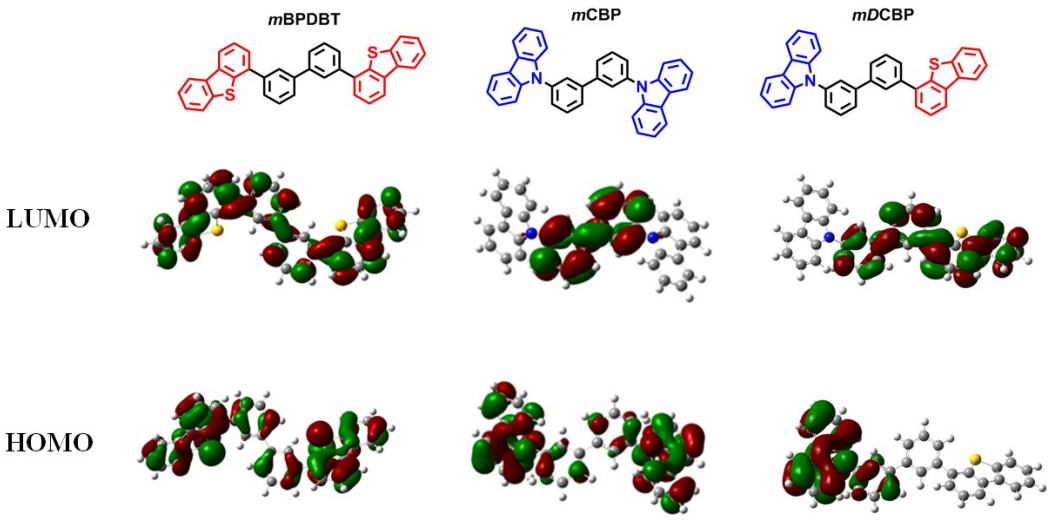

Figure 4.1.1: HOMO and LUMO spatial distributions of carbazole/dibenzothiophene derivatives.

Thermal analysis

The thermal stability of the host materials, which is closely related with the device stability, was characterized by TGA and DSC. DSC and TGA thermograms of *m*BPDBT, *m*CBP, and *m*DCBP are shown in Figure 4.1.2.

The glass transition temperature of *m*DCBP was observed at 88 ˚C, which was similar to that of *m*BPDBT (87˚C). *m*CBP did not exhibit any obvious glass transition process in the DSC traces due to its tendency to crystallize. The glass transition temperature was obviously higher than some carbazole-based host materials, such as CBP (62˚C) or *m*CP (60˚C) [19, 155].

All the decomposition temperatures of these materials were observed over 400˚C during TGA: which were 436˚C for *m*BPDBT, 405˚C for *m*CBP, and 430˚C for *m*DCBP. Decomposition temperature is mainly determined by the material's molecular weight. The thermal analysis results indicated that *m*DCBP possesses good thermal stability, which could improve the film morphology and reduce the possibility of phase separation upon heating; in other words, *m*DCBP could be used as OLEDs component in long-lifetime devices.

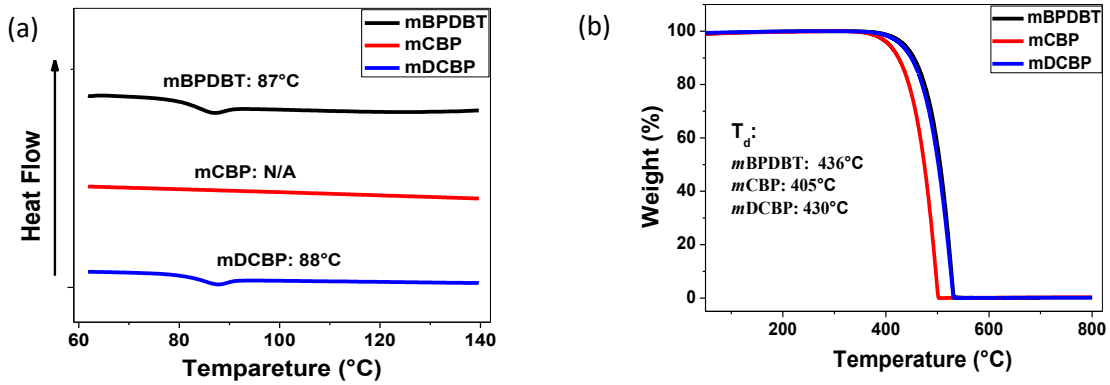

Figure 4.1.2: (a): DSC traces and (b) TGA traces recorded at a heating rate of 10˚C min^{-1}.

Photophysical properties

The photophysical properties of *m*BPDBT, *m*CBP, and *m*DCBP were investigated by means of UV-Vis absorption, PL, and phosphorescence spectra, as shown in Figure 4.1.3. The UV-Vis absorption and PL spectra were obtained from vacuum evaporated thin films (60 nm) and the phosphorescence spectra were measured in 2-MeTHF at 77 K. *m*DCBP showed similar absorption spectra to *m*CBP, the relatively weak shoulder peaks at ca. 355 nm can be attributed to the n-π* transitions of the carbazole group [30, 156]. For *m*BPDBT, the relatively weak peak at around 345 nm can be attributed to the n-π* transitions of the dibenzothiophene group [22]. The optical-energy bandgaps were determined by the onset of UV-Vis absorption spectra. The absorption edges of the spectra for *m*BPDBT, *m*CBP and *m*DCBP were 361 nm, 363 nm, and 365 nm, which corresponding to bandgaps of 3. 44 eV, 3.41 eV, and 3.40 eV, respectively. All compounds exhibited similar violet fluorescence. The maximum PL emission peaks of *m*BPDBT, *m*CBP, and *m*DCBP were observed at 368 nm, 373 nm, and 370 nm, respectively. The singlet energy of *m*DCBP was 3.35 eV, which is high enough for energy transfer to a blue or green emitter. A narrow full-width-at-half-maximum (FWHM) ranging from 41 nm of *m*BPDBT through 61 nm of *m*CBP to 47 nm of *m*DCBP were observed. The emission spectra of *m*DCBP was well overlapped with the absorption spectra of typical blue and green emitters, indicating that energy transfer from the host to the dopant would be quite efficient [157-159]. All these materials exhibited broad phosphorescent spectra; the triplet energies were calculated by the first emission peak of phosphorescence spectra ($T_1^{v=0} \rightarrow S_0^{v=0}$). The triplet energies of *m*BPDBT, *m*CBP, and *m*DCBP were 2.74, 2.85 and 2.75 eV, respectively. Again, all of them are sufficient enough to be used as blue and green hosts and to prevented triplet energy back transfer (as discussed in further detail below).

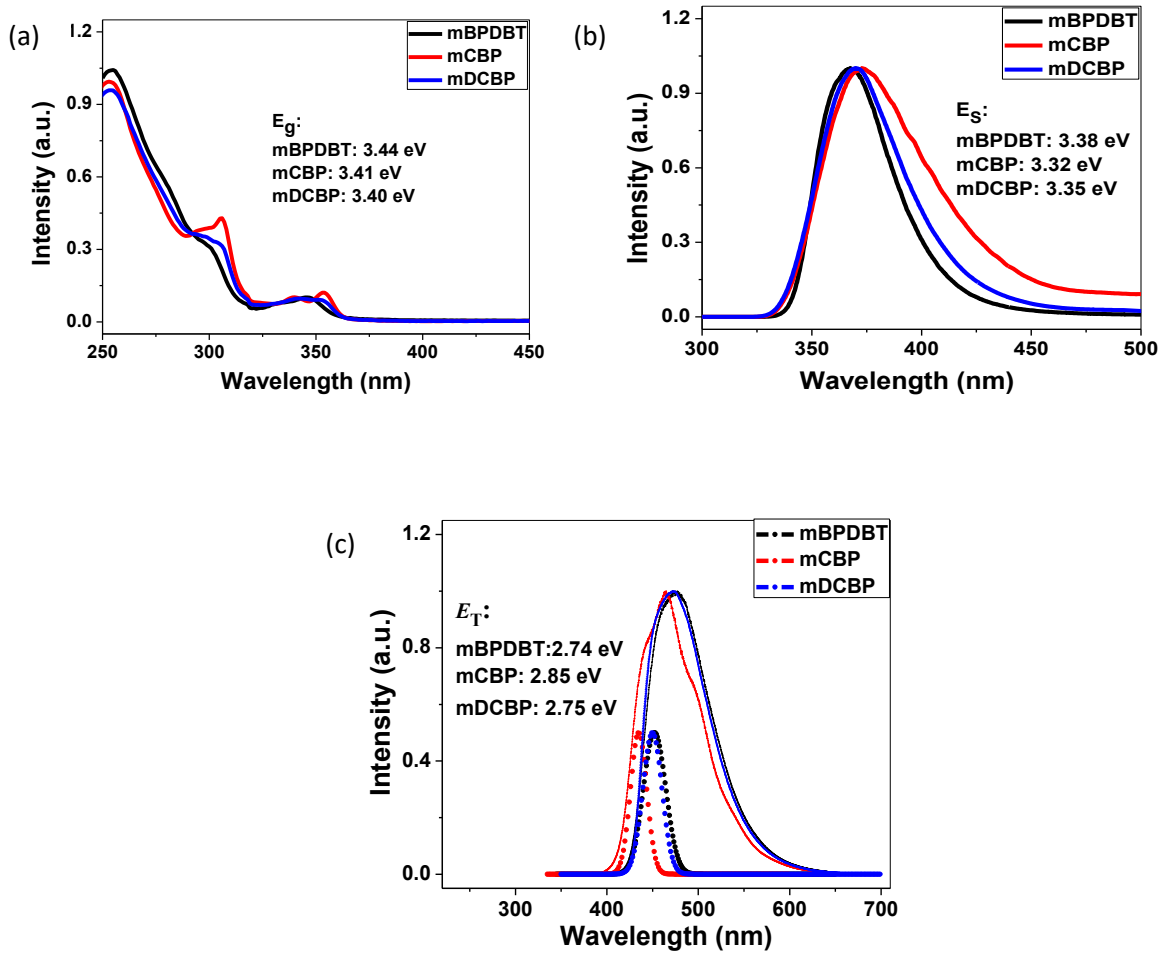

Figure 4.1.3: (a) UV-Vis absorption spectra; (b) PL spectra; (c) phosphorescence spectra measured in frozen 2-MeTHF matrix at 77 K.

HOMO/LUMO levels

For host materials, appropriate HOMO and LUMO levels is essential to the efficient injection of charge carriers into the emitting layer. The HOMO levels of the materials were determined by ultraviolet photoemission spectroscopy, as shown in Figure 4.1.4. The HOMO levels of *m*BPDBT, *m*CBP, and *m*DCBP were -6.20 eV, -6.05 eV and -6.01 eV, respectively. The optical LUMO levels were calculated using HOMO and optical bandgap E_g from UV-Vis absorption edge in the solid films, according to the equation E_{LUMO} (eV) = (E_{HOMO}+E_g) eV. The LUMO levels of *m*BPDBT, *m*CBP, and *m*DCBP were -2.76 eV, -2.64 eV, and -2.61 eV, respectively. All the physical data of these compounds are summarized in Table 4.1.1.

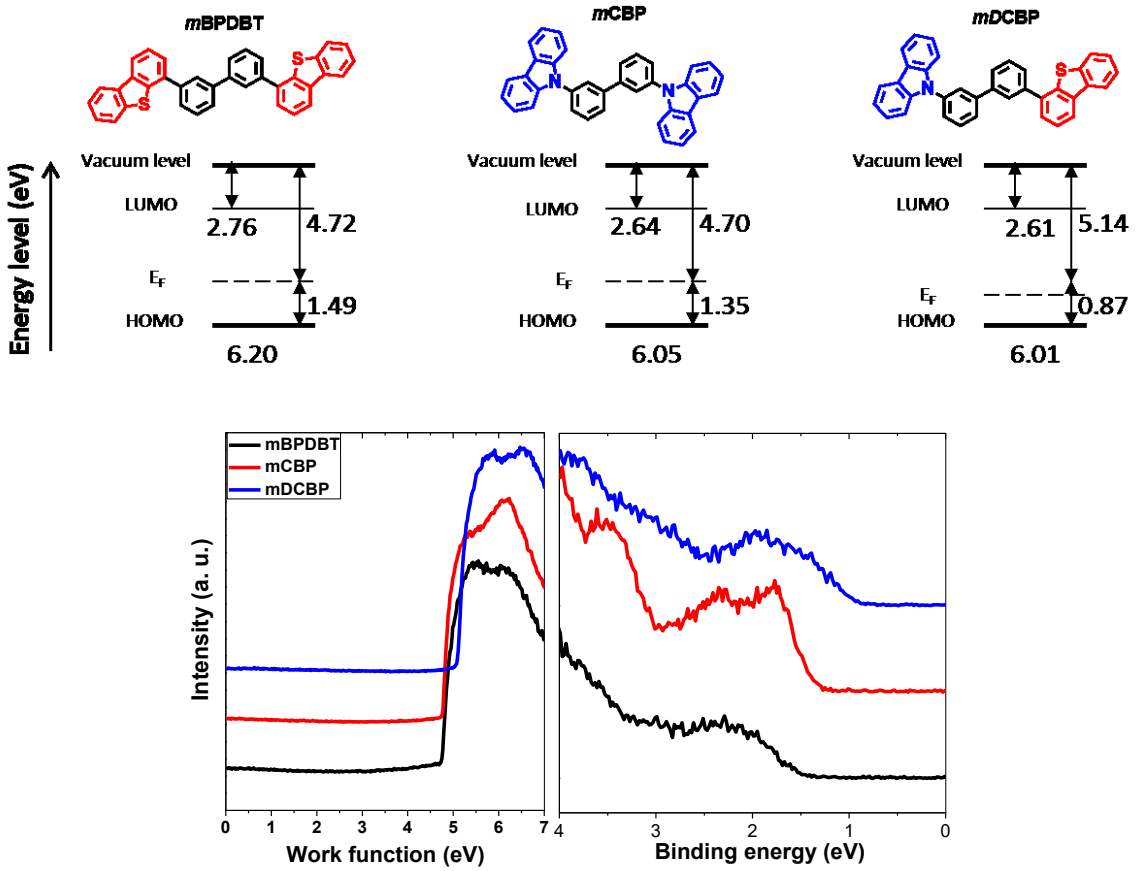

Figure 4.1.4: UPS spectra of carbazole/dibenzothiophene hybrids.

Carrier-transport properties

To evaluate their charge carrier transport ability, single-carrier devices were fabricated and characterized. The hole-only device had the following structure: ITO/MoO_3 (10 nm)/host (100 nm)/MoO_3 (10 nm)/Al and the electron-only device had the following structure: ITO/PEIE/BCP (15 nm)/host (100 nm)/BCP (15 nm)/Liq (2.5 nm)/Al (host = *m*BPDBT, *m*CBP or *m*DCBP). As shown in Figure 4.1.5, at the same electrical field, the electron current densities were much lower than the hole current densities in the single carrier device. In the hole-only devices, the hole current density for *m*DCBP was lower than that of *m*CBP or *m*BPDBT devices, indicating that *m*DCBP had the lowest hole transport properties. These results agreed well with the HOMO/LUMO spatial distributions. The HOMO levels distributed on two carbazole or two dibenzothiophene units in *m*CBP or *m*BPDBT, which were more suitable for hole hopping between adjacent molecules. In the electron-only devices, *m*BPDBT and *m*DCBP showed higher current density than *m*CBP. Compared to the carbazole moiety, the dibenzothiophene moiety had a negative effect on hole current density and a positive effect on electron transport

Table 4.1.1 Summary of physical properties of carbazole/dibenzothiophene derivatives.

Compounds	T_g[a] (°C)	T_d[b] (°C)	PL λ_{max}[c] (nm)	E_T[d] (eV)	E_g[e] (eV)	HOMO[f] (eV)	LUMO[g] (eV)
*m*BPDBT	87	436	368	2.74	3.44	-6.20	-2.76
*m*CBP	N/A	405	373	2.85	3.41	-6.05	-2.64
*m*DCBP	88	430	370	2.75	3.40	-6.01	-2.61

[a]: Glass transition temperatures; [b]: Decomposition temperatures.

[c]: Measured from vacuum deposited thin film (60 nm).

[d]: Estimated from the first emission peak of phosphorescence spectra (measured in 2-MeTHF matrix at 77 K).

[e]: Optical bandgap energies calculated from the corresponding absorption onset.

[f]: HOMO levels calculated from UPS data.

[g]: LUMO levels calculated from HOMO and E_g of vacuum deposited thin films.

property in these three compounds. Further, in the hole-only device, the current density-voltage characteristic of *m*DCBP showed two distinct regions at low and high bias, a Schottky thermionic region and a space charge limited current region; and the hole-only device with MoO_3 buffer layer forms a quasi-Ohmic contact between organic layer and electrodes, so the hole mobility of *m*DCBP can be estimated by fitting the current density-voltage curve of SCLC region according to the Mott-Gurney equation [87, 88, 160]

$$J = \frac{9}{8}\varepsilon\varepsilon_0\frac{V^2}{d^3}\mu \qquad (4.1.1)$$

where J is the current density; V is the applied voltage; ε is the relative permittivity; ε_0 is the permittivity of the free space; d is the thickness of active layer; and μ is the charge carrier mobility. Under an electric field of 1 MV/cm, the estimated hole mobility of 100 nm *m*DCBP is around 9.2×10^{-4} cm^2/Vs (Figure 4.1.5b).

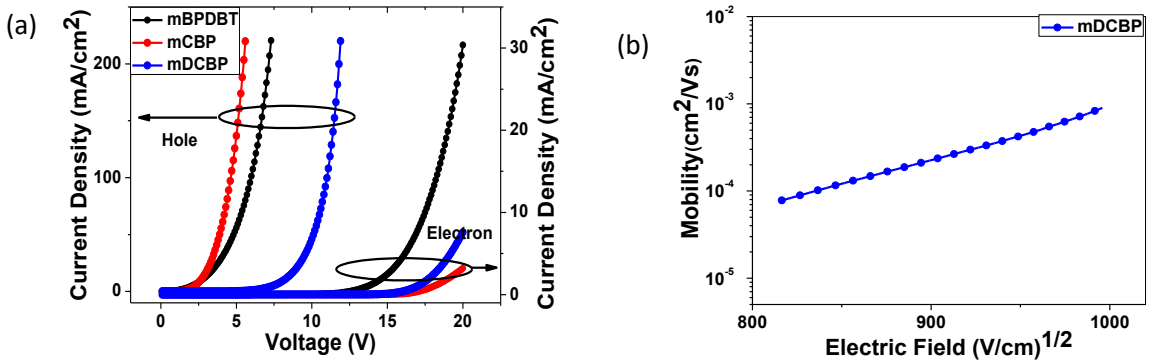

Figure 4.1.5: (a)-(b) current density-voltage curves of single-carrier devices; and (c) mobility-square root of electric field characteristic for *m*DCBP. Notes: The hole-only device structure was ITO/MoO_3/host/MoO_3/Al and the electron-only device structure was ITO/PEIE/BCP/host/BCP/Liq/Al (host = *m*BPDBT, *m*CBP or *m*DCBP).

4.1.4 PhOLEDs characterization

Energy transfer between hosts and emitter

To confirm the capability of *m*DCBP as host material for PhOLEDs, we investigated the photophysical properties of co-deposited thin films of host:FIrpic. The films were 20 nm thick with a FIrpic doping concentration of 8 wt% on quartz substrate. For the PL spectra of doped thin films (see Figure 4.1.6a), all samples showed a main emission peak around 476 nm and a shoulder emission peak around 500 nm, corresponding to the FIrpic emission. Due to the large overlap between PL emission and FIrpic absorption spectra, the emission from *m*DCBP was strongly suppressed, which confirmed the effective positive energy transfer from the host to luminescent FIrpic and then converted into light.

To further understand the relationship between the excited states of the host and guest molecules, transient PL decays of doped thin films were measured at a wavelength of 476 nm at room temperature (4.1.6b). Although *m*DCBP:FIrpic film did not exhibit mono-exponential decay curve, its second exponential decay part was fewer than its first exponential decay part, indicating that the energy transfer from *m*DCBP to FIrpic was energetically favorable due to high triplet energy level, and the energy transfer from FIrpic to hosts was strongly suppressed, thus the energy was well-confined in luminescent FIrpic. All transient PL decay curves were exponentially fitted by decay analysis software (DAS 6, Horiba) with the following functions:

$$I(t) = A_1 e^{-\frac{t}{\tau_1}} + A_2 e^{-\frac{t}{\tau_2}} \quad (4.1.2)$$

where $I(t)$ is the PL intensity, A_1 and A_2 are the quantities of the emission components, and τ_1 and τ_2 are the excited state lifetime of the corresponding emission components, respectively. An excited state lifetime of 1.30 μs for sample *m*BPDBT, 1.28 μs for *m*CBP, and 1.41 μs for *m*DCBP were observed, similar to previous reports on FIrpic [20, 149, 161, 162]. In *m*DCBP, singlet excitons were generated under light excitation and transferred to FIrpic through Förster transfer. In FIrpic, singlet excitons were also generated under light excitation. Thus, the excitons in FIrpic were generated in two ways: energy transfer from the host and direct excitation by light. These singlet excitons on FIrpic can be converted to triplet excitons via intersystem crossing quickly and effectively, then radiatively decay to the ground state ($T_1 \rightarrow S_0$ transition) and are converted into phosphorescence emission.

Experiment

To evaluate the capability of *m*DCBP as host material for blue phosphors and to reveal the influence of carbazole/dibenzothiophene moieties on device performance, a group of FIrpic-based PhOLEDs with a typical sandwich structure were constructed and characterized. The detailed device configuration was ITO/MoO_3 (3.5 nm)/TAPC (40 nm)/host:FIrpic (20 nm)/TmPyPB (40 nm)/Liq (2.5 nm)/Al (host = *m*BPDBT, *m*CBP or *m*DCBP). The blue emitter FIrpic was optimized at optimal doping concentration of 8 wt% according to our group's previous work. MoO_3 and Liq were utilized as hole and electron injection layers, respectively; and TAPC and TmPyPB were served as hole and electron transport layers, respectively. There were large energy barriers for electron leakage from the host to TAPC and hole leakage from the host to TmPyPB, so TAPC and TmPyPB were also used as electron and hole blocking layers, respectively. On the other hand, the triplet energies of TAPC (E_T=2.9 eV) and TmPyPB (E_T=2.8 eV) were higher than that of FIrpic (E_T=2.62 eV), so TAPC and TmPyPB were chosen as the exciton blocker layers to prevent exciton diffusion, thus effectively blocking the excitons within the emissive zone.

Under the electrical excitation, charge recombination in the host materials produce singlet and triplet excitons with a ratio of 1:3, i.e., 25% singlet excitons and 75% triplet excitons. The excitons generated on the host transferred to FIrpic through Förster transfer or Dexter transfer. In FIrpic, singlet and triplet excitons were also generated with a ratio of 1:3 by charge trapping. Thus the excitons in FIrpic were generated in two ways: energy transfer from the host and

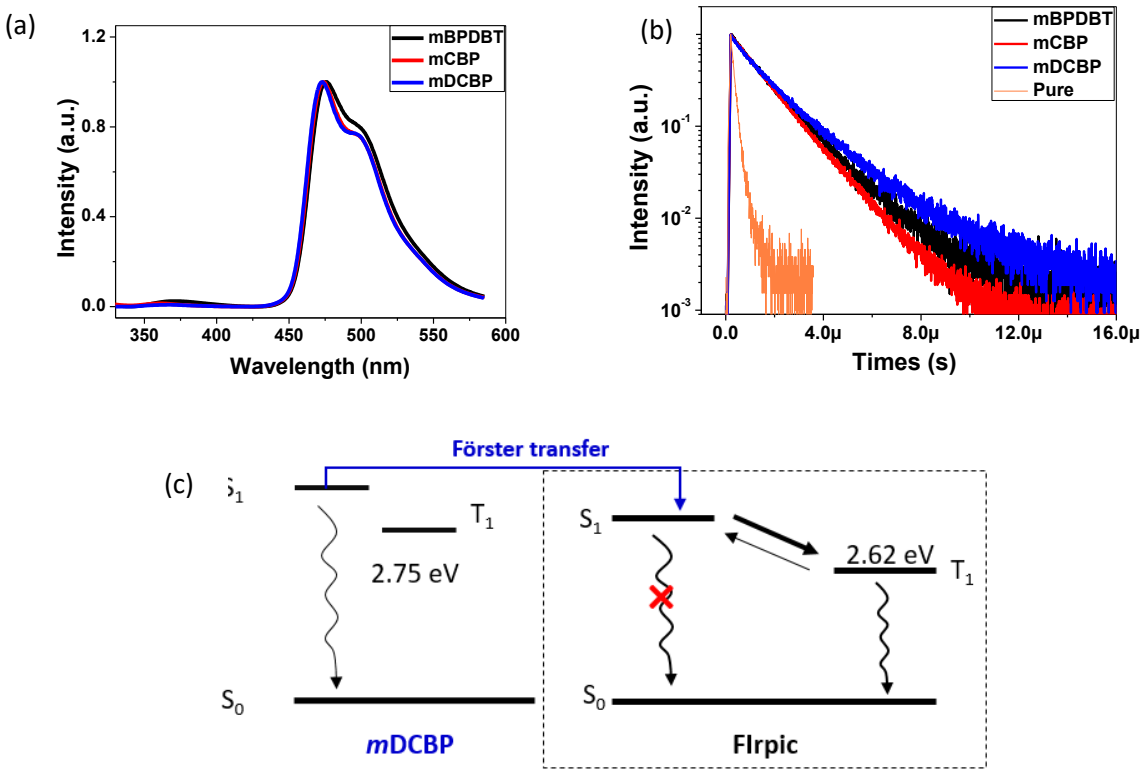

Figure 4.1.6: (a) PL spectra and (b) transient PL decay curves of doped thin films (host:FIrpic, host= *m*BPDBT, *m*CBP or *m*DCBP); (c) schematic illustration of the energy transfer process in *m*DCBP:FIrpic under light excitation.

direct recombination. The singlet excitons on FIrpic can be converted to triplet excitons via intersystem crossing fast and effective, then these triplet excitons radiatively decay from the lowest triplet state to the ground state ($T_1 \rightarrow S_0$ transition) and converted into phosphorescence emission.

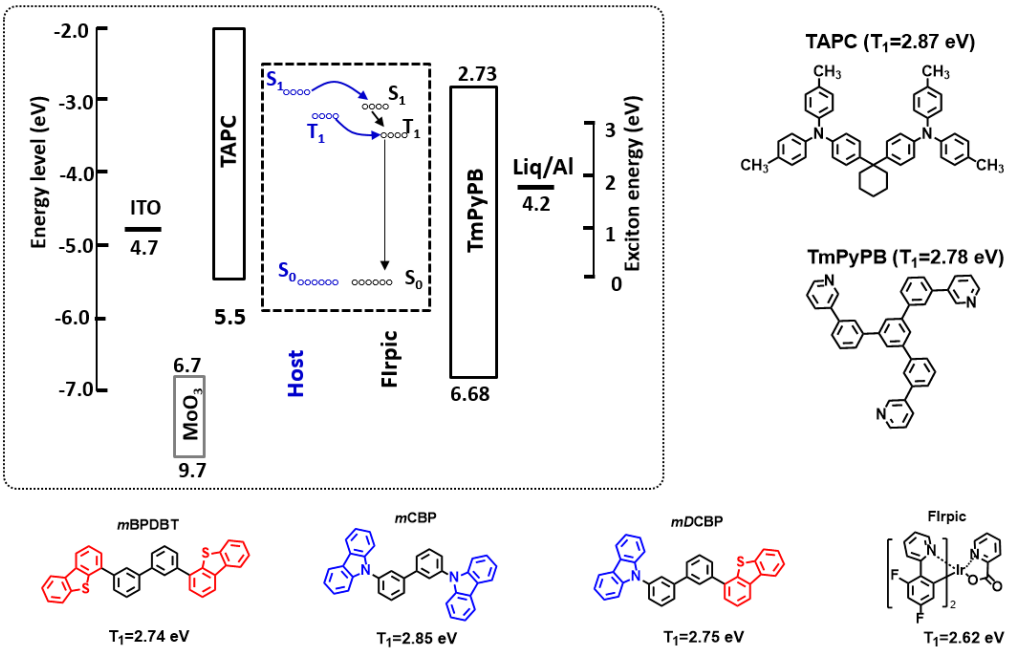

Figure 4.1.7: Energy levels and molecular structures of organic materials in EL devices.

PhOLEDs characterization

Figure 4.1.8a shows the current density-voltage-luminescence curves of the blue PhOLEDs. At the same driving voltage, the current density was highest in *m*CBP-based device and lowest in *m*DCBP-based device. And at same driving voltage, the luminescence was also highest in *m*CBP-based device and lowest in *m*DCBP-based device. At 1000 cd m^{-2} for practical applications, the driving voltage was 5.77 V for *m*DCBP-based device, compared to 5.47 V and 5.17 V for *m*BPDBT-based, and *m*CBP-based devices, respectively.

The current efficiency and power efficiency are shown in Figure 4.1.8b. For *m*CBP-based device and *m*BPDBT-based device, the results were similar to our group's previous study [22]. *m*DCBP-based device showed increased efficiency compared to the other two. For *m*DCBP-based device, the maximum current efficiency was 40.5 cd/A, which was 30% higher than that of *m*CBP-based device; and the maximum power efficiency was 29.4 lm/W.

The *m*DCBP-based device exhibited greatly improved efficiency compared to the other two: the maximum EQE was 17.9% at 0.2 mA/cm^2. Meanwhile, compared to *m*CBP-based and *m*BPDBT-based devices, *m*DCBP-based devices showed lower roll-off ratio at high current density, which was only 12% compared to the maximum value at brightness of 1000 cd m^{-2}. This may be attributed to the more balanced charge carrier in the emission zone.

Compared to *m*CBP-based and *m*BPDBT-based devices, *m*DCBP-based device showed similar EL spectra with a maximum emission peak at 476 nm and a shoulder emission peak at 500 nm, which was arising from the typical emission of phosphor FIrpic. There was no other emission peak from the host or charge transport materials, indicating complete energy transfer from the host to FIrpic and charge confinement inside the emitting layer. As shown in Figure 4.1.8e, the EL spectra of *m*DCBP-based device were not changed according to the driving voltage because the EL emission was only from FIrpic; and the Commission International de I′Eclairage coordinate was (0.16, 0.38). The device performances of PhOLEDs are summarized in Table 4.1.2.

Table 4.1.2 Electroluminescence characteristics of PhOLEDs.

Device	V^a (V)	$\eta_{ce}{}^b$ (cd A^{-1})	$\eta_{pe}{}^b$ (lm W^{-1})	$\eta_{ext}{}^b$ (%)	CIE(x, y)[c]
*m*BPDBT	5.47	23.2/-/19.7	18.1/-/11.3	10.3/-/8.7	(0.17, 0.38)
*m*CBP	5.17	31/30.4/24.8	26.2/24.9/15.1	13.9/13.5/11.0	(0.16, 0.38)
*m*DCBP	5.77	40.5/40.3/35.9	29.4/29.1/19.6	17.9/17.7/15.9	(0.16, 0.38)

[a]: Voltage at 1000 cd m^{-2}.

[b]: Current efficiency, power efficiency, and external quantum efficiency in the order of maximum, 100 cd m^{-2}, and
at 1000 cd m^{-2}, respectively.

[c]: Commission international de I'Eclariage coordinates measured at 5 mA/cm^2.

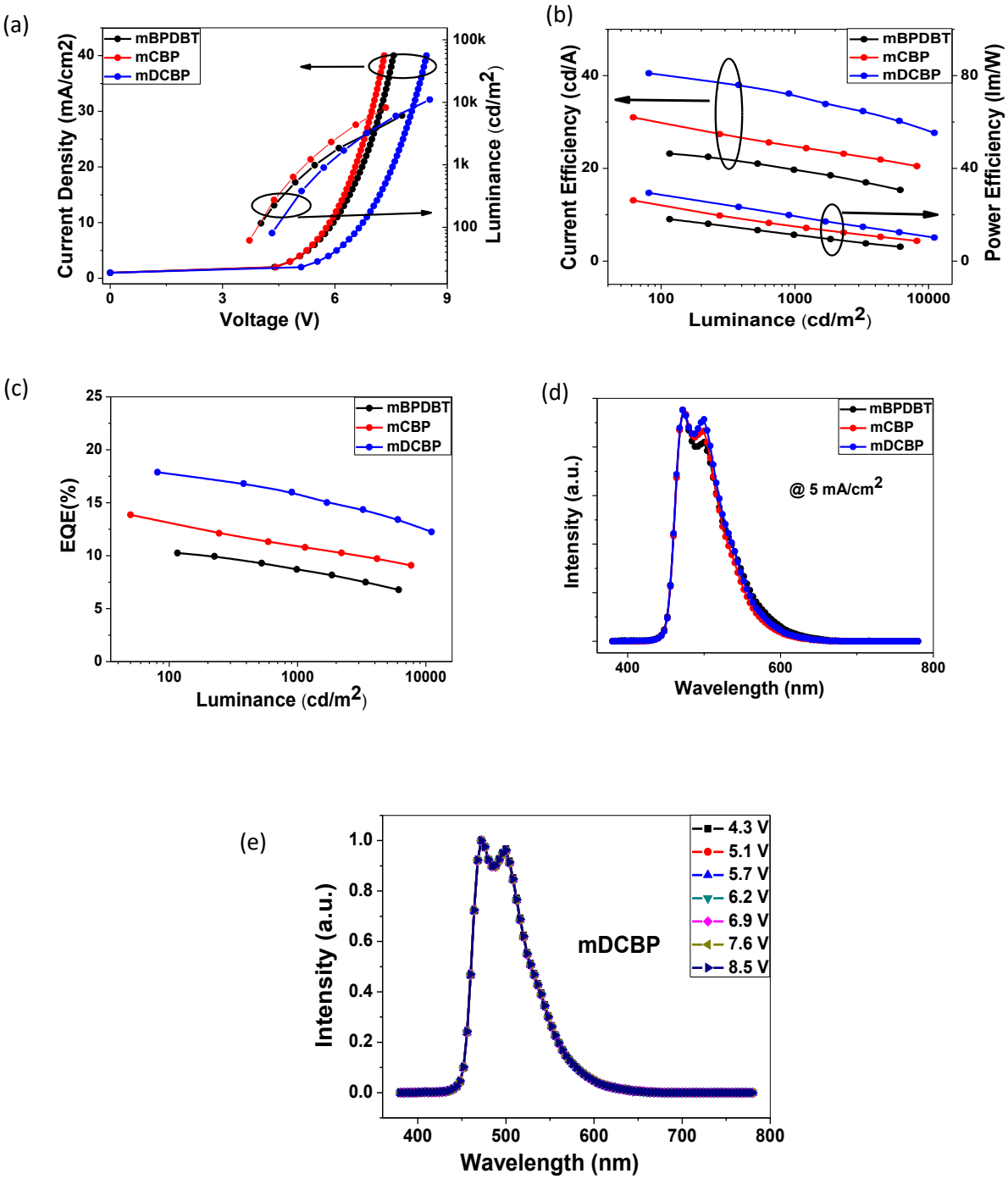

Figure 4.1.8: Device performance: (a) current density-voltage-luminance characteristics; (b) luminance-current efficiency-power efficiency characteristics; (c) luminance-EQE characteristics; (d) EL spectra at 5 mA/cm^2; (e) EL spectra of *m*DCBP-based device at varied driving voltage. Notes: The device structure was ITO/MoO_3/TAPC/host:FIrpic/TmPyPB/Liq/Al (host = *m*BPDBT, *m*CBP or *m*DCBP).

Analysis

From the literature report, TAPC has a high hole mobility of 1.0×10^{-2} cm^2/Vs at 10^5 V/cm and low electron mobility not measurable by time-of-flight (TOF) method [163]. TmPyPB has electron mobility of 7.0×10^{-4} cm^2/Vs at 2.5×10^5 Vcm^{-1} [149]. As the major component of the emitting layer, the host was a decent hole transport material. Thus the holes are considered to be the major charge carriers in PhOLEDs.

To better understand the charge carrier injection/transport behavior in the emission layer, hole- and electron-only devices were fabricated with a doped emitting layer. The hole-only device structure was ITO/MoO_3 (3.5 nm)/TAPC (40 nm)/host:FIrpic (8wt%, 20 nm)/TAPC (10 nm)/Al (120 nm) and the electron-only device structure was ITO/PEIE/BCP (15 nm)/host:FIrpic (8 wt%, 20 nm)/TmPyPB (40 nm)/Liq (2.5 nm)/Al (120 nm) (host = *m*BPDBT, *m*CBP or *m*DCBP). The current density-voltage characteristics are shown in Figure 4.1.9. The single carrier *m*DCBP-based device had slightly lower hole current and higher electron current than that of the single carrier *m*CBP-based device, because the dibenzothiophene moiety had a negative effect on hole transport property and a positive effect on electron transport property compared to the carbazole moiety. The better balanced hole and electron densities in PhOLEDs increased the charge carrier recombination efficiency, thus improving overall device performance. It also guaranteed a wide charge recombination region, which were able to suppress triplet-triplet annihilation or other unwanted quenching, thus reducing the efficiency roll-off at high brightness. For *m*BPDBT, the high HOMO level (6.2 eV) hindered the hole injection from the hole transport layer to the emitting layer due to the high energy barrier, thus greatly reducing the device performance.

4.1.5 TADF OLEDs characterization

Energy transfer between host and emitter

To confirm the capability of *m*DCBP as an effective host material in TADF OLEDs, we investigated the photophysical properties of co-deposited thin films of 4CzIPN doped in hosts. The films were 20 nm in thickness with a doping concentration of 6 wt% on quartz substrate. For the PL spectrum of *m*DCBP:4CzIPN sample (Figure 4.1.10a), it showed a maximum emission peak around 510 nm, corresponding to the $S_1 \rightarrow S_0$ transition in 4CzIPN. The emission from *m*DCBP was completely suppressed, suggesting that the excitons generated on the *m*DCBP were effectively

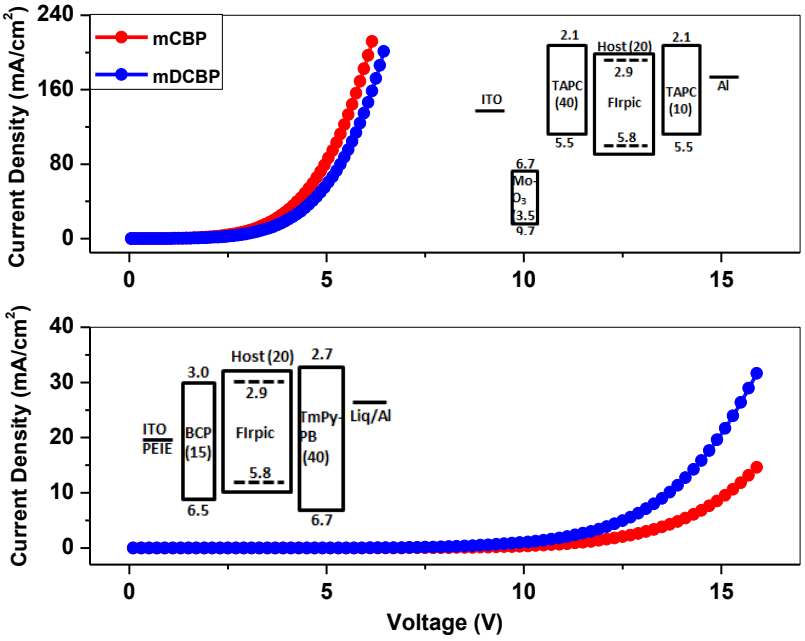

Figure 4.1.9: Current density-voltage characteristics of single-carrier-only devices.

transferred to 4CzIPN and converted into light.

To further understand the relationship between the excited states of the host and guest molecules, transient PL decays of doped thin films were measured at a wavelength of 510 nm at room temperature. As shown in Figure 4.1.10b, the doped thin films clearly exhibited a nano-second-scale component and a micro-second-scale component at room temperature. The first part was assigned to the prompt component derived from the direct $S_1 \rightarrow S_0$ transition of 4CzIPN which had a lifetime (τ_1) of ca. 21 ns, while the second part can be assigned to the delayed TADF component resulting from the $S_1 \rightarrow S_0$ transition of 4CzIPN via successive reverse intersystem crossing of $S_1 \leftarrow T_1$, which exhibited a lifetime (τ_2) that lengthened from 3.23 μs for *m*BPDBT, 3.40 μs for *m*CBP, and 3.29 μs for *m*DCBP. The excited state lifetimes for delayed PL emission were similar to that of preciously reported 4CzIPN [12]. These indicated that *m*DCBP as host could activate the TADF emission of 4CzIPN, and thus could be utilized as host material in TADF OLEDs.

In hosts, the singlet excitons were generated under light excitation and then transferred to 4CzIPN through Förster transfer. In 4CzIPN, the singlet excitons were also generated under light excitation. Thus, the excitons in 4CzIPN were generated in two ways: energy transfer from the host and direct excitation by light. Of these singlet excitons, parts of them radiative

decayed to the ground state ($S_1 \rightarrow S_0$ transition) and the remaining were converted into T_1 excitons via intersystem crossing. The T_1 excitons were then converted into S_1 excitons via reverse intersystem crossing fast and efficient. Finally, the S_1 excitons radiative decayed to the ground state, leading to TADF emission. The S_1-T_1-S_1 cycle may be repeated several times before the radiative decay.

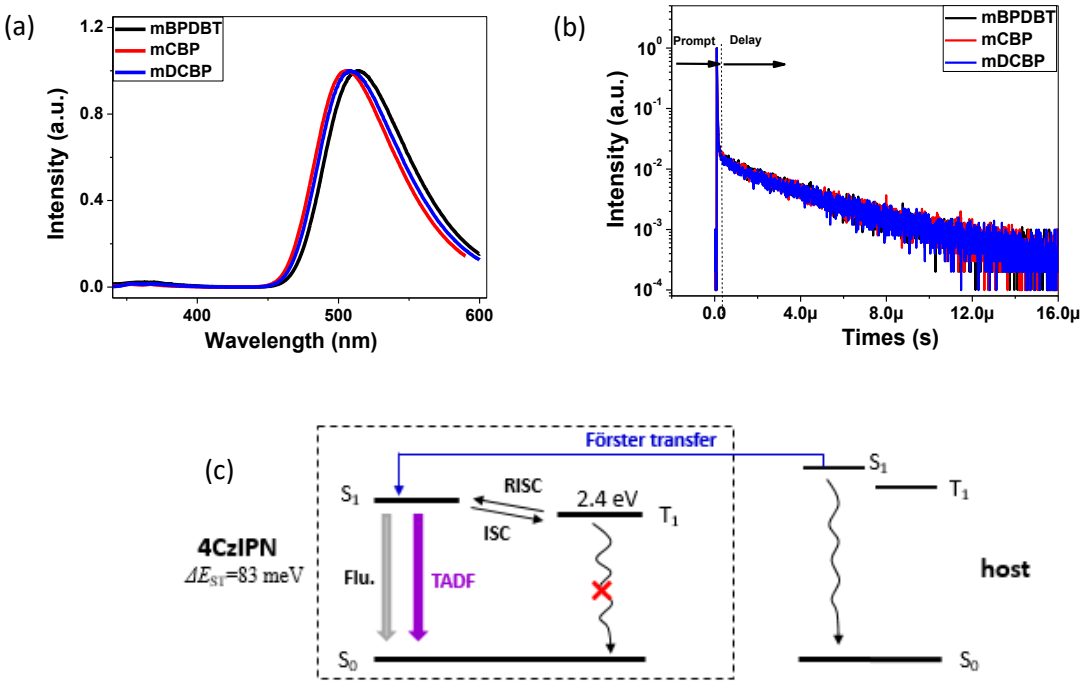

Figure 4.1.10: (a) PL spectra and (b) transient PL decay curves of doped thin films (host:4CzIPN, host= *m*BPDBT, *m*CBP or *m*DCBP); (c) schematic illustration of energy transfer under light excitation.

Experiment

In order to evaluate the capability of *m*DCBP as host material in TADF OLEDs and to reveal the influence of carbazole/dibenzothiophene moieties on device performance, a group of green emitting devices were fabricated. The green devices had the following configuration: ITO/HAT-CN (10 nm)/TAPC (40 nm)/TCTA (10 nm)/host:4CzIPN (20nm, 6 wt%)/TmPyPB (40 nm)/Liq (2.5 nm)/Al (host = *m*BPDBT, *m*CBP or *m*DCBP). The chemical structures and energy levels of the materials used in these devices are presented in Figure 4.1.11. HAT-CN and Liq were utilized as hole and electron injection layers, respectively. TAPC and TCTA were served as hole transport layers. Meanwhile, TCTA also could reduce the hole injection barrier from TAPC to the emitting layer. TmPyPB was served as electron transport layer. The triplet energies of TCTA (E_T=2.7 eV) and TmPyPB (E_T=2.8 eV) are higher than that of 4CzIPN

(E_T=2.42 eV), so TCTA and TmPyPB were selected as the exciton blocker to prevent exciton diffusion.

Under electrical excitation, charge recombination in host materials produced singlet and triplet excitons with a ratio of 1:3, 25% singlet excitons and 75% triplet excitons. The excitons generated in host materials were transferred to 4CzIPN through Förster transfer or Dexter transfer. In 4CzIPN, the singlet and triplet excitons were also generated with a ratio of 1:3 by charge trapping. Thus the excitons in 4CzIPN were generated in two ways: energy transfer from the host and direct recombination. In 4CzIPN, some S_1 excitons decayed radiatively ($S_1 \rightarrow S_0$ transition) and the remaining excitons were converted into T_1 excitons via intersystem crossing. And all the T_1 excitons can converted into S_1 excitons via reverse intersystem crossing ($S_1 \leftarrow T_1$). Finally, the S_1 excitons radiatively decayed to the ground state, leading to the TADF emission. The S_1-T_1-S_1 cycle may be repeated several times before the radiatively decay.

TADF OLEDs characterization

Figure 4.1.12a shows the current density-voltage-luminescence curves of the TADF OLEDs. The current density and luminance were highest in *m*DCBP-based device at the same driving voltage compared to the other two devices. At 1000 cd m^{-2} for practical applications, the driving voltage was 4.39 V for *m*DCBP-based device, much lower than that of *m*BPDBT-based and *m*CBP-based devices, which were 5.48 V. and 5.13 V, respectively.

More importantly, the *m*DCBP-based device showed increased current and power efficiency compared to the other two devices. Its maximum current efficiency was 66.0 cd/A, which was around 14% higher than that of *m*CBP-based device; its maximum power efficiency was 51.8 lm/W, which was 16% higher than that of *m*CBP. The *m*DCBP-based device also exhibited substantial improvement in external quantum efficiency: its maximum external quantum efficiency was 19.4%, compared with 16.7% and 17.6% for *m*BPDBT-based and *m*CBP-based devices, respectively.

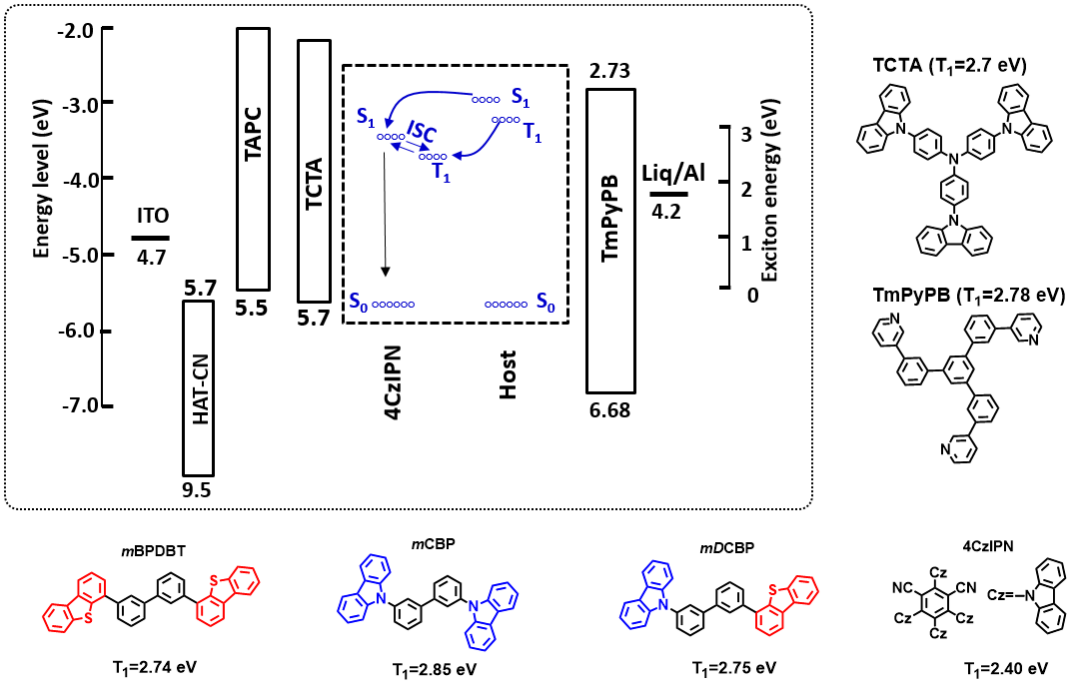

Figure 4.1.11: Energy levels and molecular structures of organic materials adopted in EL devices.

The *m*DCBP-based device showed EL spectrum with a maximum emission peak around 520 nm, which was arising from the typical emission of 4CzIPN. There was no other radiative emission peak from the host or charge transport materials, indicating complete energy transfer from the host to FIrpic, and excitons were well-confined within the emitting layer. The EL spectra of these devices remained consistent according to the driving voltage of the device because the EL emission was only from the 4CzIPN, and the commission International de I′Eclairage coordinate was (0.31, 0.59). Compared to the *m*BPDBT-based device, there was a small blue shift in the EL wavelength (8 nm) in the *m*DCBP-based device. The device performances of TADF OLEDs are summarized in Table 4.1.3.

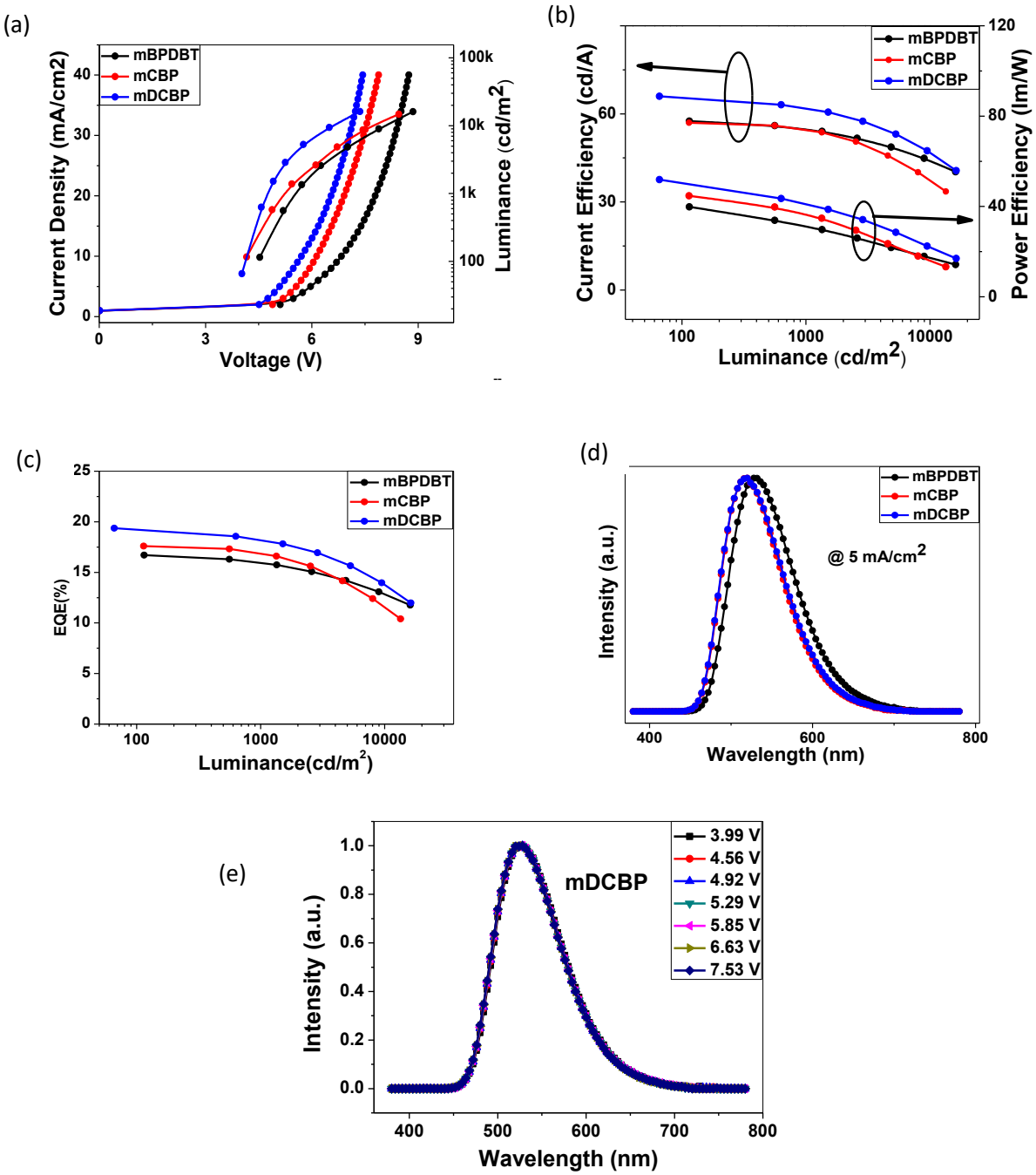

Figure 4.1.12: Device performance: (a) current density-voltage-luminance characteristics; (b) luminance-current efficiency-power efficiency characteristics; (c) luminance-EQE characteristics; (d) EL spectra at 5 mA/cm^2; and (e) EL spectra of *m*DCBP-based device at varied applied voltage. Notes: The device structure was ITO/HAT-CN/TAPC/TCTA/host:4CzIPN/TmPyPB/Liq/Al (host = *m*BPDBT, *m*CBP or *m*DCBP).

Table 4.1.3 Electroluminescence characteristics of TADF OLEDs.

Device	V^a (V)	$\eta_{ce}{}^b$ (cd A^{-1})	$\eta_{pe}{}^b$ (lm W^{-1})	$\eta_{ext}{}^b$ (%)	CIE(x, y)[c]
*m*BPDBT	5.48	57.5/-/54.9	39.8/-/31.5	16.7/-/16.0	(0.33, 0.59)
*m*CBP	5.16	58.0/-/54.7	44.7/-/37.0	17.6/-/16.9	(0.28, 0.57)
*m*DCBP	4.71	66.0/65.8/62.0	51.8/51.4/41.5	19.4/19.3/18.2	(0.31, 0.59)

[a]: Voltage at 1000 cd m^{-2}.

[b]: Current efficiency, power efficiency, and external quantum efficiency in the order of maximum, 100 cd m^{-2}, and
at 1000 cd m^{-2}, respectively.

[c]: Commission international de I'Eclariage coordinates measured at 5 mA/cm^2.

Analysis

Actually, in multilayer devices, charge carrier injection and transport are not only dependent on the intrinsic electrical performance of each involved materials, but also dramatically determined by their compatibility. To better understand the charge injection/transport behavior in the host:4CzIPN layer, the hole- and electron-only devices with doped emitting layer were fabricated. The hole-only device structure was ITO/HAT-CN (10 nm)/TAPC (40 nm)/host:4CzIPN (6% wt, 20 nm)/TAPC (10nm)/Al (120 nm) and the electron-only device structure was ITO/PEIE/BCP (15 nm)/host:4CzIPN (6%, 20nm)/TmPyPB (40 nm)/Liq (2.5 nm)/Al (120 nm) (host = *m*BPDBT, *m*CBP or *m*DCBP). In hole-only devices, due to the high electron injection barrier (>2 eV) at the Al/TAPC interface, the electrons injected from the cathode should be the exclusive charge carriers in the device. Similarly, the holes injected from the anode to the device should be the exclusive charges in the device due to the high injection barrier (>2 eV) at the PEIE/BCP interface [144]. Clearly, at the same electrical field, the electron current density is much lower than the hole current density in single-carrier devices. Further, consider the charge mobility of each material, TCTA has the hole mobility of 3×10^{-4} cm^2 $V^{-1}s^{-1}$ at an applied field of 0.5 MV/cm [164]. Thus, holes are considered to be the major carrier in TADF OLEDs and the emitting area is close to the EML/ETL interface. The single-carrier *m*DCBP-based device had both the highest hole and highest electron injection and transporting ability in these three devices. Therefore, it's expected that the enhanced both hole and electron density in the emitting layer in TADF OLEDs improved the device performance.

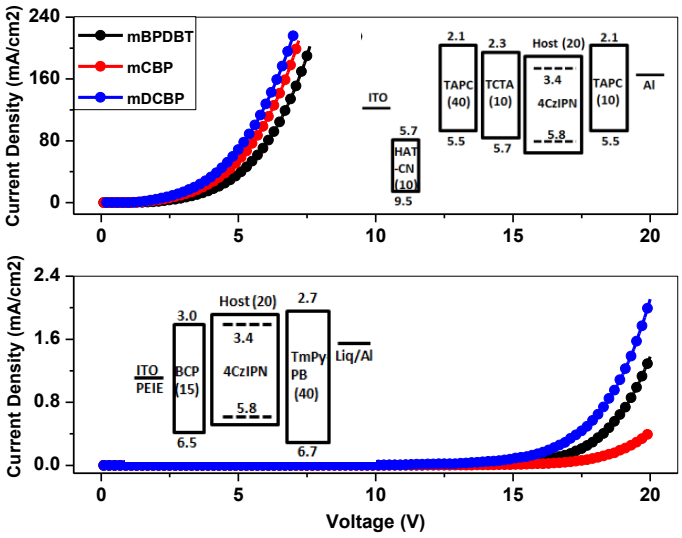

Figure 4.1.13: Current density-voltage characteristics of single-carrier-only devices.

4.1.6 Summary

A high-performance host material, *m*DCBP, combining a p-type carbazole moiety and n-type dibenzothiophene moiety was investigated. Its thermal, photophysical and electrical properties were detailed investigated and the device performance of blue PhOLEDs and green TADF OLEDs based on it were detailed investigated. The *meta*-bonding design endows the materials with high triplet energy (2. 75 eV), rendering it a potential host candidate for sky blue and green OLEDs. High morphological stability and film-forming ability, sufficiently high triplet energy, suitably aligned HOMO and LUMO levels with the adjacent layer, larger HOMO-LUMO energy gaps than the emitters, efficient energy transfers from host to guest, and good charge balance in the emitting layer leaded to a high performance OLEDs by employing *m*DCBP as host. The blue PhOLEDs produced a maximum current efficiency of 40.5 cd/A, power efficiency of 29.4 lm/W, and external quantum efficiency of 17.9%; the TADF OLEDs showed a maximum current efficiency of 66 cd/A, power efficiency of 51.8 lm/W, and external quantum efficiency of 19.4%. The OLEDs also showed a low efficiency roll-off at high brightness. It is worth noting that we did not use any light outcoupling enhancement techniques when fabricating OLEDs, so there is some room to achieve higher efficiency. This work gains insight into the molecular structure-property relationship of carbazole/dibenzothiophene moieties, and reveals that the carbazole and dibenzothiophene moieties could act as important building blocks in designing new host materials for high-efficiency OLEDs.

4.2 Carbazole/dibenzothiophene derivatives with extended phenyl spacer as host materials in modern OLEDs

4.2.1 Introduction

In the previous study of *m*DCBP, the carbazole and dibenzothiophene moieties were connected by biphenyl through *meta*-linkage and had achieved excellent EL performance. This motivated us to conduct the subsequent research on the structural modification of *m*DCBP to develop high-performance hosts. In general, the π-conjugation length should be minimized to obtain high triplet energies for host materials; for example, functional groups are connected through *meta*-linkage to keep high triplet energy while enlarging the π conjugation length of the host material [22, 165]. And in *m*DCBP, by linking the carbazole and dibenzothiophene moieties with the biphenyl group, it showed excellent performance. That revealed the phenyl unit is a good linking spacer. In this study, two carbazole/dibenzothiophene derivatives, with different linking spacers, one phenyl or three phenyl rings between carbazole and dibenzothiophene moieties, were synthesized and characterized. Their physical, photophysical, and electrical properties were systematically investigated and the device performance of blue PhOLEDs and green TADF OLEDs based on them were explored extensively. We focused especially on the manner in how the linking spacer between carbazole and dibenzothiophene units affect the optical and electrical properties of the resulting devices

4.2.2 Molecular synthesis

The host materials *m*DCP and *m*DCTP were synthesized by a project partner (Dr. Shoucheng Dong) at Soochow University. Scheme 4.2.1 illustrates the synthesis route of the host material; synthesis was straightforward with classic Suzuku-Miyaura reaction.

*m*DCP: Dibenzothiophene-4-boronic acid (1.50g, 6.58 mmol), 9-(3-bromophenyl)-9H-carbazole (1.30g, 4.04 mmmol), and tetrakis (triphenylphosphine) palladium (0) (5% molar ratio) were dissolved in THF/2 M K_2CO_3 (45 ml, 3/1, v/v) in a Schlenk tube under argon. The resulting mixture was refluxed for 12 h. After cooling to the room temperature, the organic layer was collected and annealed to remove the residual solvent. The crude product was purified by column chromatography on silica gel using dichloromethane/petroleum (1/5, v/v) as eluent, followed by recrystallization from ethyl acetate/petroleum and vacuum sublimation successively. The final product was a white powder (1.25 g, 72.9%). ^{1}H NMR (400 MHz, CDCl3) δ (ppm): 8.14-8.20 (m, 4H), 7.97 (b, 1H), 7.82-7.87 (m, 2H), 7.75 (t, J = 8.0 Hz, 1H), 7.66 (d, J = 8.0 Hz, 1H), 7.53-7.61 (m, 4H), 7.43-7.50 (m, 4H), 7.32 (t, J = 8.0 Hz, 2H). ^{13}C

NMR (100 MHz, CDCl3) δ (ppm): 142.7, 141.0, 139.6, 138.6, 138.4, 136.6, 136.1, 135.9, 130.5, 127.5, 127.2, 127.0, 126.7, 126.2, 125.4, 124.7, 123.7, 122.9, 122.0, 121.1, 120.6, 120.3, 110.1. MS (EI): m/z 425.1 (M+). Anal. calcd for $C_{30}H_{19}NS$ (%): C 84.67, H 4.50. N 3.29; found: C 84.34, H 4.42, N 3.28.

*m*DCTP: 9-(3'-bromo-[1,1'-biphenyl]-3-yl)-9H-carbazole (1.20 g, 3.01 mmol), 2-(3-(dibenzothiophen-4-yl) phenyl)-4,4,5,5-tetramethyl-1,3,2-dioxaborolane (1.39 g, 3.60 mmol) were dissolved in THF/2 M K_2CO_3 (45 ml, 3/1, v/v) in a Schlenk tube under argon. The resulting mixture was refluxed for 12 h. After cooling to the room temperature, the organic layer was collected and annealed to remove the residual solvent. The crude product was purified by column chromatography on silica gel using dichloromethane/petroleum (1/5, v/v) as eluent, followed by recrystallization from ethyl acetate/petroleum and vacuum sublimation successively. The final product was a white powder (1.05 g, 60.3%). ^{1}H NMR (400 MHz, CDCl3) δ (ppm): 8.14-8.20 (m, 4H), 8.04 (s, 1H), 7.95 (s, 1H), 7.88 (s, 1H), 7.53-7.79 (m, 12H), 7.35-7.51 (m, 6H), 7.29 (t, J = 6.8 Hz, 2H). ^{13}C NMR (100 MHz, CDCl3) δ (ppm):143.2, 142.0, 141.7, 141.4, 141.1, 141.0, 139.7, 138.8, 138.5, 137.0, 136.5, 136.0, 130.5, 129.7, 129.6, 127.6, 127.4, 127.1, 127.0, 126.5, 126.2, 126.0, 125.4, 124.6, 123.6, 122.8, 122.0, 120.8, 120.5, 120.2, 110.0. MS (EI): m/z 577.2 (M+). Anal. calcd for $C_{42}H_{27}NS$ (%): C 87.31, H 4.71, N 2.42; found: C 87.02, H 4.53, N 2.40.

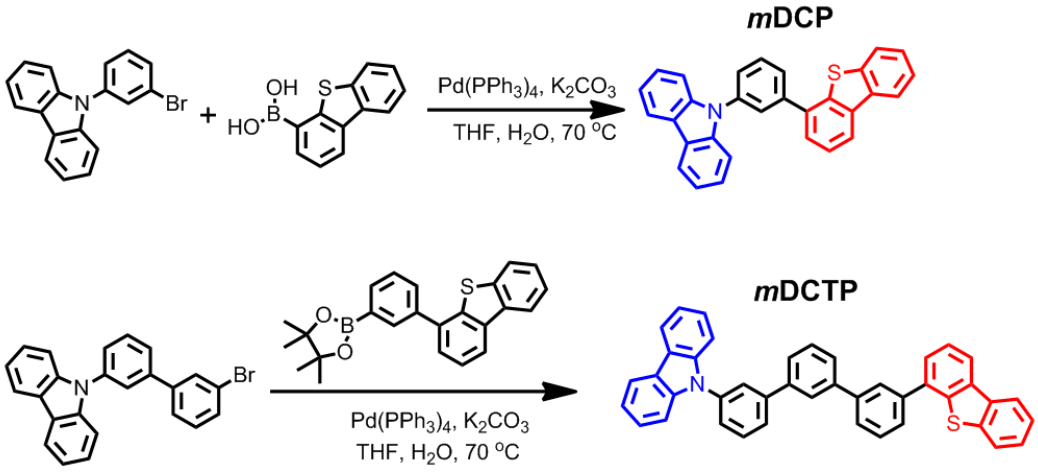

Scheme 4.2.1: Synthesis of carbazole/dibenzothiophene derivatives.

4.2.3 Fundamental physical properties

Quantum chemical calculations

To understand the molecular structure-property relationship of *m*DCP and *m*DCTP at the molecular level, their HOMO and LUMO orbital spatial distributions were obtained by the density function theory calculations at the (B3LYP)/6-31G (d) level with Gaussian program [154]. Figure 4.2.1 shows the HOMO and LUMO distributions of *m*DCP, *m*DCBP, and *m*DCTP. These three compounds showed rather similar HOMO and LUMO distributions. The HOMO orbitals were mainly located on the strong electron donating carbazole moiety and the adjacent phenyl ring due to the strong electron-donating nitrogen unit of carbazole, whereas the LUMO orbitals were distributed on the dibenzothiophene moiety and spread over all the phenyl spacer (phenyl-dibenzothiophene unit) due to the electron-withdrawing sulfur group. This indicated that carbazole is a hole transport moiety and dibenzothiophene is an electron transport moiety in these three compounds. Therefore, *m*DCP and *m*DCTP would exhibit electron-accepting properties as well as hole-accepting properties from the charge transport materials.

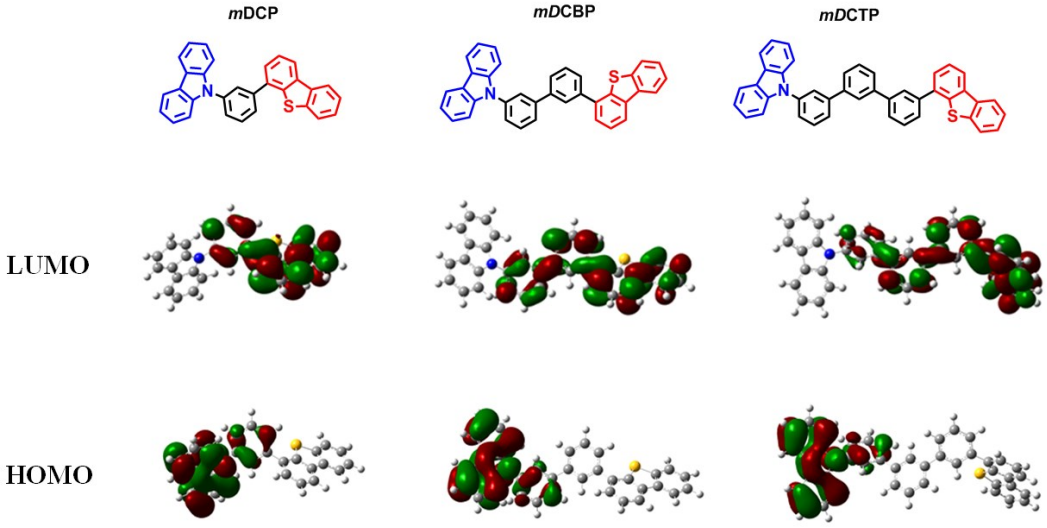

Figure 4.2.1: HOMO and LUMO spatial distributions of carbazole/dibenzothiophene derivatives.

Thermal analysis

The thermal stabilities of the materials were characterized by TGA and DSC, as mentioned above, thermal stability is closely related to the device stability. Figure 4.2.2 shows the DSC and TGA thermograms of *m*DCP, *m*DCBP, and *m*DCTP. These compounds showed clearly glass-transition temperatures. With the extended phenyl spacer, the glass transition

temperatures increased from 68˚C of *m*DCP, through 88˚C of *m*DCBP, to 98˚C of *m*DCTP; their decomposition temperatures increased from 382˚C of *m*DCP, through 430˚C of *m*DCBP, to 462˚C of *m*DCTP. As phenyl spacers extended, the molecular size and molecular weight increased, so thermal stabilities increased.

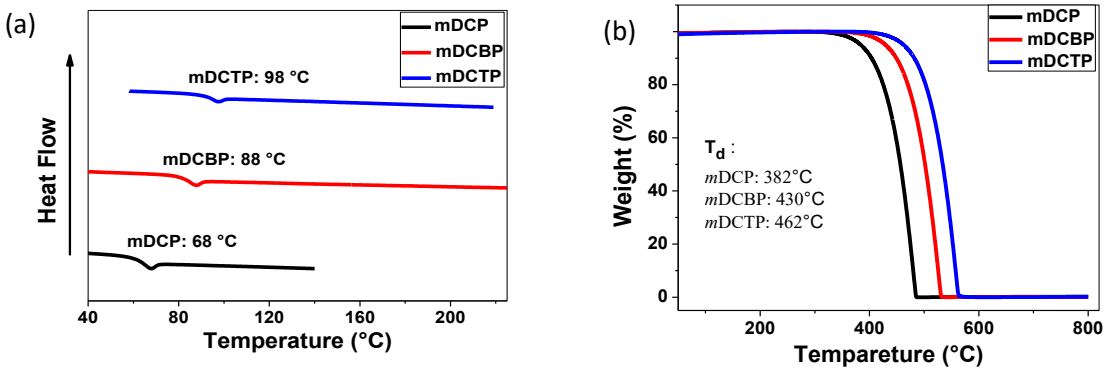

Figure 4.2.2: (a) DSC traces and (b) TGA traces recorded at a heating rate of 10˚C min^{-1}.

Photophysical properties

The photophysical properties of *m*DCP, *m*DCBP, and *m*DCTP were investigated via UV-Vis absorption, PL, and phosphorescence spectra, as shown in Figure 4.2.3. The UV-Vis absorption and PL spectra were obtained from vacuum evaporated thin films (60 nm) and phosphorescence spectra were measured in 2Me-THF at 77 K. These three compounds showed almost identical UV-Vis absorption and PL spectra. The relatively weak shoulder peak at ca. 355 nm can be attributed to the n-π* transitions of the carbazole group [30, 156]. The optical-energy bandgaps were determined by the onset of UV-Vis absorption spectra. The absorption edges of the spectra for *m*DCP, *m*DCBP, and *m*DCTP were 364 nm, 365 nm, and 364 nm, respectively, corresponding to bandgaps of 3.41 eV, 3.40 eV, and 3.41 eV, respectively. These three compounds also had similar violet fluorescence emission. The maximum PL emission peaks of *m*DCP, *m*DCBP, and *m*DCTP were observed at 373 nm, 370 nm, and 369 nm, respectively, corresponding to the singlet energy of 3.32 eV, 3.35 eV, and 3,36 eV. A narrow FWHM ranging from 44 nm of *m*DCP through 47 nm of *m*DCBP to 45 nm of *m*DCTP were observed. The emission spectra of these three compounds were well overlapped with the absorption spectra of typical high-efficiency blue and green emitters, suggesting that energy transfer from the host to the dopant would be efficient in practice [157-159]. All the materials exhibit broad phosphorescent spectra. The triplet energies were calculated by the first emission peak of phosphorescent spectra ($T_1^{v=0} \rightarrow S_0^{v=0}$). The triplet energy of *m*DCTP was 2.79 eV,

similar with that of *m*DCBP and *m*DCP (2.75 eV), both sufficient for used as host for blue and green triplet emitters. These indicating that with a merit of *meta*-linkage, the extended phenyl spacers had negligible effect on materials' photophysical properties.

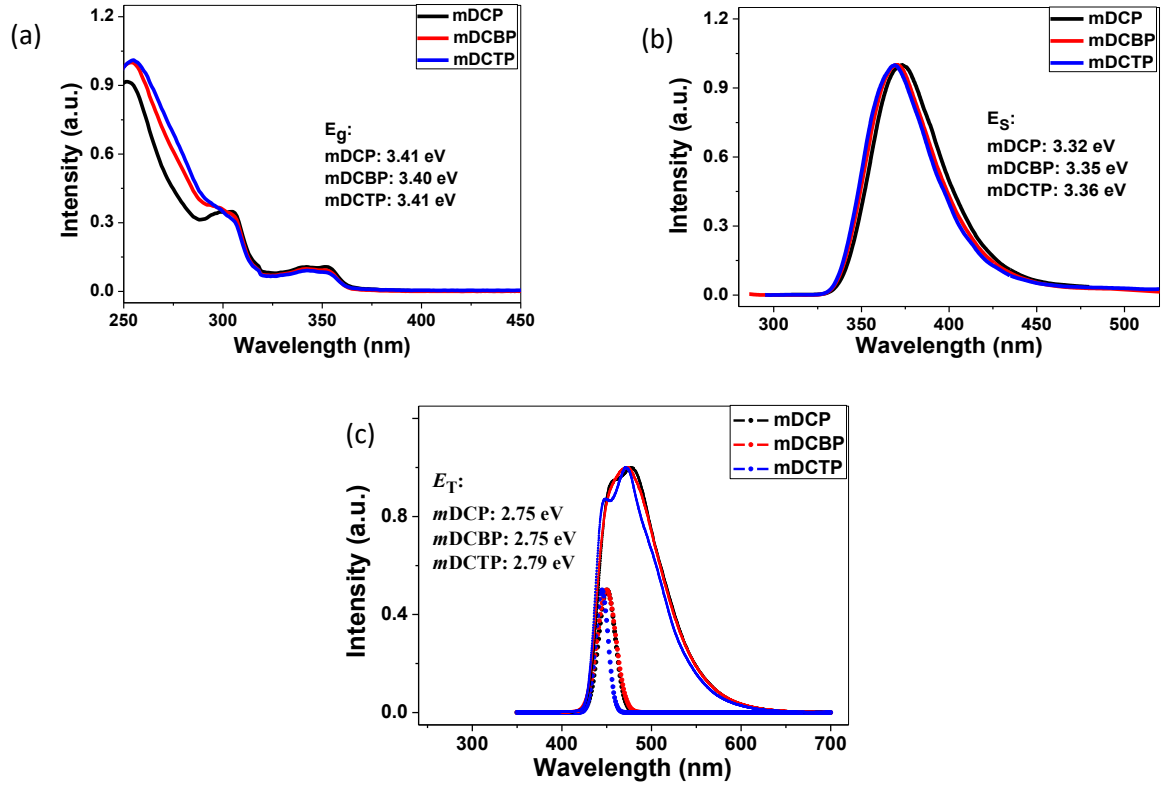

Figure 4.2.3: (a) UV-Vis absorption and (b) PL spectra of vacuum deposited thin films; (c) phosphorescence spectra in frozen 2-MeTHF matrix at 77 K.

HOMO/LUMO levels

For host materials, appropriate HOMO and LUMO levels are essential to the efficient injection of carriers into the emitting layer. The HOMO levels of the materials were determined by UPS. The HOMO levels of *m*DCP, *m*DCBP, and *m*DCTP were -5.94 eV, -6.01eV and -5.98 eV, respectively. The optical LUMO levels were calculated using HOMO and optical band gap in solid films, according to the equation $E_{LUMO} = E_{HOMO}+E_g$, so the LUMO levels of *m*DCP, *m*DCBP and *m*DCTP were -2.53 eV, -2.61 eV, and -2.57 eV, respectively. Table 4.2.1 summarizes all of the physical data of these materials.

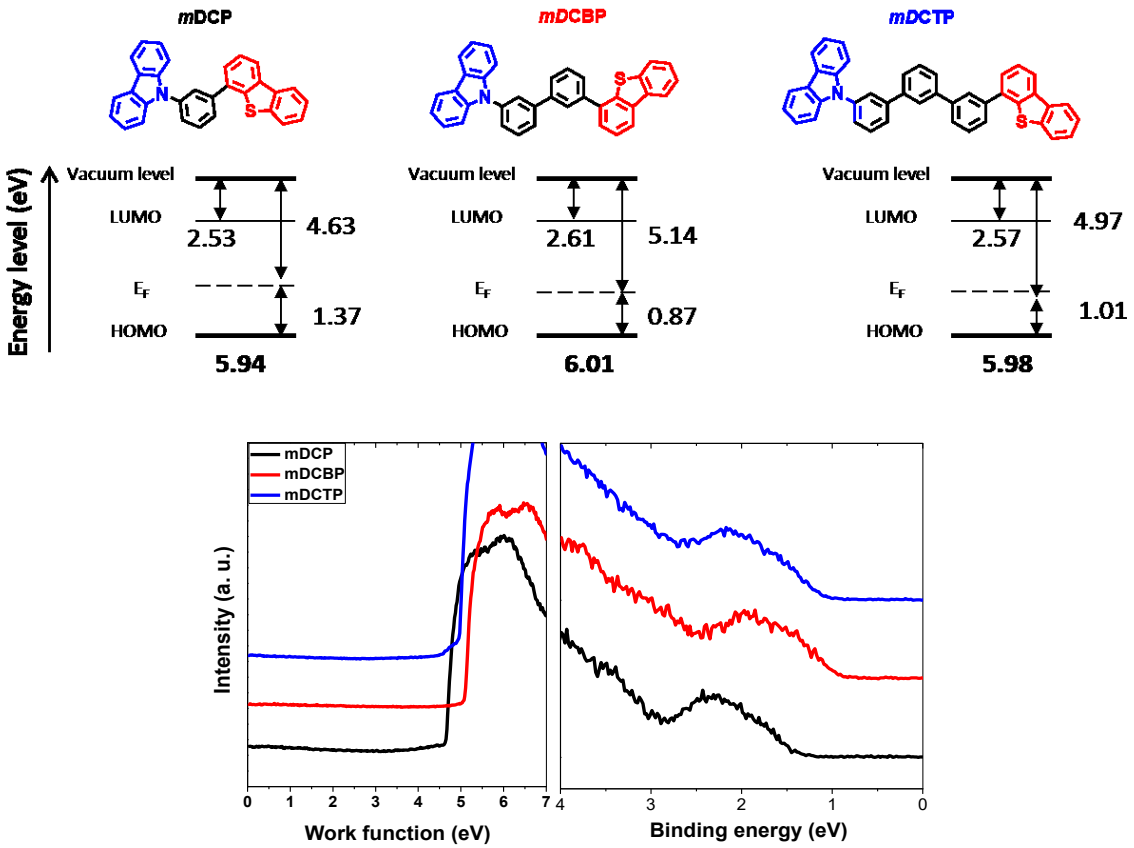

Figure 4.2.4: UPS spectra of carbazole/dibenzothiophene derivatives.

Carrier-transport properties

To evaluate their charge carrier transport ability, single-carrier devices were fabricated. The hole-only device had the structure: ITO/MoO_3 (10 nm)/host (100 nm)/MoO_3 (10 nm)/Al and the electron-only device had the structure: ITO/PEIE/BCP (15 nm)/host (100 nm)/BCP (15 nm)/Liq (2.5 nm)/Al (host= *m*DCP, *m*DCBP or *m*DCTP). As shown in Figure 4.2.5, in all three single-carrier devices, at the same electrical field intensity, the electron current densities were much lower than the hole current densities. Both hole and electron current densities decreased as phenyl spacers increased. In the hole-only devices, the current density-voltage characteristics of the samples showed two distinct regions at low and high bias: a Schottky thermionic region and a SCLC region, respectively. The hole mobility of *m*DCP and *m*DCTP can be estimated by fitting the current density-voltage curves of SCLC region according to the Mott-Gurney equation [87, 88]

$$J = \frac{9}{8}\varepsilon\varepsilon_0\frac{V^2}{d^3}\mu \tag{4.2.1}$$

where J is the current density; V is the applied voltage; ε is the relative permittivity; ε_0 is the permittivity of the free space; d is the thickness of active layer; and μ is the charge carrier

mobility. Under an electric field of 0.6 MV/cm, the estimated hole mobility of 100 nm *m*DCP is 1.4×10^{-3} cm^2/Vs. And under an electric field of 1 MV/cm, the estimated hole mobility of 100 nm *m*DCTP is 1.7×10^{-4} cm^2/Vs.

Table 4.2.1 Summary of physical properties of carbazole/dibenzothiophene derivatives.

Compounds	T_g[a] (°C)	T_d[b] (°C)	PL λ_{max}[c] (nm)	E_T[d] (eV)	E_g[e] (eV)	HOMO[f] (eV)	LUMO[g] (eV)
*m*DCP	68	382	373	2.79	3.41	-6.00	-2.59
*m*DCBP	88	430	370	2.75	3.40	-6.01	-2.61
*m*DCTP	98	462	369	2.75	3.41	-5.98	-2.58

[a]: Glass transition temperatures; [b]: Decomposition temperatures.

[c]: Measured from vacuum deposited thin film (60 nm).

[d]: Estimated from the first emission peak of phosphorescence spectra (measured in 2-MeTHF matrix at 77 K).

[e]: Optical bandgap energies calculated from the corresponding absorption spectra onset.

[f]: HOMO levels calculated from UPS data.

[g]: LUMO levels calculated from HOMO and E_g of vacuum deposited thin films.

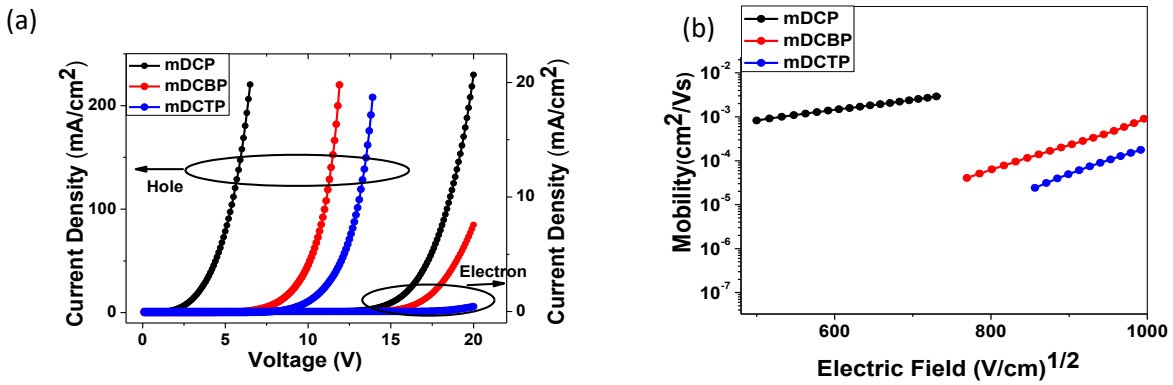

Figure 4.2.5: (a) Current density-voltage curves of single-carrier devices and (b) mobility-square root of electric field. Note: The hole-only device structure was ITO/MoO_3/host/MoO_3/Al and the electron-only device was ITO/PEIE/BCP/host/BCP/Liq/Al (host= *m*DCP, *m*DCBP or *m*DCTP).

4.2.4 PhOLEDs characterization

Energy transfer between hosts and emitter

To confirm the applicability of *m*DCP and *m*DCTP as the hosts for PhOLEDs, we investigated the photophysical properties of co-deposited thin films of host:FIrpic (host= *m*DCP, *m*DCBP or *m*DCTP). The films were 20 nm thick with a FIrpic doping concentration of 8 wt% on quartz substrate. For the PL spectra of doped thin film (Figure 4.2.6a), all samples showed an emission peak around 476 nm and a shoulder emission peak around 500 nm, corresponding to the FIrpic emission. The emission from the *m*DCP or *m*DCTP was strongly suppressed, which confirmed the effective energy transfer from the high singlet energy host to luminescent FIrpic and then converted into light.

To further understand the relationship between the excited states of the hosts and guest molecules, transient PL decays of doped thin films were measured at a wavelength of 476 nm at room temperature. According to Figure 4.2.6b, although these films did not exhibit mono-exponential decay curves, their second exponential decay parts were fewer than their first exponential decay parts, indicating that due to high E_T, the energy transfer from the hosts to FIrpic was energetically favorable and the energy transfer from FIrpic to hosts was suppressed, thus the energy was well-confined in luminescent FIrpic. All the transient PL decay curves were exponentially fitted by decay analysis software (DAS 6, Horiba). The excited state lifetimes of 1.64 μs for sample *m*DCP, 1.41 μs for *m*DCBP, and 1.36 μs for *m*DCTP were obtained, similar to previously reported FIrpic [149, 161, 162].

In the hosts, singlet excitons were generated under the light excitation, then transferred to FIrpic through Förster transfer. In FIrpic, singlet excitons were also generated under light excitation. Thus the excitons in FIrpic were generated in two ways: energy transfer from the hosts and direct excitation by light. These singlet excitons in FIrpic can be converted to triplet excitons via intersystem crossing, then the triplet excitons radiatively decay from T_1 to the ground state ($T_1 \rightarrow S_0$ transition) and are converted into phosphorescence emission.

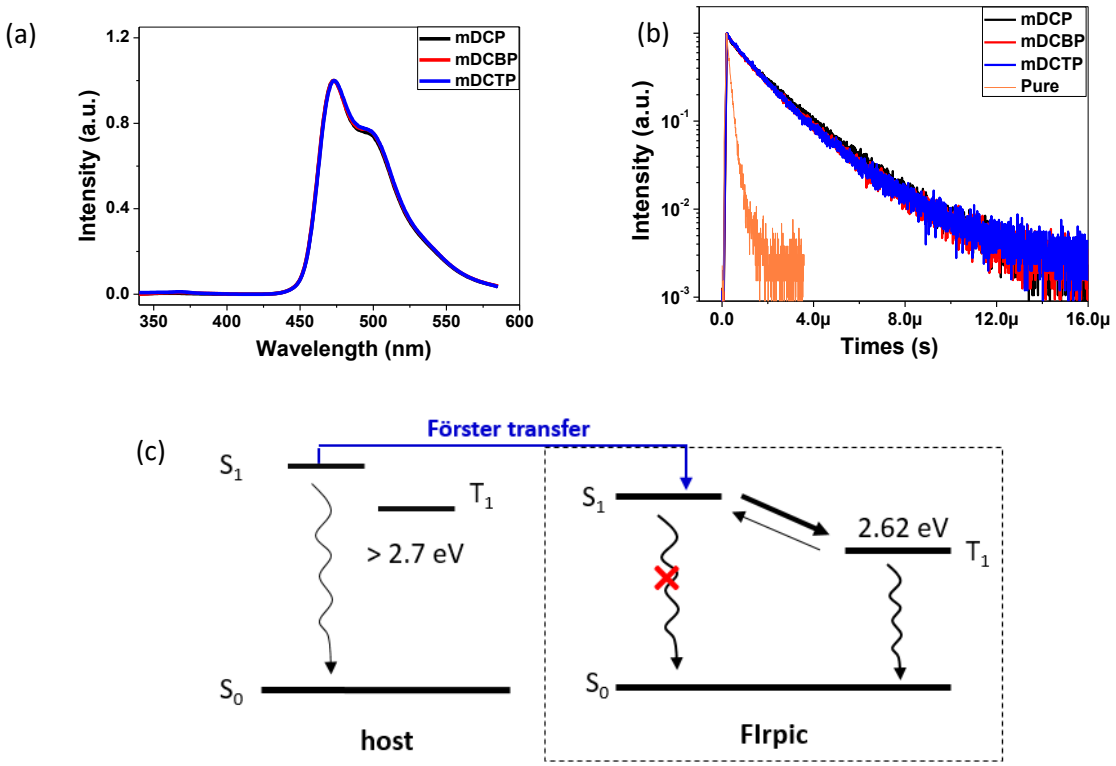

Figure 4.2.6: (a) PL spectra and (b) transient PL decay curves of doped thin films (host:FIrpic, host= *m*BPDBT, *m*CBP or *m*DCBP); (c) schematic illustration of energy transfer process under light excitation.

Experimental

To evaluate the performance of *m*DCP and *m*DCTP as host for blue phosphors and reveal the influence of extend phenyl spacers on PhOLEDs performance, FIrpic-based PhOLEDs were constructed with a typical sandwich structure. The detailed device configuration was ITO/MoO_3 (3.5 nm)/TAPC (40 nm)/host:FIrpic (20 nm, 8wt%)/TmPyPB (40 nm)/Liq (2.5 nm)/Al (host= *m*DCP, *m*DCBP or *m*DCTP). MoO_3 and Liq were utilized as hole and electron injection layers, respectively. TAPC and TmPyPB were served as hole and electron transport layer, respectively. There were large energy barriers for electron leakage from the host to TAPC and hole leakage from the host to TmPyPB, so TAPC and TmPyPB were used as electron and hole blocking layers. On the other hand, the triplet energies of TAPC (E_T=2.9 eV) and TmPyPB (E_T=2.8 eV) were higher than that of FIrpic (E_T=2.62 eV), so TAPC and TmPyPB were also used to block the triplet excitons within the emissive zone.

Under the electrical excitation, charge recombination in host materials produces singlet and triplet excitons with a ratio of 1:3 (25% singlet excitons and 75% triplet excitons). These

excitons generated in the hosts were transferred to FIrpic through Förster transfer or Dexter transfer. In FIrpic, singlet and triplet excitons were also generated with a ratio of 1:3 by charge trapping. Thus, the excitons in FIrpic were generated in two ways: energy transfer from the host and direct recombination in FIrpic. The singlet excitons in FIrpic can be converted to triplet excitons via intersystem crossing, then these triplet excitons radiatively decay from T_1 to the ground state.

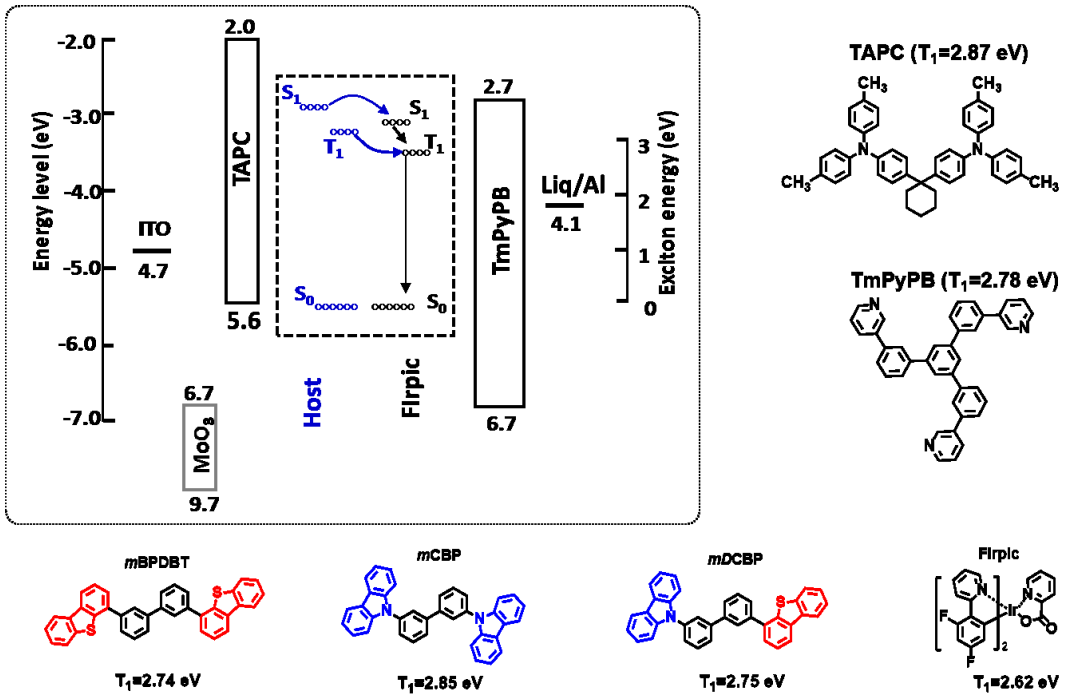

Figure 4.2.7: Energy levels and molecular structures of materials adopted in EL devices.

PhOLEDs characterization

Figure 4.2.8a shows the current density-voltage-luminescence curves of blue PhOLEDs. At the same driving voltage, the current density was highest in *m*DCP-based device and lowest in *m*DCTP-based device. At the same driving voltage, luminescence was also highest in *m*DCP-based device and lowest in *m*DCTP-based device. At 1000 cdm^{-2} for practical applications, the driving voltage was 5.48 V for *m*DCP-based device, lower than that of 5.77 V and 6.13 V for *m*DCBP-based and *m*DCTP-based devices, respectively. With the extended phenyl spacer, the performance of the device slightly decreased, as shown in Figure 4.2.8b. For the device *m*DCP, the maximum current efficiency was 43 cd/A; the maximum power efficiency was 34.8 lm/W; and the maximum external quantum efficiency was 18.6%. These efficiency values were 40.5 cd/A, 29.4 lm/W, and 18.1% for *m*DCBP-based device, and 38 cd/A, 27.1 lm/W and 16.6 % for *m*DCTP-based device, respectively.

All the devices showed almost identical EL spectra with a maximum emission peak around 476 nm and a shoulder emission peak around 500 nm arising from the phosphor FIrpic. There was no other emission peak from the host or charge transport materials, indicating complete energy transfer from host to FIrpic, and excitons were well-confined in the emitting layer. As shown in Figures 4.2.8e and 4.2.8f, the EL spectra of these devices were not changed according to the varied driving voltage of the device because EL emission came only from FIrpic. The Commission International de I'Eclairage coordinates varied quite little for these devices: (0.16, 0.38) and (0.16, 0.39) for *m*DCP-based and *m*DCTP-based devices, respectively. The device performances of PhOLEDs are summarized in Table 4.2.2.

Table 4.2.2 Electroluminescence characteristics of PhOLEDs.

Device	V^a (V)	$\eta_{ce}{}^b$ (cd A^{-1})	$\eta_{pe}{}^b$ (lm W^{-1})	$\eta_{ext}{}^b$ (%)	CIE(x, y)[c]
*m*DCP	5.32	43/42.8/36.5	34.8/34.3/21.6	18.6/17.6/5.6	(0.16, 0.38)
*m*DCBP	5.77	40.5/40.3/35.9	29.4/29.1/19.6	17.9/17.7/15.9	(0.16, 0.38)
*m*DCTP	6.13	36.5/36.1/30.9	25.6/25.0/15.9	16.6/15.9/14.3	(0.16, 0.39)

a: Voltage at 1000 cd m^{-2}.

b: Current efficiency, power efficiency, and external quantum efficiency in the order of maximum, 100 cd m^{-2}, and
at 1000 cd m^{-2}, respectively.

c: Commission international de I'Eclariage coordinates measured at 5 mA/cm^2.

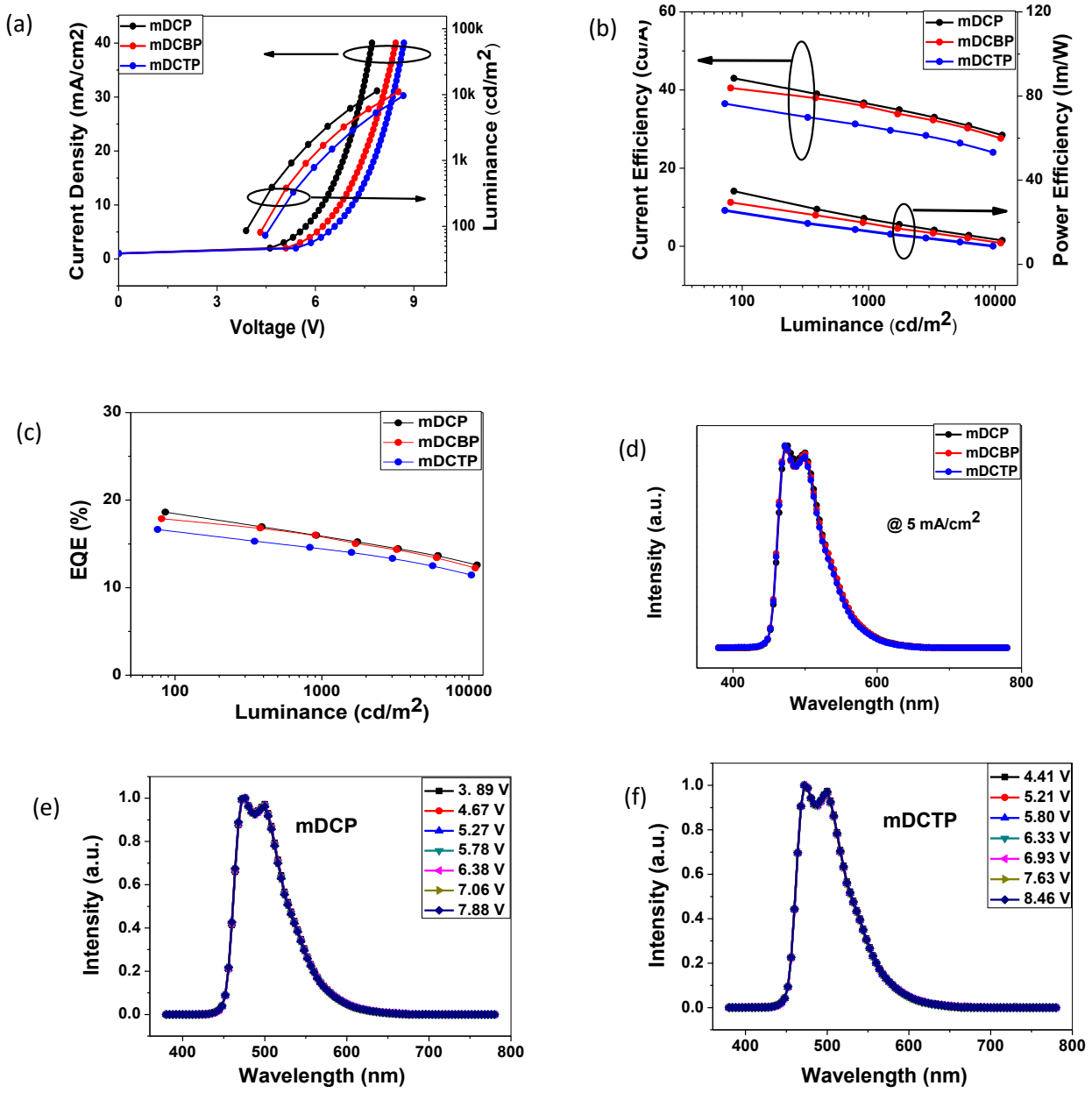

Figure 4.2.8: Device performance: (a) current density-voltage-luminance characteristics; (b) luminance-current efficiency-power efficiency characteristics; (c) luminance-EQE characteristics; (d) EL spectra at 5 mA/cm^2; (e) EL spectra of *m*DCP-based device at varied driving voltage; (f) EL spectra of *m*DCTP-based device at varied driving voltage. Note: The device structure was ITO/MoO_3/TAPC/host:FIrpic/TmPyPB/Liq/Al (host= *m*DCP, *m*DCBP or *m*DCTP).

Analysis

To better understand the charge carrier injection/transport behavior in the emitting layer, the hole- and electron-only devices with doped emitting layer were fabricated. The hole-only device structure was ITO/MoO_3 (3.5 nm)/TAPC (40 nm)/host:FIrpic (8 wt%, 20 nm)/TAPC (10 nm)/Al (120 nm) and the electron-only device structure was ITO/PEIE/BCP (15 nm)/host:FIrpic (8 wt%, 20 nm)/TmPyPB (40 nm)/Liq (2.5 nm)/Al (120 nm) (host= *m*DCP, *m*DCBP or *m*DCTP). The current density-voltage characteristics of these single-carrier-only devices are shown in Figure 4.2.9. At the same driving voltage, the *m*DCP-based device had both highest hole and electron injection and transporting abilities. The enhanced both hole density and electron density in the emitting layer improved the device efficiency of PhOLEDs. The enhanced charge carrier density in the emitting layer also reduced the resistance of the device, thus leading to a low operation voltage.

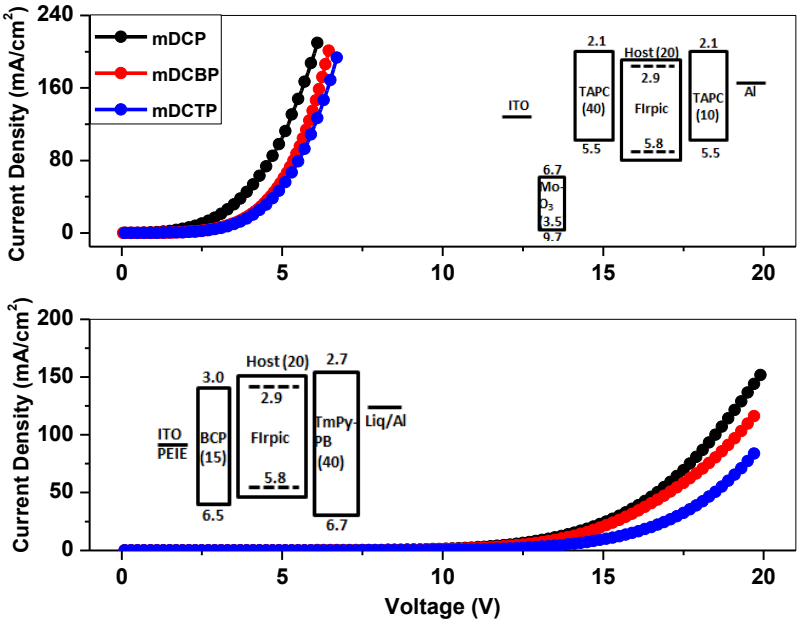

Figure 4.2.9: Current density-voltage characteristics of single-carrier-only devices.

4.2.5 TADF OLEDs characterization

Energy transfer between hosts and emitter

To confirm the applicability of *m*DCP and *m*DCTP as hosts in TADF OLEDs, we investigated the photophysical properties of co-deposited 4CzIPN-doped thin films. The films were 20 nm in thickness with a doping concentration of 6 wt% on quartz substrate. PL spectra of doped thin films showed a maximum emission peak around 510 nm, corresponding to the $S_1 \rightarrow S_0$ transition in 4CzIPN. The emission from the hosts were completely suppressed in all samples, suggesting that the excitons generated on the *m*DCP and *m*DCTP were effectively

transferred to 4CzIPN and converted into light.

To further understand the relationship between the excited states of the host and guest molecules, transient PL decays of doped thin films were measured at a wavelength of 510 nm at room temperature. As shown in Figure 4.2.10b, the doped thin film clearly exhibited a nano-second-scale component and a micro-second-scale component at room temperature. The former was assigned to the prompt component derived from the direct $S_1 \rightarrow S_0$ transition, which has a lifetime (τ_1) of ca. 21 ns; the latter was assigned to the delayed TADF component resulting from the $S_1 \rightarrow S_0$ transition via successive reverse intersystem conversion of the excitons from the T_1 state, which exhibited a lifetime (τ_2) lengthened from 3.3 μs for *m*DCP through 3.29 μs for *m*DCBP to 3.7 μs for *m*DCTP. These indicated that the *m*DCP and *m*DCTP as the host materials can activate the TADF emission of 4CzIPN.

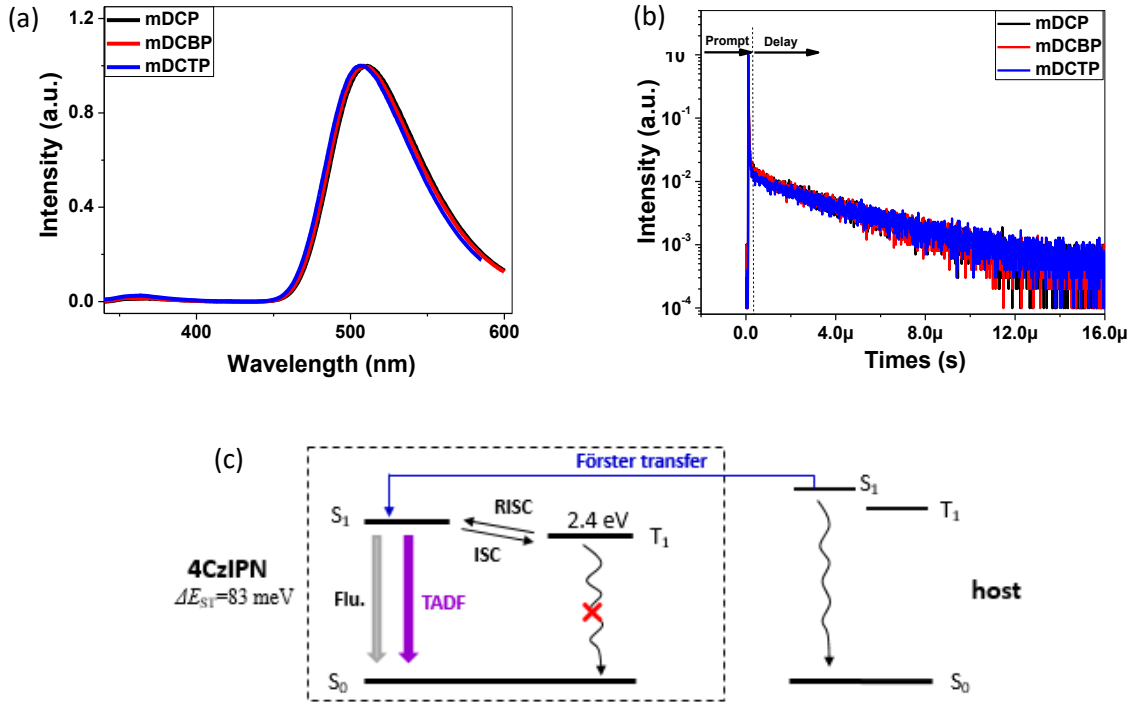

Figure 4.2.10: (a) PL spectra and (b) transient PL decay curves of doped thin films (host:4CzIPN, host= *m*DCP, *m*DCBP or *m*DCTP); (c) schematic illustration of the energy transfer under light excitation.

In hosts, singlet excitons were generated under light excitation and transferred to 4CzIPN through Förster transfer. In 4CzIPN, singlet excitons were also generated under light excitation. Accordingly, the excitons in 4CzIPN were generated in two ways: energy transfer from the host and direct excitation by light. Of these singlet excitons, parts of them radiative decayed to

the ground state ($S_1 \rightarrow S_0$ transition) and those remaining were converted into triplet excitons via intersystem crossing. The T_1 excitons were then converted into S_1 excitons via reverse intersystem crossing ($S_1 \leftarrow T_1$). Finally, the S_1 excitons radiatively decayed to ground state leading to TADF emission. The S_1-T_1-S_1 cycle may be repeated several times before the radiative decay of $S_1 \rightarrow S_0$ transition.

Experimental

In order to evaluate the capability of *m*DCP and *m*DCTP as host materials in TADF OLEDs and to reveal the influence of extended phenyl spacers of the host on the device performance, a series of green emitting devices were fabricated with *m*DCP, *m*DCBP and *m*DCTP as hosts in the following configuration: ITO/HAT-CN (10 nm)/TAPC (40 nm)/TCTA (10 nm)/host:4CzIPN (20 nm, 6 wt%)/TmPyPB (40 nm)/Liq (2.5 nm)/Al (host = *m*DCP, *m*DCBP or *m*DCTP). The chemical structures and energy levels of the materials used in these devices are presented in Figure 4.2.11. HAT-CN and Liq were utilized as hole and electron injection layers, respectively. TAPC and TCTA were served as hole transport layers. Meanwhile, TCTA also can reduced the hole injection barrier from TAPC to the host. TmPyPB was served as an electron transport layer. The triplet energies of TCTA (E_T=2.7 eV) and TmPyPB (E_T=2.8 eV) are higher than that of 4CzIPN (2.42 eV), so TCTA and TmPyPB were chosen as exciton blocker layers to prevent exciton diffusion, thus effectively blocking excitons within the emissive zone.

Under electrical excitation, charge recombination in hosts produced singlet and triplet excitons with a ratio of 1:3 (25% singlet excitons and 75% triplet excitons). The excitons generated on host materials were transferred to 4CzIPN through Förster transfer or Dexter transfer. In 4CzIPN, singlet and triplet excitons were also generated with a ratio of 1:3 by charge trapping. Thus the excitons in 4CzIPN were generated in two ways: energy transfer from the host and direct recombination. In 4CzIPN, some singlet excitons decayed radiatively ($S_1 \rightarrow S_0$ transition) while those remaining were converted into T_1 excitons via intersystem crossing. The T_1 excitons were then converted into S_1 excitons via reverse intersystem crossing ($S_1 \leftarrow T_1$ transition). Finally, the S_1 excitons decayed radiatively to the ground state ($S_1 \rightarrow S_0$ transition). The cycle S_1-T_1-S_1 may be repeated several times before the radiative decay of $S_1 \rightarrow S_0$ transition leading to TADF emission.

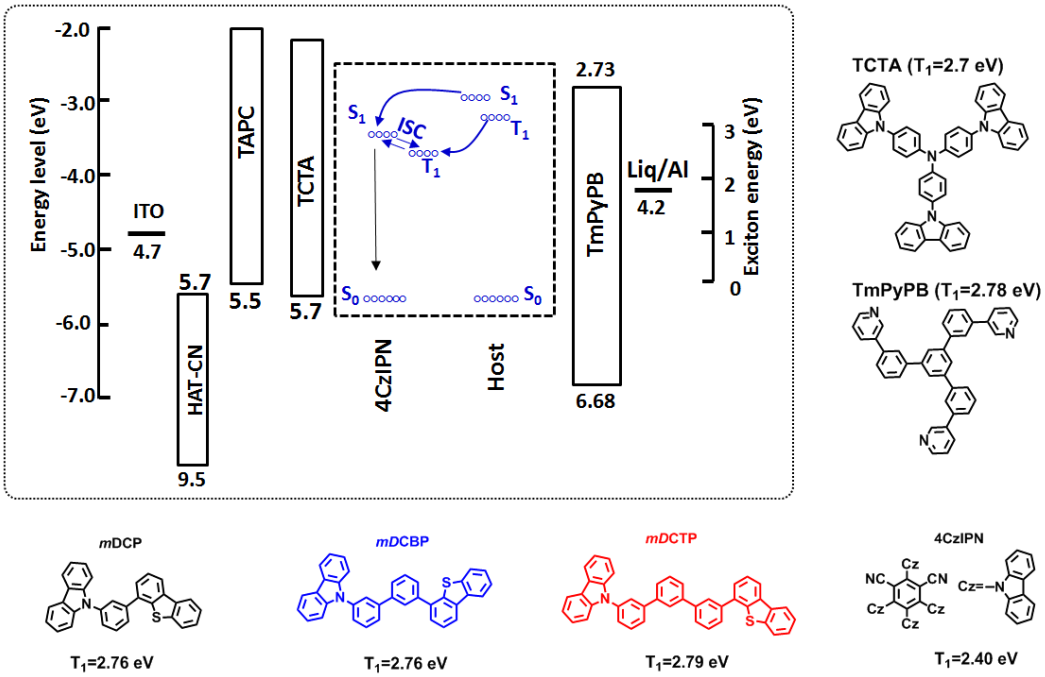

Figure 4.2.11: Energy levels and molecular structures of materials adopted in EL devices.

TADF OLEDs characterization

Figure 4.2.12a shows the current density-voltage-luminescence curves of the TADF OLEDs. At the same driving voltage, the current density was highest in *m*DCP-based device and lowest in *m*DCTP-based device. At same driving voltage, the luminescence was also highest in *m*DCP-based device and lowest in the *m*DCTP-based device. At 1000 cd/m^2 for practical applications, the driving voltage was 4.03 V for device *m*DCP, lower than that of *m*DCBP-based and *m*DCTP-based devices (4.39 V and 5.00 V, respectively). With the extended phenyl spacer, the performance of the device slightly decreased. For *m*DCP-based device, the maximum current efficiency was 68.0 cd/A; the maximum power efficiency was 60.3 lm/W; and the maximum external efficiency quantum efficiency was 21%. These efficiency values were 68.0 cd/A, 51.8 lm/W, and 19.4% for *m*DCBP-based device, 64.5 cd/A, 47.0 lm/W and 19.03% for *m*DCTP-based device, respectively.

All the devices showed almost identical EL spectra with a maximum emission peak at 520 nm arising from the typical emission of 4CzIPN. There was no other radiative emission peak from the host or charge transport materials, indicating complete energy transfer from the host to 4CzIPN and excitons were-confined within the emitting layer. The EL spectra of these devices remained consistent according to the driving voltage of the device, because the EL emission came only from the 4CzIPN. The commission International de I′Eclairage coordinates

were (0.26, 0.58) and (0.29, 0.58) for *m*DCP-based and *m*DCTP devices, respectively. All of the aforementioned characterization data of TADF OLEDs are summarized in Table 4.2.3.

Table 4.2.3 Electroluminescence characteristics of TADF OLEDs.

Device	V^a (V)	$\eta_{ce}{}^b$ (cd A^{-1})	$\eta_{pe}{}^b$ (lm W^{-1})	$\eta_{ext}{}^b$ (%)	CIE(x, y)[c]
*m*DCP	4.03	68.0/-/64.5	60.3/-/49.7	21.0/-/19.9	(0.26, 0.58)
*m*DCBP	4.71	66.0/65.8/62.0	51.8/51.4/41.5	19.4/19.3/18.2	(0.31, 0.59)
*m*DCTP	5.00	64.5/-/60.0	47.0/-/37.5	19.0/-/17.8	(0.29, 0.58)

[a]: Voltage at 1000 cd m^{-2}.

[b]: Current efficiency, power efficiency, and external quantum efficiency in the order of maximum, 100 cd m^{-2}, and
at 1000 cd m^{-2}, respectively.

[c]: Commission international de I'Eclariage coordinates measured at 5 mA/cm^2.

Analysis

To better understand the charge carrier injection/transport behavior in the host:4CzIPN layer, the hole- and electron-only devices with doped emitting layer were fabricated. The hole-only device structure was ITO/HAT-CN (10 nm)/TAPC (40 nm)/host:4CzIPN (6% wt, 20 nm)/TAPC (10nm)/Al (120 nm) and the electron-only device structure was ITO/PEIE/BCP (15 nm)/host:4CzIPN (6%, 20nm)/TmPyPB (40 nm)/Liq (2.5 nm)/Al (120 nm) (host= *m*DCP, *m*DCBP, or *m*DCTP). Clearly, at the same driving voltage, *m*DCP-based device had highest both hole and electron injection and transporting ability. The enhanced both hole density and electron density in the emitting layer improved the efficiency of TADF OLEDs. The enhanced charge carrier injection and transport abilities of the emitting layer also reduced the resistance of TADF OLEDs, leading to the low operation voltage.

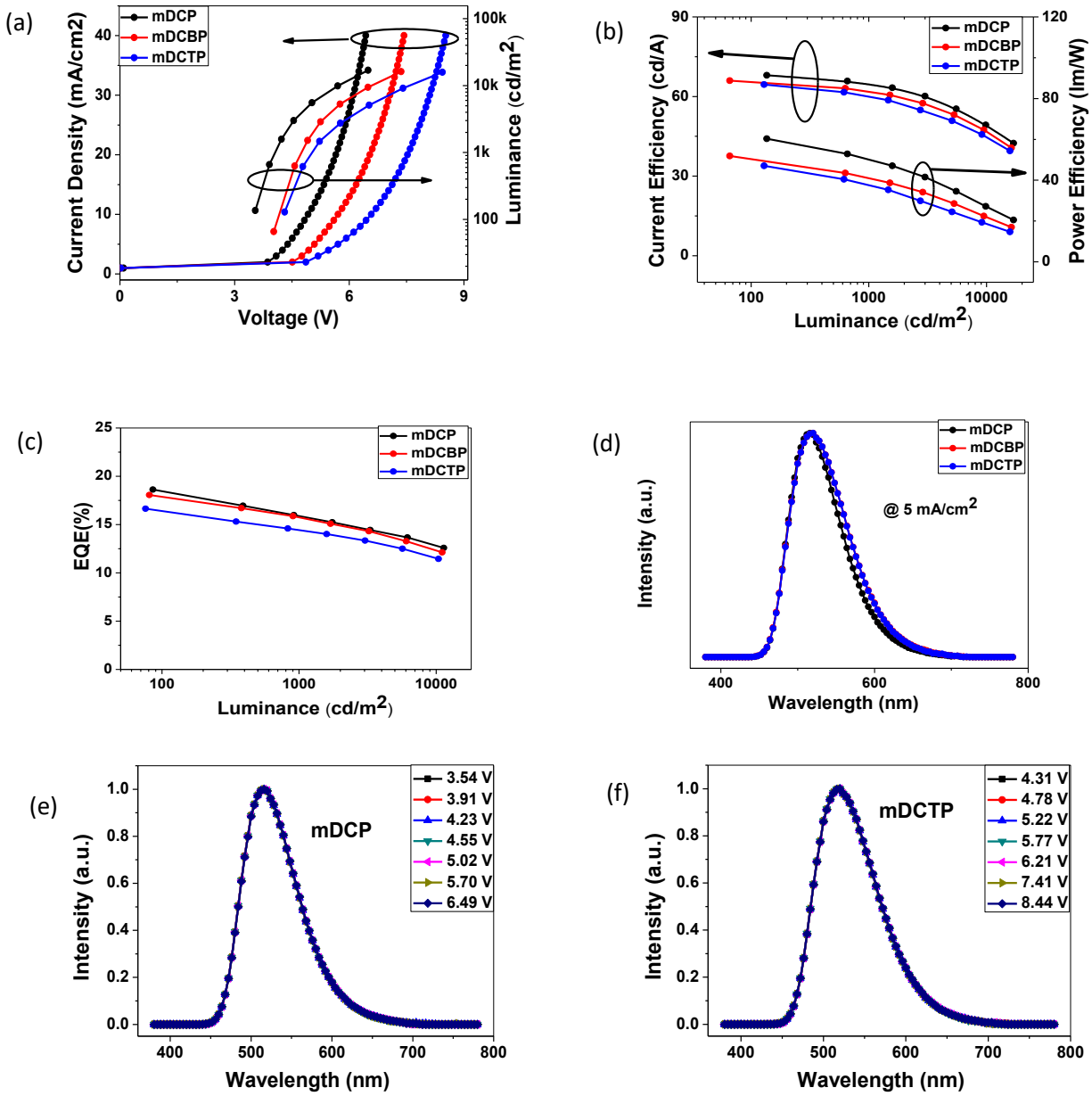

Figure 4.2.12: Device performance: (a) current density-voltage-luminance characteristics; (b) luminance-current density-power efficiency characteristics; (c) luminance-EQE characteristics; (d) EL spectra at 5 mA/cm^2; (e) EL spectra of *m*DCP-based device at varied driving voltage; (f) EL spectra of *m*DCTP-based device at varied driving voltage. Note: The device structure was ITO/HAT-CN/TAPC/TCTA/host:4CzIPN/TmPyPB/Liq/Al (host = *m*DCP, *m*DCBP or *m*DCTP).

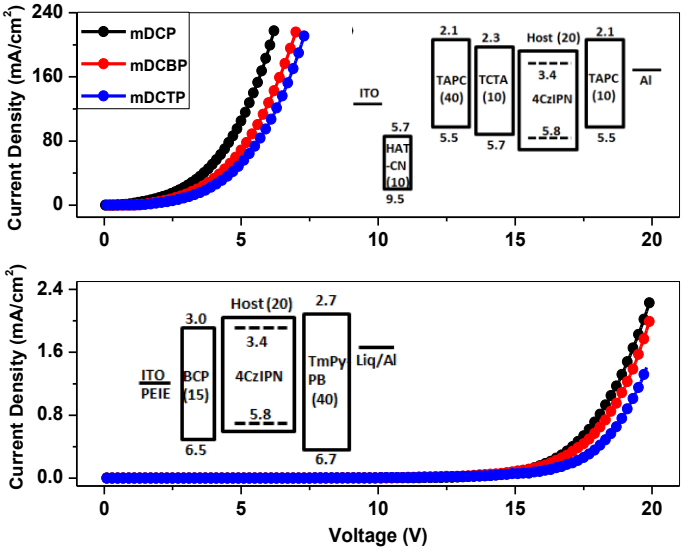

Figure 4.2.13: Current density-voltage characteristics of single-carrier-only devices.

4.2.6 Summary

Two new host materials, *m*DCP and *m*DCTP, with dibenzothiophene and carbazole groups connected by extended phenyl spacers were investigated. Their thermal, photophysical and electrical properties of them were fully investigated. The *meta*-bonding design endowed them with high triplet energy than 2. 7 eV, making them excellent potential host candidates for sky blue and green OLEDs. As the phenyl spacer extended, the hybrids exhibited gradually increased thermal stability as characterized by TGA and DSC analysis. As a merit of *meta*-linkage, the extended phenyl spacers did not affect their photophysical properties significantly. With the extended phenyl spacer, the device performance was slightly decreased. By employing *m*DCP as host, the blue PhOLEDs produced a maximum current efficiency of 43 cd/A, power efficiency of 34.8 lm/W, and external quantum efficiency of 18.6%; the green TADF OLEDs showed a maximum current efficiency of 66 cd/A, power efficiency of 60.3 lm/W, and external quantum efficiency of 21%. This study provide insight into the structure-property relationship of carbazole/dibenzothiophene moieties, and demonstrate that utilizing a suitable phenyl spacer to connect the molecular moiety is effective in adjusting the properties of carbazole- or dibenzothiophene-based host materials.

4.3 Carbazole/dibenzothiophene derivatives with different carbazole to dibenzothiophene ratios as host materials in modern OLEDs

4.3.1 Introduction

It had been well known that balanced charge carrier injection and transport in the emission layer were required in high performance OLEDs. Accordingly, host materials that contain both hole transporting and electron transporting moieties were utilized to facilitate charge carrier balance and enhance device efficiency [166-170]. In general, the charge carrier injection/transport ability of host materials can be accurately modulated by tuning the number and the mixing ratio of electron-donating and electron-withdraw units [167, 171, 172]. To gain insight into the molecular structure-function relationship of the number and ratio of carbazole to dibenzothiophene moieties, in this study, two carbazole/dibenzothiophene derivatives, with different carbazole/dibenzothiophene unit ratios were investigated. Their physical, photophysical, and electrical properties were systematically investigated and the device performance of blue PhOLEDs and green TADF OLEDs based on them were detailed investigated. As discussed below, we also explore how the charge carrier balance in the emitting layer can be fine-tuned by adjusting the ratio of carbazole to dibenzothiophene moieties were also discussed.

4.3.2 Molecular synthesis

The host materials *m*DC2BP and *m*D2CBP were synthesized by a project partner (Dr. Shoucheng Dong) at Soochow University. Scheme 4.3.1 illustrates the synthesis route of the host materials. The synthesis was straightforward with classic Suzuku-Miyaura reaction.

*m*DC2BP: 9,9'-(5-bromo-1,3-phenylene) bis (9H-carbazole) (1.00 g, 2.05 mmol), 2-(3-(dibenzothiophen-4-yl) phenyl)-4,4,5,5-tetramethyl-1,3,2-dioxaborolane (0.95 g, 2.46 mmol) were dissolved in THF/2 M K_2CO_3 (45 ml, 3/1, v/v) in a Schlenk tube under argon. The resulting mixture was refluxed for 12 h. After cooling to room temperature, the organic layer was collected and annealed to remove the residual solvent. The crude product was purified by column chromatography on silica gel using dichloromethane/petroleum (1/5, v/v) as eluent, followed by recrystallization from ethyl acetate/petroleum and vacuum sublimation successively. The final product was a white powder (0.86 g, 62.9%). ^{1}H NMR (400 MHz, CDCl3) δ (ppm): 8.16 (d, J = 8.0 Hz, 7H), 8.04 (d, J = 1.6 Hz, 2H), 7.75-7.86 (m, 4H), 7.62-7.67 (m, 5H), 7.54-7.57 (m, 2H), 7.42-7.49 (m, 6H), 7.32 (t, J = 7.2 Hz, 4H). ^{13}C NMR (100 MHz, CDCl3) δ (ppm): 144.6, 141.8, 140.8, 140.1, 140.0, 139.6, 138.7, 136.6, 136.5, 135.9,

130.0, 128.5, 127.3, 127.1, 127.0, 126.5, 125.4, 124.7, 124.6, 124.1, 123.9, 122.9, 122.0, 121.0, 120.7, 120.6, 110.0. MS (EI): m/z 666.2 (M+). Anal. calcd for $C_{48}H_{30}N_2S$ (%): C 86.46, H 4.53, N 4.20; found: C 86.11, H 4.24, N 4.12.

*m*D2CBP: 4,4'-(5-bromo-1,3-phenylene) di-dibenzothiophene (0.5 g, 0.96 mmol), (3-(9H-carbazol-9-yl) phenyl) boronic acid (0.42 g, 1.46 mmol) were dissolved in THF/2 M K_2CO_3 (45 ml, 3/1, v/v) in a Schlenk tube under argon. The resulting mixture was refluxed for 12 h. After cooling to room temperature, the organic layer was collected and annealed to remove the residual solvent. The crude product was purified by column chromatography on silica gel using dichloromethane/petroleum (1/5, v/v) as eluent, followed by recrystallization from ethyl acetate/petroleum and vacuum sublimation successively. The final product was a white powder (0.40 g, 61.0%). ^{1}H NMR (400 MHz, CDCl3) δ (ppm): 8.10-8.22 (m, 9H), 8.02 (t, J = 1.6 Hz, 1H), 7.87 (d, J = 8.0 Hz, 1H), 7.80-7.85 (m, 2H), 7.73 (t, J = 8.0 Hz, 1H), 7.51-7.67 (m, 7H), 7.43-7.50 (m, 4H), 7.40 (t, J = 8.4 Hz, 2H), 7.28 (t, J = 7.2 Hz, 2H). ^{13}C NMR (100 MHz, CDCl3) δ (ppm): 142.8, 142.2, 141.5, 141.0, 139.7, 138.8, 138.7, 136.6, 136.5, 136.0, 130.7, 127.8, 127.3, 127.1, 126.8, 126.5, 126.4, 126.3, 126.1, 125.5, 124.7, 123.7, 122.9, 122.0, 121.1, 120.5, 120.2, 110.1. MS (EI): m/z 683.2 (M+). Anal. calcd for $C_{48}H_{29}NS_2$ (%): C 84.30, H 4.27, N 2.05; found: C 83.98, H 4.01, N 1.98.

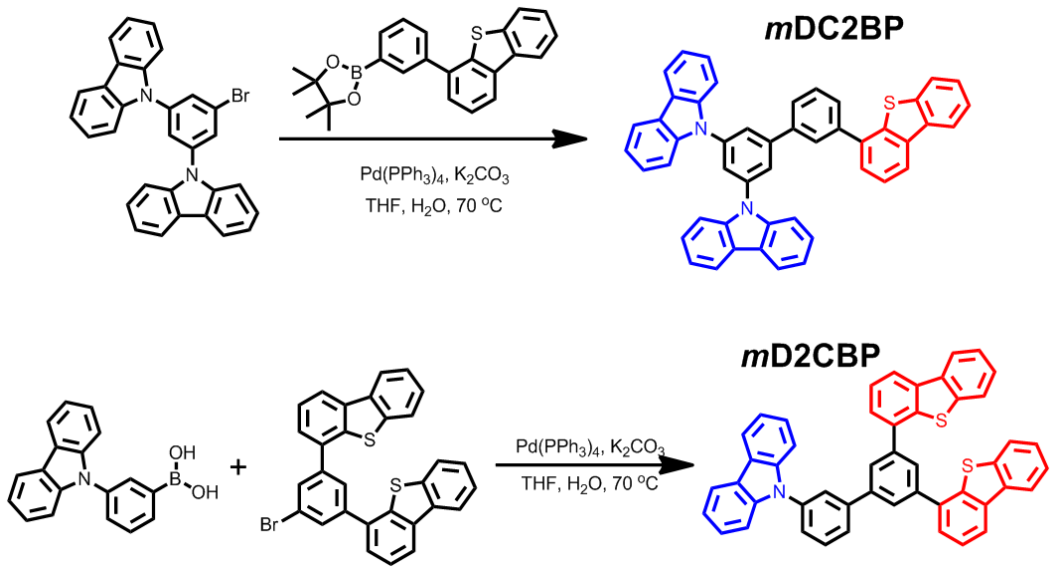

Scheme 4.3.1: Synthesis of carbazole/dibenzothiophene derivatives.

4.3.3 Fundamental physical properties

Quantum chemical calculations

To understand the molecular structure-property relationship of *m*D2CBP and *m*DC2BP at the molecular level, the HOMO and LUMO orbital spatial distributions were obtained by the density function theory calculations at the (B3LYP)/6-31G (d) level with Gaussian program [154]. Figure 4.3.1 shows the HOMO and LUMO distributions of *m*DCBP, *m*D2CBP, and *m*DC2BP. In the three compounds, the HOMO orbitals were mainly distributed over one carbazole moiety and the adjacent phenyl ring due to the strong electron-donating nitrogen unit of carbazole, whereas the LUMO orbitals were mainly distributed on the one dibenzothiophene moiety and spread over all the phenyl spacer. This indicated that carbazole is a hole transport unit and dibenzothiophene is an electron transport unit in the materials. Therefore, *m*D2CBP and *m*DC2BP would exhibit electron-accepting properties as well as hole-accepting properties from charge transport materials.

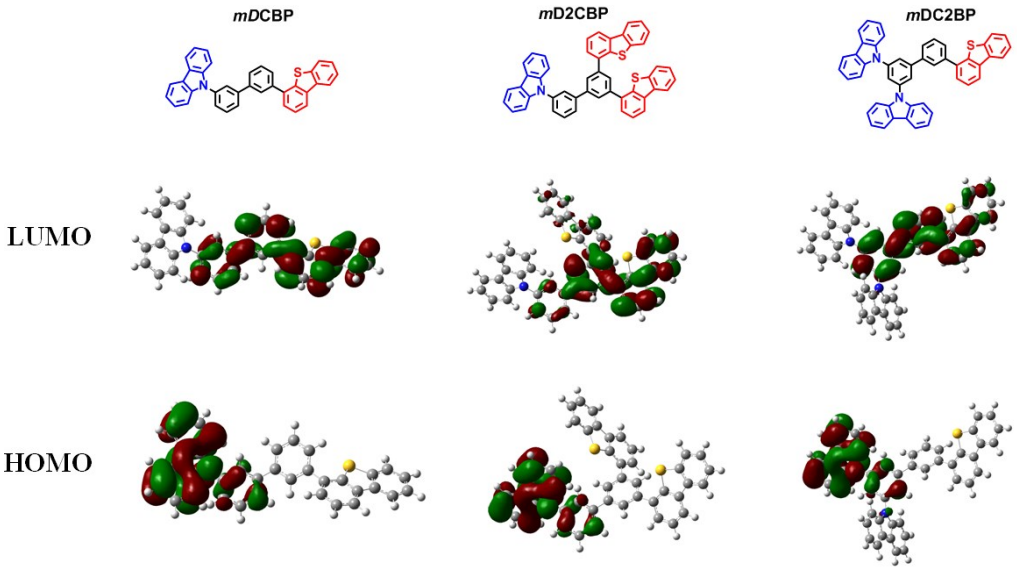

Figure 4.3.1: HOMO and LUMO spatial distributions of carbazole/dibenzothiophene derivatives.

Thermal analysis

The thermal stabilities of these three hybrids were characterized by TGA and DSC because the thermal stability is closely related to the device stability. Figure 4.3.2 shows the DSC and TGA thermograms of *m*DCBP, *m*D2CBP, and *m*DC2BP. The values of glass transition temperature of *m*D2CBP was observed at 140˚C, similar with that of *m*DC2BP (136˚C), and higher than that of *m*DCBP (88 ˚C). All the decomposition temperatures of these three materials were observed over 400˚C in TGA: 509˚C for *m*D2CBP and 488˚C for *m*DC2BP. Thermal

stability was enhanced as carbazole or dibenzothiophene moieties increased due to the increased molecular size and weight. The good thermal stability of *m*D2CBP and *m*DC2BP could improve film morphology and reduce the formation of aggregation upon heating, thus they could be used in long-lifetime OLEDs.

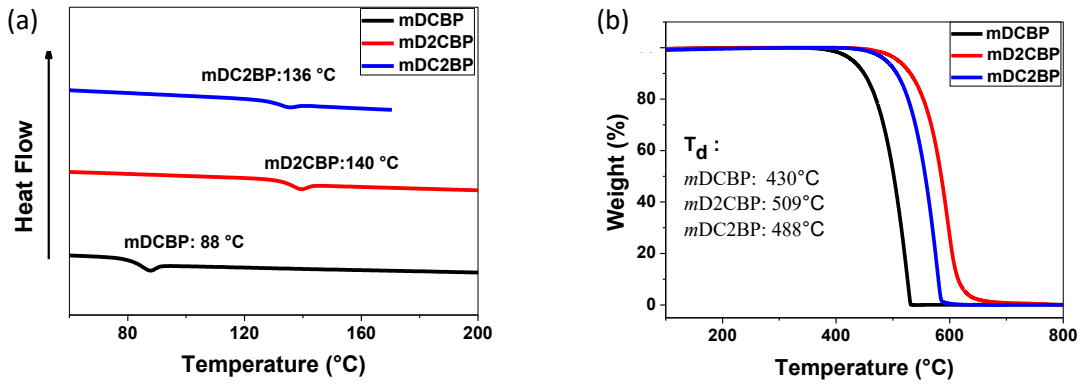

Figure 4.3.2: DSC traces and (b) TGA traces recorded at a heating rate of 10˚C min^{-1}.

Photophysical properties

The photophysical properties of *m*DCBP, *m*D2CBP, and *m*DC2BP were investigated by means of UV-Vis absorption, PL, and phosphorescence spectra, as shown in Figure 4.3.3. The (a) Vis absorption and PL spectra of the compounds were obtained from vacuum evaporated thin films (60 nm) and phosphorescence spectra we (b) asured in 2Me-THF at 77 K. *m*D2CBP and *m*DC2BP showed almost identical UV-Vis absorption and PL spectra. The relatively weak shoulder peaks at ca. 355 nm can be attributed to the n-π* transitions of the carbazole group [30, 156]. The optical bandgap was determined by the onset of UV-Vis absorption spectra. The absorption edges of the spectra for *m*D2CBP, *m*DC2BP were 364 nm and 362 nm, respectively, corresponding to the optical bandgaps of 3.41 eV and 3.43 eV. The maximum PL emission peaks of *m*D2CBP and *m*DC2BP were 386 nm and 390 nm, respectively, corresponding to singlet energy levels of 3.21 eV and 3.17 eV. The PL emission of *m*D2CBP and *m*DC2BP showed a red-shift compared to that of *m*DCBP. A FWHM ranging from 46 nm in *m*DCBP through 57 nm in *m*D2CBP to 60 nm in *m*DC2BP was observed. All materials exhibited broad phosphorescent spectra; the triplet energies were calculated by the first emission peak of phosphorescent spectra ($T_1^{v=0} \rightarrow S_0^{v=0}$). The triplet energies of *m*DCBP, *m*D2CBP, and *m*DC2BP were all above 2.7 eV, which were 2.75 eV, 2.73 eV, and 2.74 eV, respectively, sufficient for use as host materials for sky blue and green triplet emitters in practice.

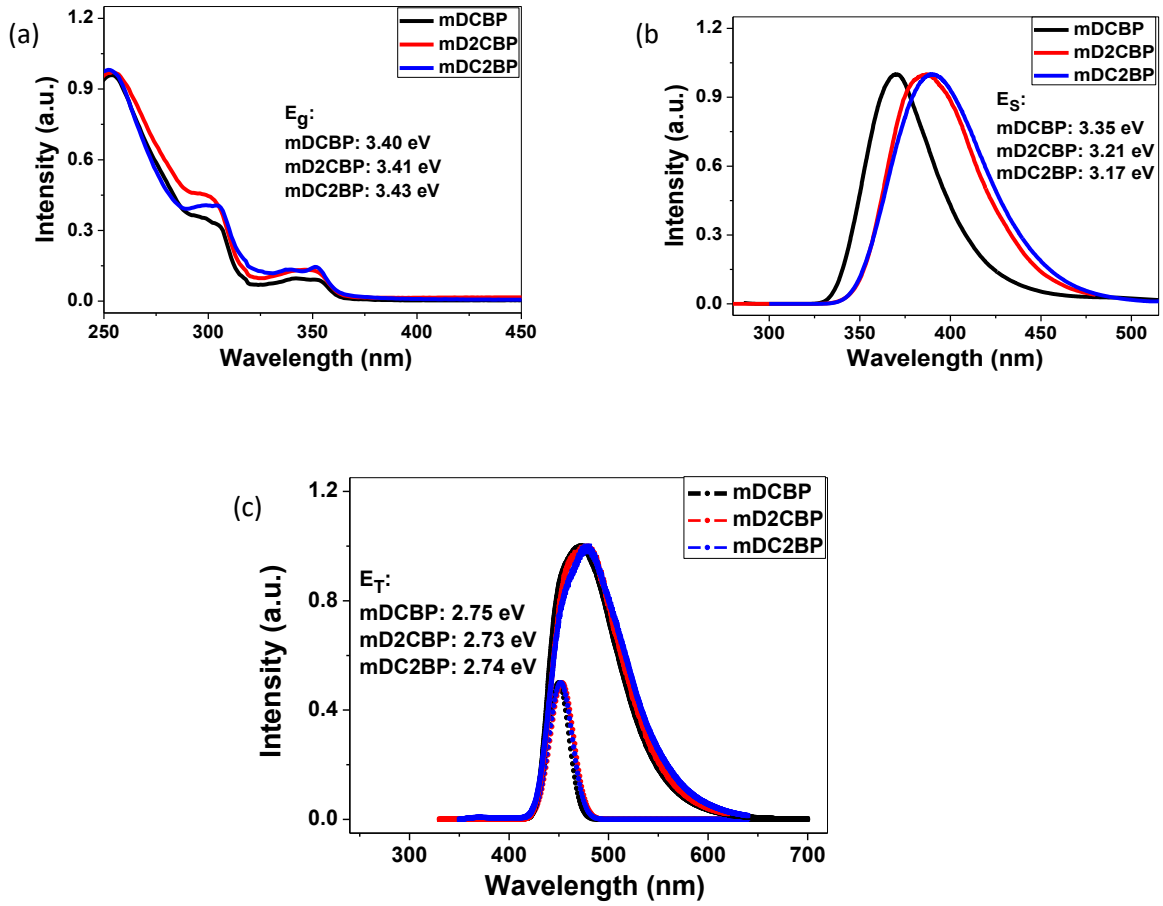

Figure 4.3.3: (a) UV-Vis absorption and (b) PL spectra of vacuum deposited thin films; (c) phosphorescence spectra in frozen 2-MeTHF matrix at 77 K.

HOMO/LUMO levels

For host materials, appropriate HOMO and LUMO levels are essential for the efficient injection of carriers into the emitting layer. In this study, the HOMO levels of the materials were determined by UPS to be -6.01 eV, -5.98 eV, and -5.99 eV for *m*DCBP, *m*D2CBP and *m*DC2BP, respectively. The LUMO levels were calculated using HOMO levels and optical bandgap in solid films, according to the equation $E_{LUMO}=E_{HOMO}+E_g$, so the LUMO levels of *m*DCBP, *m*D2CBP, and *m*DC2BP were -2.61 eV, -2.57 eV, and -2.56 eV, respectively. Table 4.3.1 summarizes the physical data for the three materials.

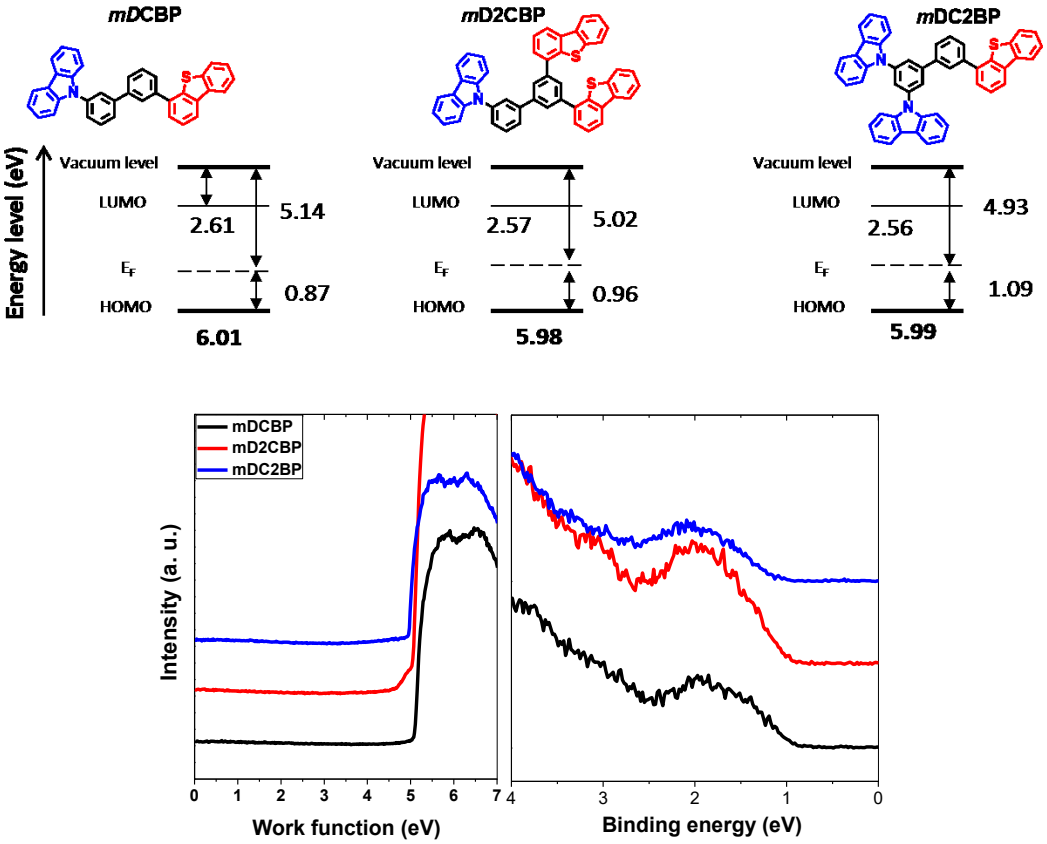

Figure 4.3.4: UPS spectra carbazole/dibenzothiophene derivatives.

Table 4.3.1: Summary of physical properties of carbazole/dibenzothiophene derivatives.

Compounds	T_g[a] (°C)	T_d[b] (°C)	PL λ_{max}[c] (nm)	E_T[d] (eV)	E_g[e] (eV)	HOMO[f] (eV)	LUMO[g] (eV)
*m*DCBP	88	430	370	2.75	3.40	-6.01	-2.61
*m*D2CBP	136	509	386	2.73	3.41	-5.98	-2.57
*m*DC2BP	140	488	391	2.74	3.43	-5.99	-2.56

[a]: Glass transition temperatures; [b]: Decomposition temperatures.

[c]: Measured from vacuum deposited thin film (60 nm).

[d]: Estimated from the first emission peak of phosphorescence spectra (measured in 2-MeTHF matrix at 77 K).

[e]: Optical bandgap energies calculated from the corresponding absorption spectra onset.

[f]: HOMO levels calculated from UPS data.

[g]: LUMO levels calculated from HOMO and E_g of vacuum deposited thin films.

Carrier-transport properties

To evaluate their charge carrier transporting ability, single-carrier devices were fabricated. The hole-only device had the following structure: ITO/MoO_3 (10 nm)/host (100 nm)/MoO3 (10 nm)/Al and the electron-only device had the following structure: ITO/PEIE/BCP (15 nm) /host (100 nm)/BCP (15 nm)/Liq (2.5 nm)/Al (host = *m*DCBP, *m*D2CBP and *m*DC2BP). At the same electrical field intensity, the electron current densities were much lower than the hole current densities. The devices exhibited higher hole current density as carbazole units increased and higher electron current density as dibenzothiophene units increased. In the carbazole/dibenzothiophene derivatives, increasing the molar ratio of p-type unit seemed to be an effective strategy to improve the hole transport ability; and increasing the molar ratio of the n-type unit seemed to be an effective strategy to improve the electron transport ability. In hole-only devices, the current density-voltage characteristics of these samples showed two distinct regions at low and high bias, a Schottky thermionic region and a SCLC region. The hole mobility of *m*D2CBP and *m*DC2BP were estimated by fitting the current density-voltage curves of SCLC region according to the Mott-Gurney equation [87, 88]

$$J = \frac{9}{8}\varepsilon\varepsilon_0 \frac{V^2}{d^3}\mu \tag{4.3.1}$$

where J is the current density; V is applied voltage; ε is the relative permittivity; ε_0 is the permittivity of the free space; d is the thickness of active layer; and μ is the charge carrier mobility. Under an electric field of 0.8 MV/cm, the estimated hole mobility of 100 nm *m*D2CBP is 3.8×10^{-4} cm^2/Vs. And under an electric field of 0.5 MV/cm, the estimated hole mobility of 100 nm *m*DC2BP is 7.6×10^{-3} cm^2/Vs.

4.3.4 PhOLEDs characterization

Energy transfer between hosts and emitter

To confirm the applicability of *m*D2CBP and *m*DC2BP as the hosts for PhOLEDs, we investigated the photophysical properties of co-deposited thin films of host:FIrpic (host= *m*DCBP, *m*D2CBP, or *m*DC2BP). The films were 20 nm in thickness with a FIrpic doping concentration of 8 wt% on quartz substrate. For the PL spectra of doped thin film (Figure 4.3.6a), all samples showed an emission peak around 476 nm and a shoulder emission peak around 500 nm corresponding to the FIrpic emission. For the sample *m*DC2BP, the relatively slight PL emission peak around 390 nm corresponding to the emission of *m*DC2BP was

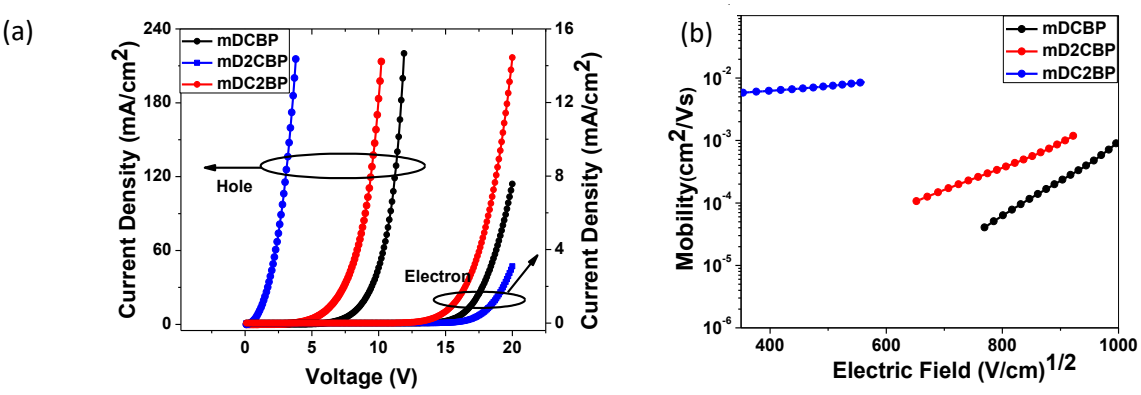

Figure 4.3.5: (a) Current density-voltage curves of single-carrier devices; (b) mobility-square root of electric field. Note: The hole-only device structure was ITO/MoO_3/host/MoO_3/Al and the electron-only device structure was ITO/PEIE/BCP/host/BCP/Liq/Al (host = *m*DCBP, *m*D2CBP and *m*DC2BP).

observed, indicating incomplete singlet energy transfer from host to luminescent FIrpic, which would decrease the device performance.

To further understand the relationship between the excited states of the hosts and guest molecules, transient PL decays of doped thin films were measured at a wavelength of 476 nm at room temperature (Figure 4.3.6b). Although these films did not exhibit mono-exponential decay curves, the second exponential decay portions were fewer than their first exponential decay portions, indicating that due to high E_T, the energy transfer from the hosts to FIrpic was energetically favorable, and the energy transfer from FIrpic back to the hosts was suppressed, thus the energy was well-confined in luminescent FIrpic. All the transient PL decay curves were fitted exponentially with decay analysis software (DAS 6, Horiba) and showed relatively long excited state lifetime: 1.41 μs for *m*DCBP, 1.70 μs for *m*D2CBP, and 2.03 μs for *m*DC2BP. In hosts, singlet excitons were generated under light excitation, then transferred to FIrpic through Förster transfer. In FIrpic, singlet excitons were also generated under light excitation. Thus, the excitons in FIrpic were generated in two ways: energy transferred from the host and direct excitation by light. The singlet excitons in FIrpic were converted to triplet excitons via intersystem crossing, then these triplet excitons radiatively decayed from T_1 to the ground state ($T_1 \rightarrow S_0$ transition) and converted into phosphorescence emission.

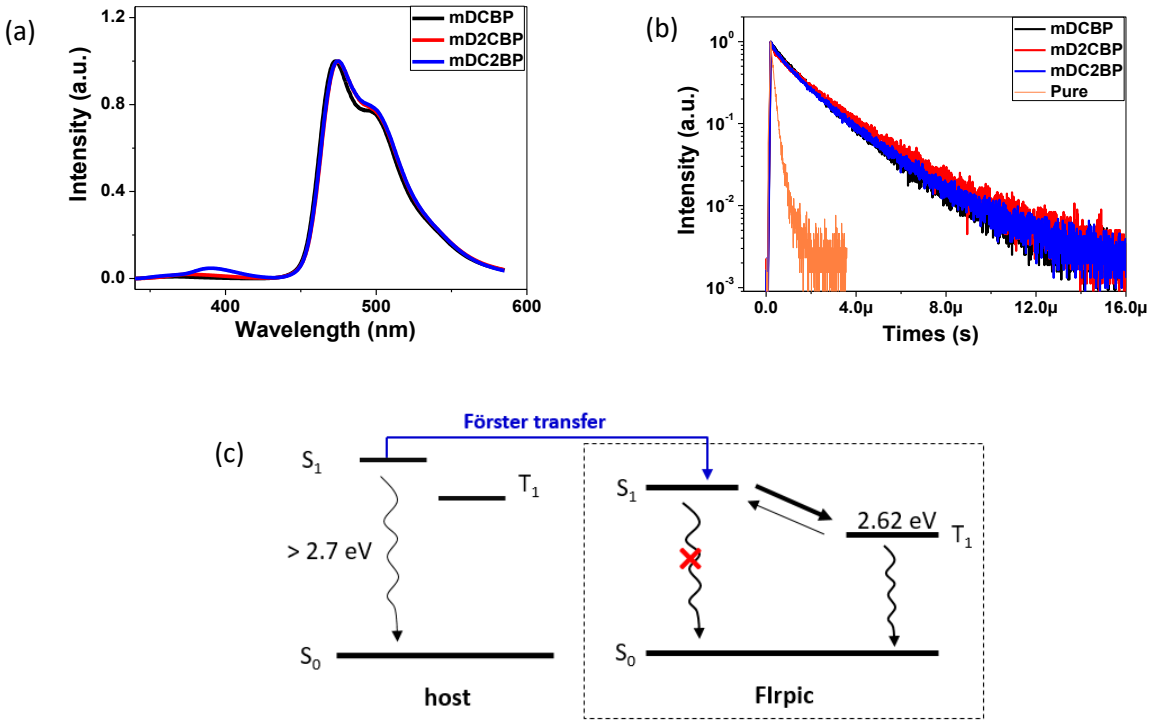

Figure 4.3.6: (a) PL spectra and (b) transient PL decay curves of doped thin films (host:FIrpic, host= *m*DCBP, *m*D2CBP, or *m*DC2BP); (c) schematic illustration of the energy transfer process under light excitation.

Experimental

To evaluate the capability of *m*D2CBP and *m*DC2BP as host materials for blue phosphors and to reveal the influence of different carbazole/dibenzothiophene moiety ratios on the device performance, a group of FIrpic-based PhOLEDs were constructed with a typical sandwich structure. The detailed device configuration was ITO/MoO_3 (3.5 nm)/TAPC (40 nm)/host:FIrpic (20 nm, 8wt%)/TmPyPB (40 nm)/Liq (2.5 nm)/Al (host= *m*DCBP, *m*D2CBP, or *m*DC2BP). MoO_3 and Liq were utilized as hole and electron injection layers, respectively. TAPC and TmPyPB were served as hole and electron transport layers, respectively. There were large energy barriers for electron leakage from hosts to TAPC and hole leakage from hosts to TmPyPB, so TAPC and TmPyPB were also used as electron and hole blocking layers, respectively. The triplet energies of TAPC (E_T=2.9 eV) and TmPyPB (E_T=2.8 eV) were higher than that of FIrpic (E_T=2.62 eV), so TAPC and TmPyPB were utilized to block excitons within the emissive layer.

Under the electrical excitation, charge recombination in host materials produced singlet and triplet excitons with a ratio of 1:3 (25% singlet excitons and 75% triplet excitons). These

excitons generated on the host transferred to FIrpic through Förster transfer or Dexter transfer. In FIrpic, singlet and triplet excitons were also generated with a ratio of 1:3 by charge trapping. So the excitons in FIrpic were generated in two ways: energy transfer from the hosts and direct recombination. The singlet excitons on FIrpic were converted to triplet excitons via intersystem crossing, then the triplet excitons radiatively decayed from T_1 to the ground state and converted into phosphorescence emission.

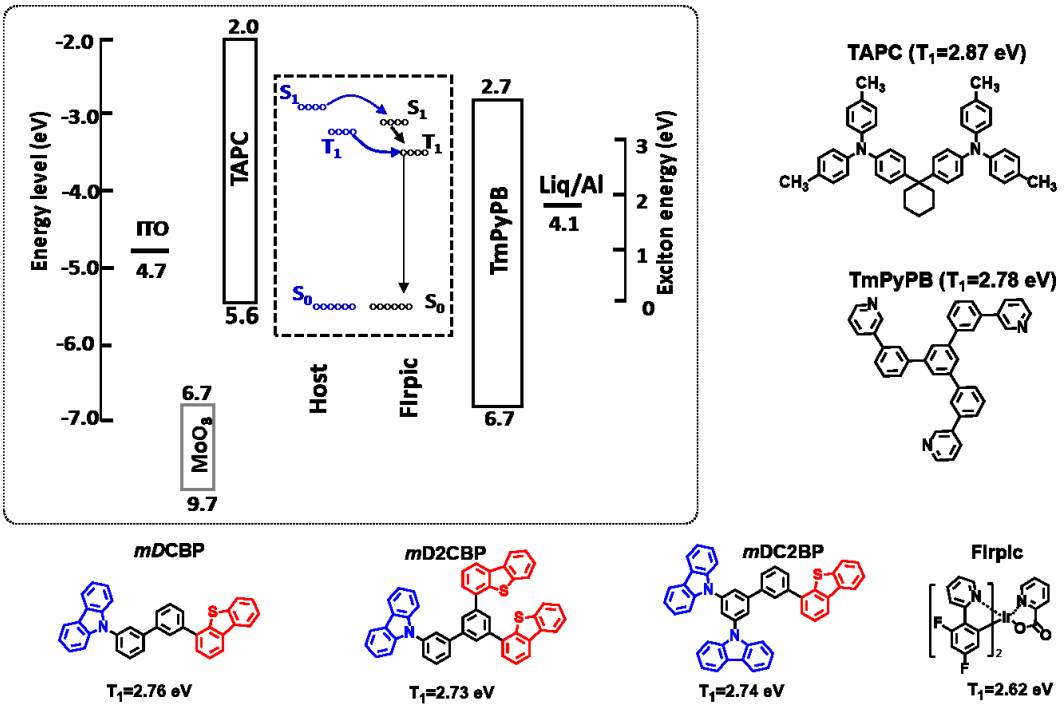

Figure 4.3.7: Energy levels and molecular structures of materials adopted in EL devices.

PhOLEDs characterization

Figure 4.3.8a shows the current density-voltage-luminescence curves of the blue PhOLEDs. At the same driving voltage, the current density was highest in *m*DC2BP-based device and lowest in the *m*DCBP-based device. And at same voltage, the luminescence was also highest in *m*DC2BP-based device and lowest in the *m*DCBP-based device. At 1000 cd/m^2 for practical applications, the driving voltages were 5.77 V, 5.60 V and 5.54 V for *m*DCBP-based, *m*D2CBP-based, and *m*DC2BP-based devices, respectively. With a 1:1 mixing ratio of carbazole and dibenzothiophene moiety, *m*DCBP-based device showed highest efficiency compared to other two. Its maximum current efficiency was 40.5 cd/A; maximum power efficiency was 29.4 lm/W; and maximum external quantum efficiency of the *m*DCBP-based device was 18.1%. These efficiency values were 34.5 cd/A, 26.6 lm/W, and 14.5% for *m*D2CBP-based device, 33 cd/A, 25.9 lm/W, and 13.9 % for *m*DC2BP, respectively.

All devices showed EL spectra with a maximum emission peak at 476 nm and a shoulder emission peak at 500 nm arising from the phosphor FIrpic. There were no other emission peaks from the hosts or charge transport materials, indicating the complete energy transfer from the hosts to FIrpic and exciton confinement inside the emitting layer. The EL spectra of these devices remained stable under varied driving voltage because the EL emission came only from FIrpic, as shown in Figures 4.3.8 (e) and (f). The Commission International de I'Eclairage coordinates were (0.17, 0.41) and (0.18, 0.40) for *m*D2CBP-based and *m*DC2BP-based devices, respectively. The device performances of PhOLEDs are summarized in Table 4.3.2.

Table 4.3.2 Electroluminescence characteristics of PhOLEDs.

Device	V^a (V)	$\eta_{ce}{}^b$ (cd A^{-1})	$\eta_{pe}{}^b$ (lm W^{-1})	$\eta_{ext}{}^b$ (%)	CIE(x, y)[c]
*m*DCBP	5.77	40.5/40.3/35.9	29.4/29.1/19.6	17.9/17.7/15.9	(0.16, 0.38)
*m*D2CBP	5.60	34.5/34.2/29.6	26.6/25.9/16.7	14.5/14.0/12.3	(0.17, 0.41)
*m*DC2BP	5.54	33/32.8/28.0	25.9/25.2/15.9	13.9/13.5/11.7	(0.17, 0.40)

[a]: Voltage at 1000 cd m^{-2}.

[b]: Current efficiency, power efficiency, and external quantum efficiency in the order of maximum, 100 cd m^{-2}, and
at 1000 cd m^{-2}, respectively.

[c]: Commission international de I'Eclariage coordinates measured at 5 mA/cm^2.

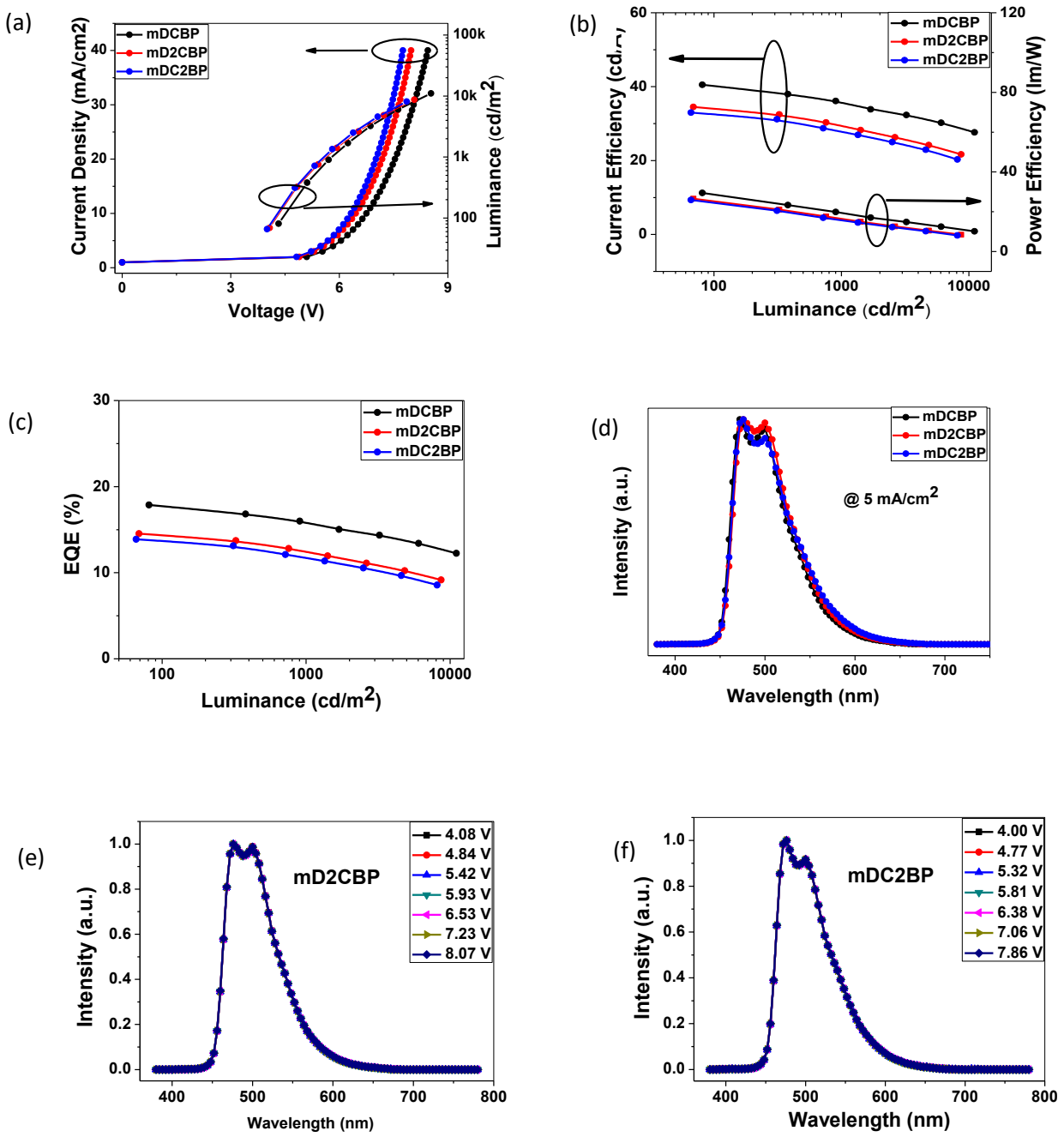

Figure 4.3.8: Device performance: (a) current density-voltage-luminance characteristics; (b) luminance-current efficiency-power efficiency characteristics; (c) luminance-EQE characteristics; (d) EL spectra at 5 mA/cm^2; (e) EL spectra of *m*D2CBP-based device at varied driving voltage; (f) EL spectra of *m*DC2BP-based device at varied driving voltage. Note: The device structure was ITO/MoO_3/TAPC/host:FIrpic/TmPyPB/Liq/Al (host= *m*DCBP, *m*D2CBP, or *m*DC2BP).

Analysis

To better understand the charge carrier injection/transport behavior in the host:FIrpic layer, the FIrpic doped hole-only device ITO/MoO_3 (3.5 nm)/TAPC (40 nm)/host:FIrpic (8 wt%, 20 nm)/TAPC (10 nm)/Al (120 nm) and electron-only device ITO/PEIE/BCP (15 nm)/host:FIrpic (8 wt%, 20 nm)/TmPyPB (40 nm)/Liq (2.5 nm)/Al (120 nm) (host =*m*DCBP, *m*D2CBP or *m*DC2BP) were fabricated. The current density-voltage characteristics are shown in Figure 4.3.9. The single carrier *m*DCBP-based device had slight lower hole current density and higher electron current density than those of single *m*D2CBP-based and *m*DC2BP-based devices. The balanced hole and electron densities in the emitting layer increased the recombination efficiency, thus improving the device performance of PhOLEDs. The enhanced charge carrier injection and transporting abilities of *m*D2CBP and *m*DC2BP also reduced the resistance of PhOLEDs, leading to low operation voltage.

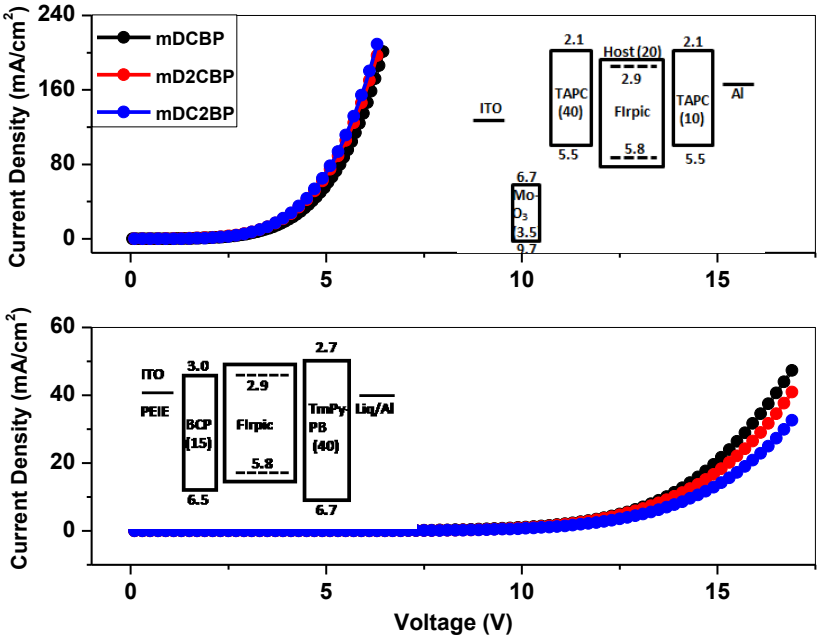

Figure 4.3.9: Current density-voltage characteristics of single-carrier-only devices.

4.3.5 TADF OLEDs characterization

Energy transfer between hosts and emitter

To confirm the applicability of these two compounds as host materials for TADF OLEDs, we investigated the photophysical properties of co-deposited thin films of 4CzIPN doped in the hosts. The films were 20 nm in thickness with FIrpic doping concentration of 6 wt% on quartz substrate. The PL spectra of doped thin film (Figure 4.3.10a) showed a maximum emission peak around 510 nm, corresponding to the $S_1 \rightarrow S_0$ transition in 4CzIPN. The emissions

from hosts were strongly suppressed in all samples, suggesting that the excitons generated in *m*D2CBP and *m*DC2BP were effectively transferred to 4CzIPN and converted into light.

To further understand the relationship between the excited states of the host and guest molecules, transient PL decays of doped thin films were measured at a wavelength of 510 nm at room temperature. As shown in Figure 4.1.10b, the transient PL decay curves of these doped thin films clearly exhibited a nano-second-scale component and a micro-second-scale component at room temperature. The former were assigned to the prompt component derived from the direct $S_1 \rightarrow S_0$ transition, which has a lifetime (τ_1) of ca. 21 ns; the latter were assigned to the TADF component resulting from the recursive $S_1 \rightarrow S_0$ transition via successive reverse intersystem conversion of the excitons from the T_1 state, which exhibited a lifetime (τ_2) that lengthened from 3.29 μs for *m*DCBP, 3.56 μs for *m*D2CBP, to 3.73 μs for *m*DC2BP. These results indicated that t*m*DC2BP and *m*D2CBP as the host can active the TADF emission of 4CzIPN.

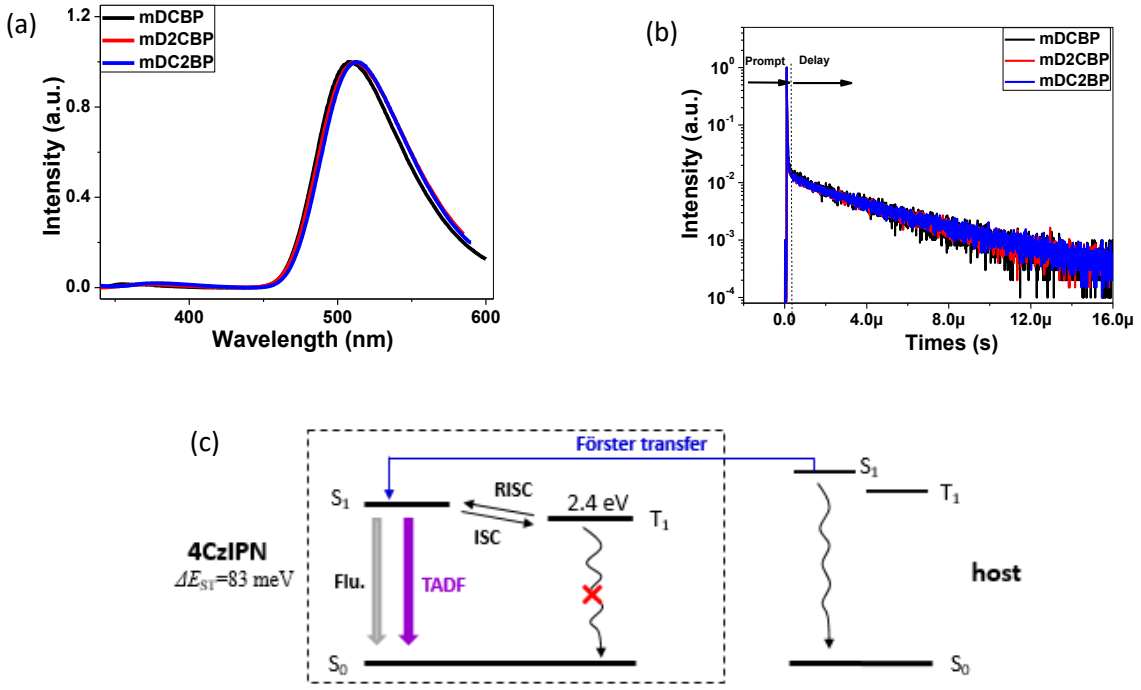

Figure 4.3.10: (a) PL spectra and (b) transient PL decay curves of doped thin films (host:4CzIPN, host =*m*DCBP, *m*D2CBP or *m*DC2BP); (c) schematic illustration of the energy transfer under light excitation.

In the hosts, singlet excitons were generated under light excitation, and then transferred to 4CzIPN through Förster transfer. In 4CzIPN, singlet excitons were also generated under light excitation. Thus, the excitons in 4CzIPN were generated in two ways: energy transfer from the

host and direct excitation by light. Of these S_1 excitons, some radiatively decayed to the ground state and those remaining were converted into T_1 excitons via intersystem crossing. The T_1 excitons were then converted into S_1 excitons via reverse intersystem crossing ($S_1 \leftarrow T_1$). Finally, the S_1 excitons radiatively decayed to the ground state. The S_1-T_1-S_1 cycle may be repeated several times before the radiatively decay of $S_1 \rightarrow S_0$ transition, leading to thermally activated delayed fluorescence emission.

Experimental

In order to evaluate the capability of *m*D2CBP and *m*DC2BP as host materials in TADF OLEDs and to reveal the influence of different carbazole to dibenzothiophene ratios on the resulting device performance, green TADF OLEDs were fabricated with the host:4CzIPN system as green emitters. The detailed device configuration was: ITO/HAT-CN (10 nm)/TAPC (40 nm)/TCTA (10 nm)/host:4CzIPN (20 nm, 6 wt%)/TmPyPB (40 nm)/Liq (2.5 nm)/Al (host= *m*DCBP, *m*D2CBP, or *m*DC2BP). The chemical structures and energy levels of the materials used in these devices are presented in Figure 4.3.11. HAT-CN and Liq were utilized as hole and electron injection layers, respectively. TAPC and TCTA were served as hole transport materials; TCTA also reduced the hole injection barrier from TAPC to the hosts. TmPyPB was served as the electron transport material. There were large energy barriers for electron leakage from the host to TCTA and for hole leakage from the host to TmPyPB, so TCTA and TmPyPB were also used as electron and hole blocking layers, respectively. The triplet energies of TCTA (E_T=2.7 eV) and TmPyPB (E_T=2.8 eV) were higher than that of 4CzIPN (2.42 eV), so TCTA and TmPyPB were chosen as the exciton blocker layer to prevent exciton diffusion, thus effectively blocking excitons within the emissive zone.

Under the electrical excitation, charge recombination in the host materials produced singlet and triplet excitons with a ratio of 1:3 (25% singlet excitons and 75% triplet excitons). The excitons generated on host materials were transferred to 4CzIPN through Förster transfer or Dexter transfer. In 4CzIPN, singlet and triplet excitons were also generated with a ratio of 1:3 by charge trapping. Excitons in 4CzIPN were thus generated in two ways: energy transfer from the host and direct recombination. In 4CzIPN, of these excitons, some decay radiatively and those remaining were converted into T_1 excitons via intersystem crossing. The T_1 excitons were converted into S_1 excitons via reverse intersystem crossing ($S_1 \leftarrow T_1$). Finally, the S_1 excitons radiatively decayed to the ground state ($S_1 \rightarrow S_0$ transition). The S_1-T_1-S_1 cycle may be repeated several times before the radiative decay of $S_1 \rightarrow S_0$, leading to thermally activated delayed fluorescence emission.

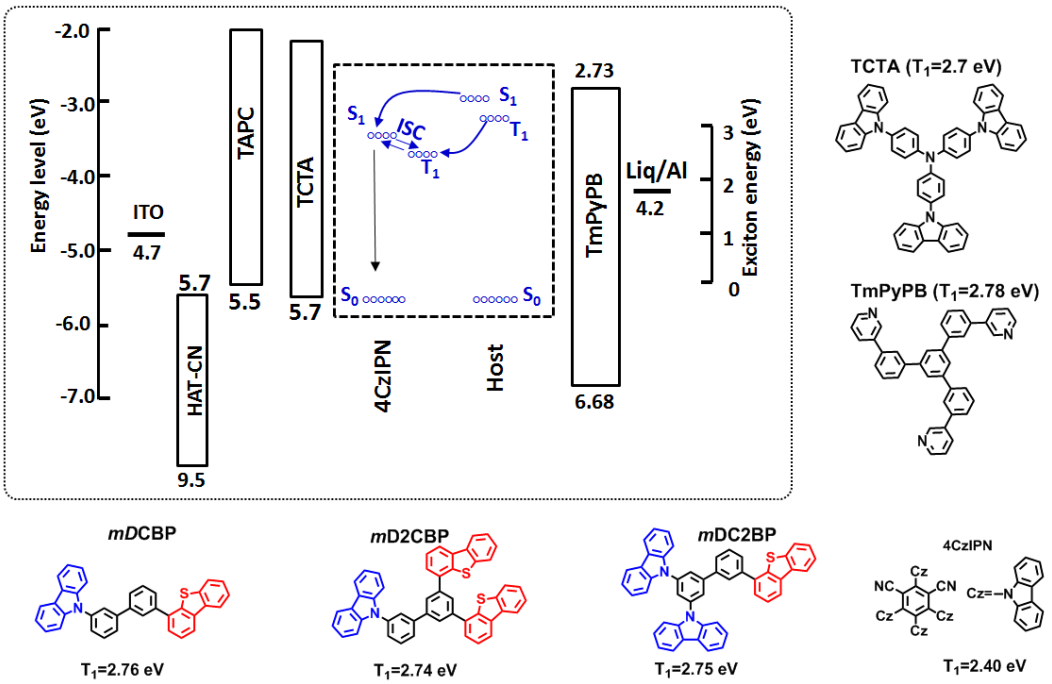

Figure 4.3.11: Energy levels and molecular structures of materials adopted in EL devices.

TADF OLEDs characterization

Figure 4.3.12a shows the current density-voltage-luminescence curves of TADF OLEDs. At the same driving voltage, the current density was highest in *m*DC2BP-based device and lowest in *m*D2CBP-based device; at low driving voltage, the luminescence was highest in *m*DC2BP-based device and lowest in *m*D2CBP-based device, and at high driving voltage, the luminescence was highest in *m*DCBP-based device. These results indicate that *m*DC2BP-based device has larger efficiency roll-off at high luminance compared to that of *m*DCBP. At 1000 cd m^{-2} for practical applications, the driving voltages was 4.37 V for *m*DC2BP-based device, lower than that of 4.90 V and 4.71 V for *m*D2CBP and *m*DCBP devices, respectively.

With carbazole and dibenzothiophene moiety mixing ration of 1: 1, *m*DCBP-based device showed the highest device efficiency. Its maximum current efficiency was 66 cd/A; the maximum power efficiency was 51.8 lm/W; and the maximum external quantum efficiency was 19.4%. These efficiency values were 61.5 cd/A, 45.1 lm/W, and 18.2% for *m*D2CBP-based device, and 60 cd/A, 50.9 lm/W and 17.7 % for *m*DC2BP, respectively. All the devices showed EL spectra with a maximum emission peak at 520 nm arising from the typical emission of the 4CzIPN. There were no other radiative emission peaks from the host or charge transport materials, indicating complete energy transfer from the host to FIrpic and excitons were well-confined within the emitting layer. The EL spectra of these devices were not changed under

increased driving voltage because the EL emission was only from the 4CzIPN. The commission International de I′Eclairage coordinates were (0.31, 0.59) and (0.32,0.59) for *m*D2CBP-based and *m*DC2BP devices, respectively. All of the aforementioned characterization data of TADF OLEDs are summarized in Table 4.3.3.

Table 4.3.3 Electroluminescence characteristics of TADF OLEDs.

Device	V^a (V)	$\eta_{ce}{}^b$ (cd A^{-1})	$\eta_{pe}{}^b$ (lm W^{-1})	$\eta_{ext}{}^b$ (%)	CIE(x, y)[c]
*m*DCBP	4.71	66.0/65.8/62.0	51.8/51.4/41.5	19.4/19.2/18.2	(0.31,0.59)
*m*D2CBP	4.90	61.5/-/58.8	45.1/-/37.4	18.2/-/17.4	(0.31,0.59)
*m*DC2BP	4.37	60/-/56.6	50.9/-/40.8	17.7/-/16.7	(0.32,0.59)

[a]: Voltage at 1000 cd m^{-2}.

[b]: Current efficiency, power efficiency, and external quantum efficiency in the order of maximum, 100 cd m^{-2}, and
at 1000 cd m^{-2}, respectively.

[c]: Commission international de I'Eclariage coordinates measured at 5 mA/cm^2.

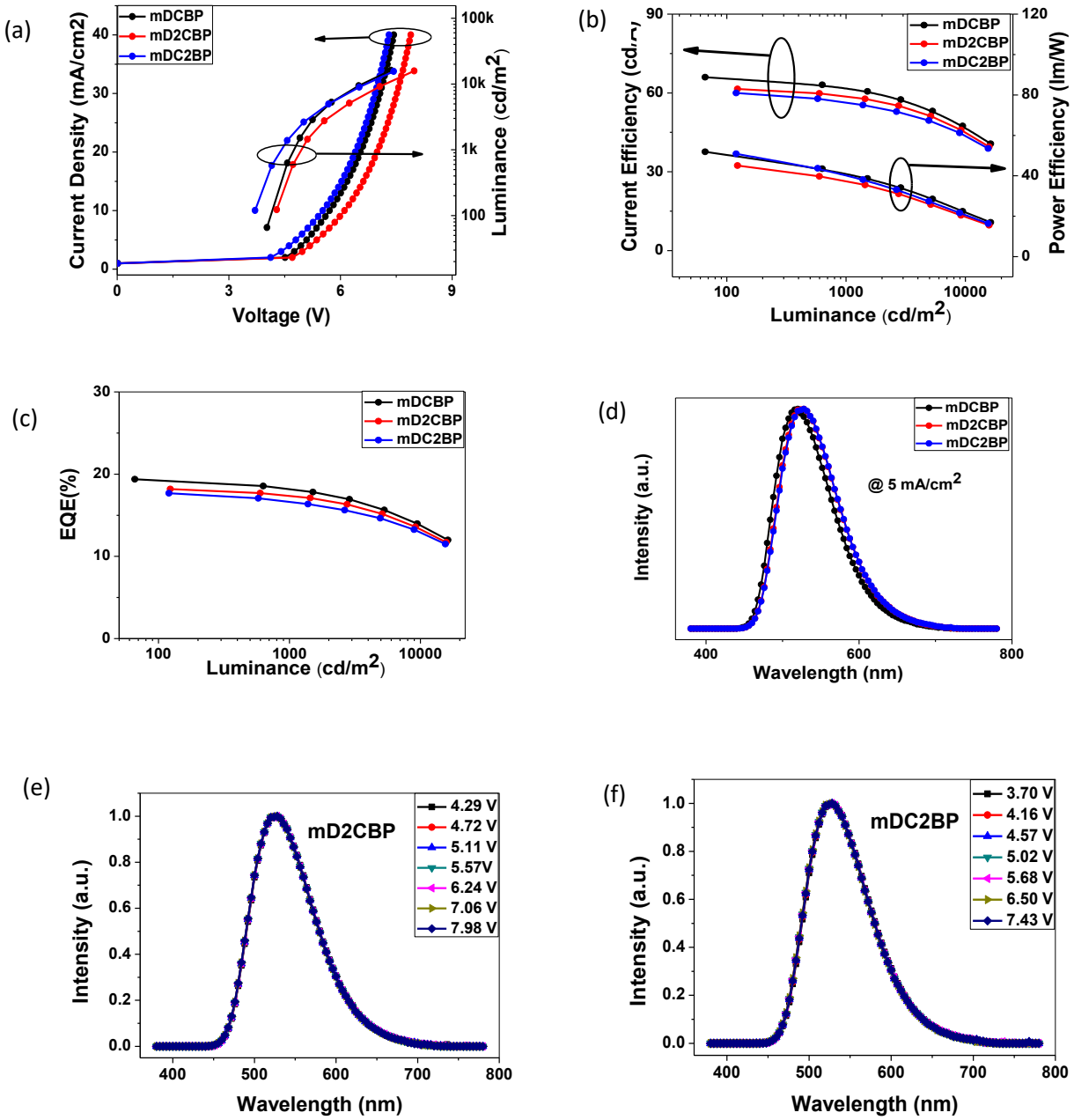

Figure 4.3.12: Device performance: (a) current density-voltage-luminance characteristics; (b) luminance-current efficiency-power efficiency characteristics; (c) luminance-EQE characteristics; and (d) EL spectra at 5 mA/cm^2; (e) EL spectra of *m*D2CBP-based device at varied driving voltage; (f) EL spectra of *m*DC2BP-based device at varied driving voltage. Note: The device structure was ITO/HAT-CN/TAPC/TCTA/host:4CzIPN/TmPyPB/Liq/Al (host= *m*DCBP, *m*D2CBP, or *m*DC2BP).

Analysis

To better understand the charge carrier injection/transport behavior in doped emitting layer, the hole- and electron-only devices with doped emitting layer were fabricated. The hole-only device structure was ITO/HAT-CN (10 nm)/TAPC (40 nm)/host:4CzIPN (20 nm, 6% wt)/TAPC (10 nm)/Al (120 nm) and the electron-only device structure was ITO/PEIE/BCP (15 nm)/host:4CzIPN (20nm, 6wt%)/TmPyPB (40 nm)/Liq (2.5 nm)/Al (120 nm) (host=*m*DCBP, *m*D2CBP or *m*DC2BP). The single-carrier *m*DCBP-based device had slightly higher electron current density than those of single-carrier *m*D2CBP-based and *m*DC2BP-based devices. The slightly balanced hole and electron densities in the emitting layer increased the recombination efficiency, thus slightly improved the device efficiency of TADF OLEDs. For the *m*DC2BP-based device, it showed the highest hole current density and lowest electron current density compared to the other two devices. The enhanced charge carrier injection and transporting abilities of *m*D2CBP reduced the resistance of the device, leading to low operation voltage; and the poor carrier balance resulted in large roll-off at high luminance.

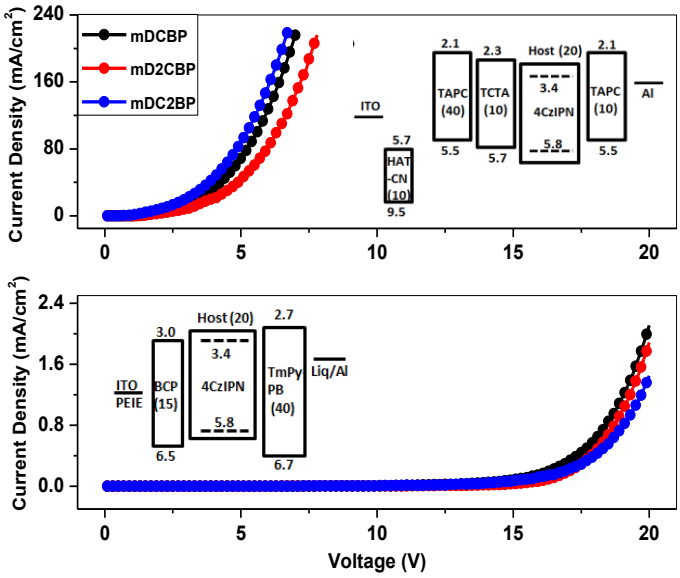

Figure 4.3.13: Current density-voltage characteristics of single-carrier-only devices.

4.3.6 Summary

The systematic study elucidating the structure-function relationship of the number and ratio of carbazole to dibenzothiophene moieties in OLEDs host materials has been carried out. Two host materials, *m*D2CBP and *m*DC2BP, with various carbazole and dibenzothiophene group ratios connected by biphenyl spacers were investigated. Their thermal, photophysical, and

electrical properties were characterized in detail. These two compounds exhibited sufficiently high triplet energies to guarantee their capability to use as hosts for blue PhOLEDs and green TADF OLEDs. The device performance of blue PhOLEDs and green TADF OLEDs based on them were detailed investigated and good performance was obtained. The best-performance of the PhOLEDs and TADF OLEDs were achieved with the host materials containing 1:1 carbazole and dibenzothiophene ratios, because of improved charge balance in OLEDs. The present study provides a valuable strategy for readily controlling the carrier injecting/transporting ability of carbazole/dibenzothiophene derivatives by adjusting the number and mixing ratio of the donor to acceptor units.

Chapter 5
Conclusion and Outlook

The aim of this study was to understand the impact of carbazole and dibenzothiophene moieties in host materials for OLEDs. In this work, seven host materials derived from carbazole and dibenzothiophene moieties with different molecular structure configurations were investigated. By systematically varying the molecular structure of carbazole/dibenzothiophene hybrids, we investigated 1) the structure-property relationships on thermal stability/physical properties (singlet/triplet energies, HOMO/LUMO)/charge carrier transport properties; 2) the bridging effects of extended linking spacers between the carbazole and dibenzothiophene moieties on thermal stability/physical properties/charge carrier transport properties; and 3) various carbazole to dibenzothiophene moiety ratios effect on thermal stability/physical properties/charge carrier transport properties.

Within this thesis, we firstly investigated a high performance host material (*m*DCBP) containing one carbazole moiety (as donor) and one dibenzothiophene moiety (as acceptor) with biphenyl as a linkage through the meta position. The physical properties were comprehensively characterized and compared to classic carbazole and dibenzothiophene analogues (*m*BPDBT and *m*CBP). The best performance both in blue PhOLEDs and green TADF OLEDs was achieved using mDCBP (with one carbazole moiety and one dibenzothiophene moiety) as host material, which showed maximum current efficiency of 40.5 cd A^{-1}, power efficiency of 29.4 lm W^{-1}, and external quantum efficiency of 17.9% in blue-FIrpic based PhOLEDs and maximum current efficiency of 66 cd A^{-1}, power efficiency of 51.8 lm W^{-1}, and external quantum efficiency of 19.4% in green-4CzIPN based TADF OLEDs, as shown in Figure 5.1. The highest reported external quantum efficiency for 4CzIPN based TADF devices was 19.3% achieved by Adachi group in 2012, and was improved to 25.7% by engineering mixed host materials in emitting layer as reported by Kido group in 2016 [12, 173].

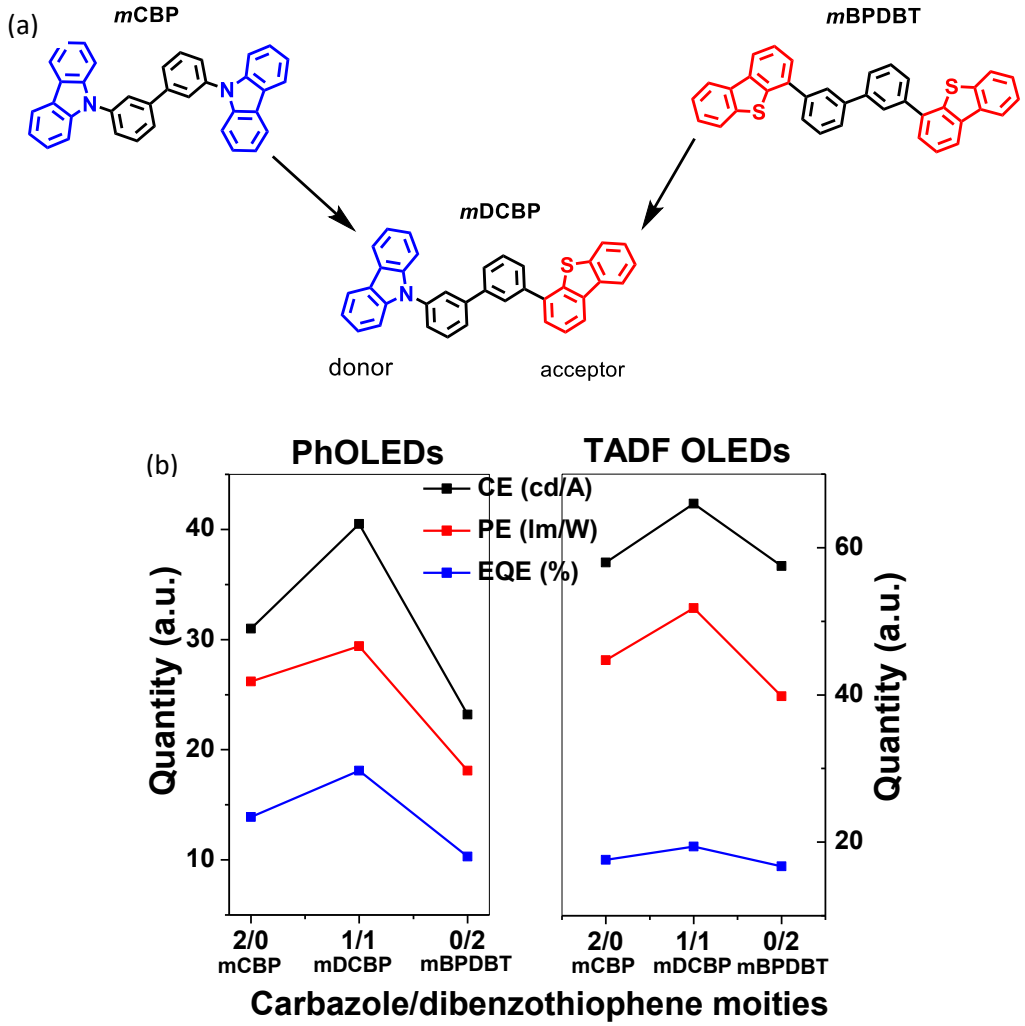

Figure 5.1: (a) Schematic illustration of first study; (b) device performance of PhOLEDs and TADF OLEDs. Note: Carbazole/dibenzothiophene moieties: carbazole/dibenzothiophene moiety numbers in carbazole/dibenzothiophene derivatives, 2/0 (*m*CBP), 1/1 (*m*DCBP), and 0/2 (*m*BPDBT).

We next investigated three carbazole/dibenzothiophene derivatives, *m*DCP with one phenyl ring, *m*DCBP with two phenyl rings, and *m*DCTP with three phenyl rings between carbazole and dibenzothiophene moieties. The manner in how the different linking spacers between carbazole and dibenzothiophene units affect the physical properties and the balance between the charge carrier transporting property were discussed in detail. We found that thermal stability was increased as the linking spacer extended. As the phenyl spacer increased, the performance of blue PhOLEDs and green TADF OLEDs slightly decreased; the best device performance was achieved with *m*DCP as host material, as shown in Figure 5.2. But *m*DCP has

a low glass transition temperature of 68 ˚C, which would reduce the device stability. So in conclusion, *m*DCBP (with biphenyl) was suggested as the best performance host material since it showed suitable thermal stability and *m*DCBP-based OLEDs exhibited similar device efficiencies with that of *m*DCP-based OLEDs.

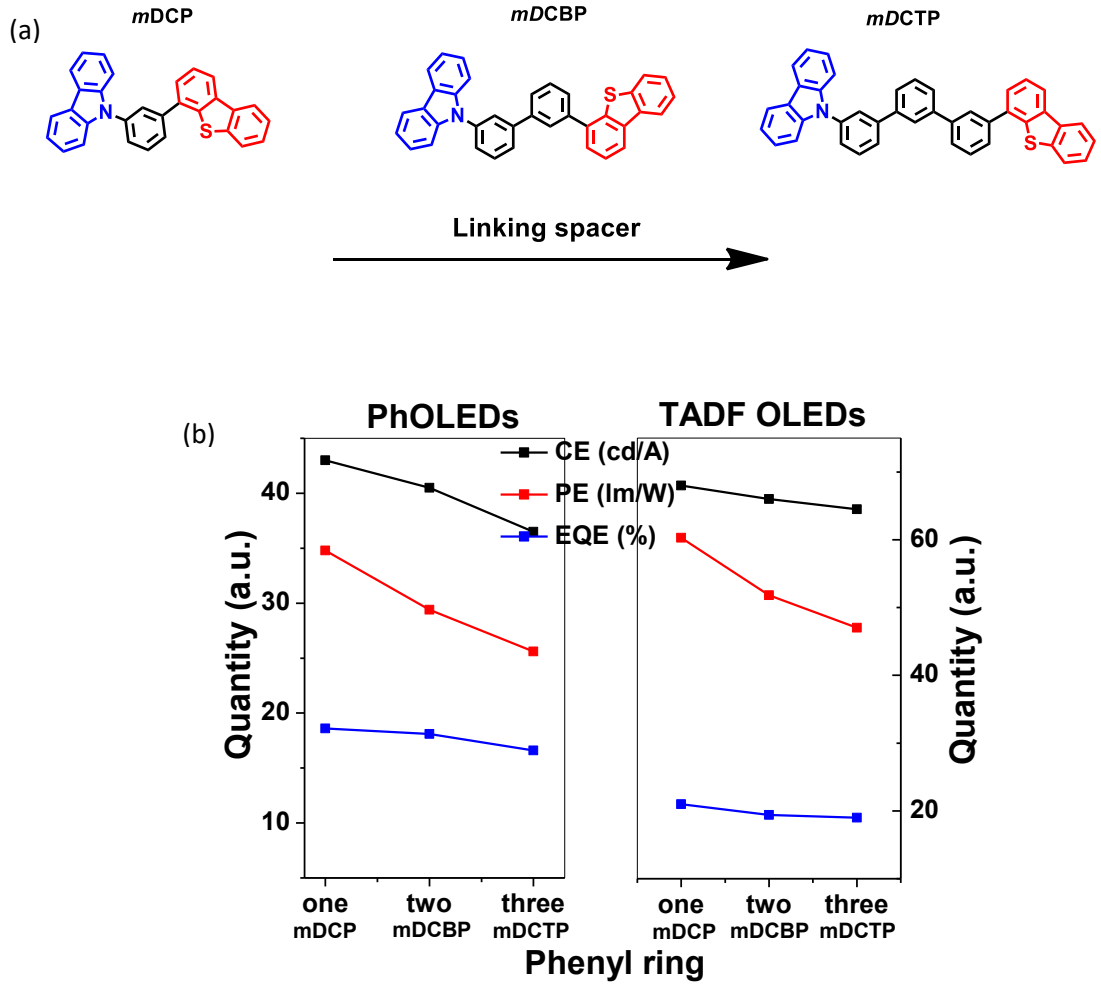

Figure 5.2: (a) Schematic illustration of second study and (b) device performance of PhOLEDs and TADF OLEDs. Note: Phenyl ring: phenyl ring numbers in carbazole/dibenzothiophene derivatives, one (*m*DCP), two (*m*DCBP), and three (*m*DCTP).

We conducted further systematic study to elucidate the molecular structure-function relationship of the number and ratio of carbazole to dibenzothiophene moieties. Three carbazole/dibenzothiophene derivatives: *m*DCBP with one carbazole and one dibenzothiophene moieties, *m*DC2BP with two carbazole and one dibenzothiophene moiety moieties, and *m*D2CBP, with one carbazole and two dibenzothiophene moieties (all connected by biphenyl spacers) were investigated. With the *m*DCBP as host materials, the best device performance of both blue PhOLEDs and green TADF OLEDs were achieved, as shown in

Figure 5.3.

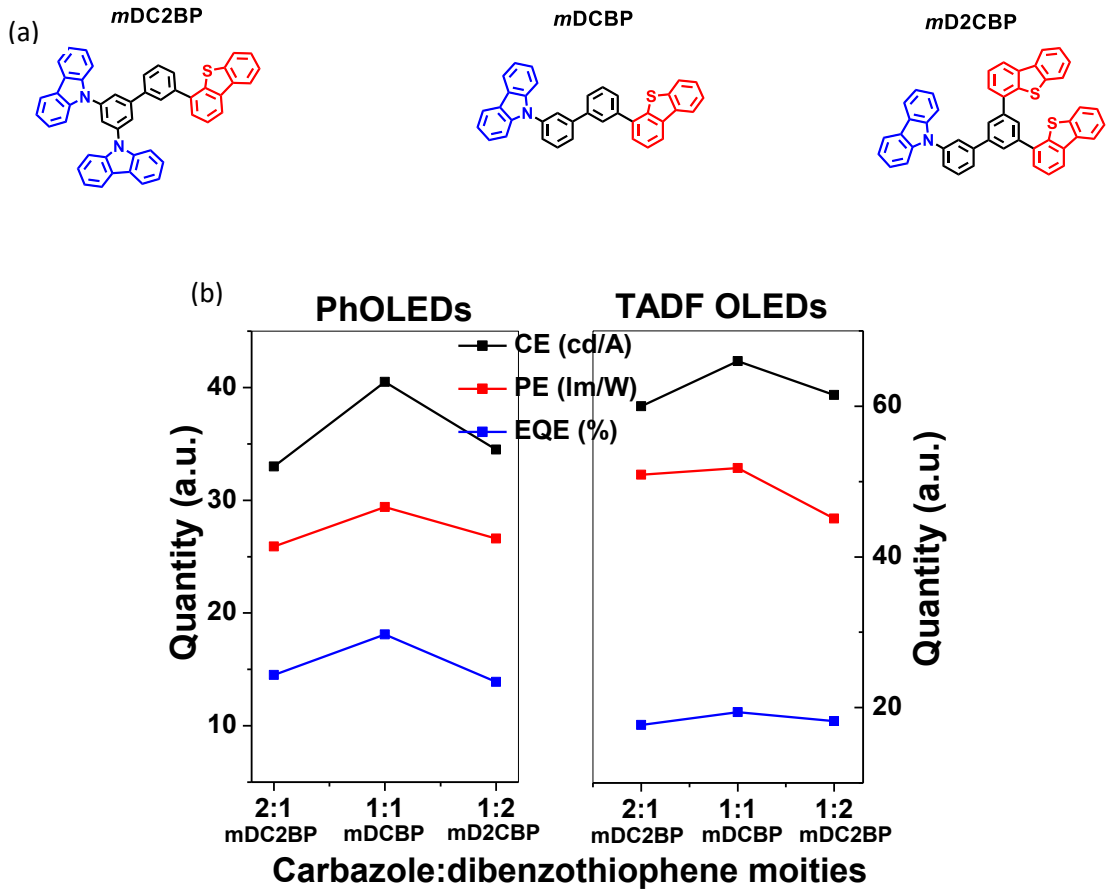

Figure 5.3: (a) Schematic illustration of third study and (b) device performance of PhOLEDs and TADF OLEDs. Note: carbazole: dibenzothiophene: the ratio of carbazole to dibenzothiophene in derivatives, 2:1 (*m*DC2BP), 1:1 (*m*DCBP), and 1:2 (*m*D2CBP).

In total, taking the thermal stability of the host materials and the device efficiencies, *m*DCBP, which has one carbazole moiety and one dibenzothiophene moiety while biphenyl was used to linkage them through *meta* position, was found to be the best choice in these carbazole/dibenzothiophene derivative.

There are a number of unresolved issues, which arose during this study that merit further research in the future.

• In this study, *m*DCP showed excellent charge carrier injection/transporting ability but a low glass transition temperature due to the low molecule weight. By changing the linking spacer with high molecular weight (e.g., diphenylsily) between donor and acceptors, the glass

transition temperature can be effectively enhanced [174].

• To improve the electron injection and transport ability, incorporation of other strong electron-withdrawing moieties (i.e., sulfonyl moiety, trifluoromethyl carbonyl moiety, and pyrazolyl moiety) could be employed to construct carbazole-based host material for high performance OLEDs [175, 176].

Bibliography

1. Bernanose, A., M. Comte, and P. Vouaux, *A New Method of Emission of Light by Certain Organic Compounds.* J. Chim. Phys, 1953. **50**: p. 64-68.
2. Pope, M., H. Kallmann, and P. Magnante, *Electroluminescence in Organic Crystals.* Journal of Chemical Physics, 1963. **38**: p. 2042-2043.
3. Tang, C.W. and S.A. VanSlyke, *Organic Electroluminescent Diodes.* Applied Physics Letters, 1987. **51**(12): p. 913-915.
4. Burroughes, J., et al., *Light-Emitting Diodes Based on Conjugated Polymers.* Nature, 1990. **347**(6293): p. 539-541.
5. Forrest, S.R., D.D. Bradley, and M.E. Thompson, *Measuring the Efficiency of Organic Light‐Emitting Devices.* Advanced Materials, 2003. **15**(13): p. 1043-1048.
6. Smith, L., J. Wasey, and W.L. Barnes, *Light Outcoupling Efficiency of Top-Emitting Organic Light-Emitting Diodes.* Applied Physics Letters, 2004. **84**(16): p. 2986-2988.
7. Saxena, K., V. Jain, and D.S. Mehta, *A Review on the Light Extraction Techniques in Organic Electroluminescent Devices.* Optical Materials, 2009. **32**(1): p. 221-233.
8. Forrest, S.R., *The Road to High Efficiency Organic Light Emitting Devices.* Organic Electronics, 2003. **4**(2): p. 45-48.
9. Jeon, S.-O., et al., *100% Internal Quantum Efficiency and Stable Efficiency Roll-Off in Phosphorescent Light-Emitting Diodes Using a High Triplet Energy Hole Transport Material.* Applied Physics Letters, 2008. **93**(6): p. 063306.
10. Fukagawa, H., et al., *Highly Efficient and Stable Red Phosphorescent Organic Light‐Emitting Diodes Using Platinum Complexes.* Advanced Materials, 2012. **24**(37): p. 5099-5103.
11. Baldo, M.A., et al., *Highly Efficient Phosphorescent Emission from Organic Electroluminescent Devices.* Nature, 1998. **395**(6698): p. 151-154.
12. Uoyama, H., et al., *Highly Efficient Organic Light-Emitting Diodes from Delayed Fluorescence.* Nature, 2012. **492**(7428): p. 234-240.
13. Adachi, C., et al., *Nearly 100% Internal Phosphorescence Efficiency in an Organic Light-Emitting Device.* Journal of Applied Physics, 2001. **90**(10): p. 5048-5051.

14. Kaji, H., et al., *Purely Organic Electroluminescent Material Realizing 100% Conversion from Electricity to Light.* Nature Communications, 2015. **6**: p. 8476.
15. Cui, L.-S., et al., *Pure Hydrocarbon Hosts for ≈100% Exciton Harvesting in Both Phosphorescent and Fluorescent Light-Emitting Devices.* Advanced Materials, 2015. **27**(28): p. 4213-4217.
16. Kawamura, Y., et al., *Intermolecular Interaction and a Concentration-Quenching Mechanism of Phosphorescent Ir (Iii) Complexes in a Solid Film.* Physical Review Letters, 2006. **96**(1): p. 017404.
17. Baldo, M.A., C. Adachi, and S.R. Forrest, *Transient Analysis of Organic Electrophosphorescence. Ii. Transient Analysis of Triplet-Triplet Annihilation.* Physical Review B, 2000. **62**(16): p. 10967.
18. Reineke, S., K. Walzer, and K. Leo, *Triplet-Exciton Quenching in Organic Phosphorescent Light-Emitting Diodes with Ir-Based Emitters.* Physical Review B, 2007. **75**(12): p. 125328.
19. Adachi, C., et al., *Endothermic Energy Transfer: A Mechanism for Generating Very Efficient High-Energy Phosphorescent Emission in Organic Materials.* Applied Physics Letters, 2001. **79**(13): p. 2082-2084.
20. Tokito, S., et al., *Confinement of Triplet Energy on Phosphorescent Molecules for Highly-Efficient Organic Blue-Light-Emitting Devices.* Applied Physics Letters, 2003. **83**(3): p. 569-571.
21. Yuan, X.-D., et al., *A Rational Design of Carbazole-Based Host Materials with Suitable Spacer Group Towards Highly-Efficient Blue Phosphorescence.* Journal of Materials Chemistry C, 2014. **2**(31): p. 6387-6394.
22. Dong, S.C., et al., *Rational Design of Dibenzothiophene-Based Host Materials for Pholeds.* Journal of Physical Chemistry C, 2014. **118**(5): p. 2375-2384.
23. Sangchart, T., et al., *Synthesis, Physical and Electroluminescence Properties of 3, 6-Dipyrenylcarbazole End Capped Oligofluorenes.* RSC Advances, 2015. **5**(34): p. 26569-26579.
24. Wang, X.D., et al., *Solution-Processible 2,2-Dimethyl-Biphenyl Cored Carbazole Dendrimers as Universal Hosts for Efficient Blue, Green, and Red Phosphorescent Oleds.* Advanced Functional Materials, 2014. **24**(22): p. 3413-3421.

25. Nishimoto, T., et al., *A Six-Carbazole-Decorated Cyclophosphazene as a Host with High Triplet Energy to Realize Efficient Delayed-Fluorescence Oleds.* Materials Horizons, 2014. **1**(2): p. 264-269.
26. Sasabe, H., et al., *3, 3′ -Bicarbazole -Based Host Materials for High -Efficiency Blue Phosphorescent Oleds with Extremely Low Driving Voltage.* Advanced Materials, 2012. **24**(24): p. 3212-3217.
27. Tsai, M.-H., et al., *3-(9-Carbazolyl) Carbazoles and 3, 6-Di (9-Carbazolyl) Carbazoles as Effective Host Materials for Efficient Blue Organic Electrophosphorescence.* Advanced Materials, 2007. **19**(6): p. 862-866.
28. Holmes, R., et al., *Blue Organic Electrophosphorescence Using Exothermic Host-Guest Energy Transfer.* Applied Physics Letters, 2003. **82**(15): p. 2422-2424.
29. Dong, S.-C., et al., *Novel Dibenzothiophene Based Host Materials Incorporating Spirobifluorene for High-Efficiency White Phosphorescent Organic Light-Emitting Diodes.* Organic Electronics, 2013. **14**(3): p. 902-908.
30. Dong, S.-C., et al., *Spiro-Annulated Triarylamine-Based Hosts Incorporating Dibenzothiophene for Highly Efficient Single-Emitting Layer White Phosphorescent Organic Light-Emitting Diodes.* Journal of Materials Chemistry C, 2013. **1**(40): p. 6575-6584.
31. Na, Y.-J., et al., *Synthesis of Dibenzothiophene-Based Host Materials and Their Blue Phosphorescent Device Performances.* Organic Electronics, 2015. **22**: p. 92-97.
32. Fan, C., et al., *Dibenzothiophene-Based Phosphine Oxide Host and Electron-Transporting Materials for Efficient Blue Thermally Activated Delayed Fluorescence Diodes through Compatibility Optimization.* Chemistry of Materials, 2015. **27**(14): p. 5131-5140.
33. Jeong, S.H. and J.Y. Lee, *Dibenzothiophene Derivatives as Host Materials for High Efficiency in Deep Blue Phosphorescent Organic Light Emitting Diodes.* Journal of Materials Chemistry, 2011. **21**(38): p. 14604-14609.
34. Brütting, W., *Physics of Organic Semiconductors*. 2006: John Wiley & Sons.
35. Carey, F.A. and R.J. Sundberg, *Advanced Organic Chemistry: Part A: Structure and Mechanisms*. 2007: Springer Science & Business Media.
36. Atkins, P. and J. De Paula, *Atkins' Physical Chemistry.* Oxford University Press, 2006.

37. Holmes, R.J., W. Brütting, and C. Adachi, *Physics of Organic Semiconductors*. 2012: John Wiley & Sons.
38. Schwoerer, M. and H.C. Wolf, *Organic Molecular Solids*. 2008: John Wiley & Sons.
39. Pope, M. and C.E. Swenberg, *Electronic Processes in Organic Crystals and Polymers*. 1999: Oxford University Press.
40. Djurovich, P.I., et al., *Measurement of the Lowest Unoccupied Molecular Orbital Energies of Molecular Organic Semiconductors.* Organic Electronics, 2009. **10**(3): p. 515-520.
41. Krause, S., et al., *Determination of Transport Levels of Organic Semiconductors by Ups and Ips.* New Journal of Physics, 2008. **10**(8): p. 085001.
42. Atkins, P.W. and R.S. Friedman, *Molecular Quantum Mechanics*. 2011: Oxford university press.
43. Lichtman, J.W. and J.-A. Conchello, *Fluorescence Microscopy.* Nature methods, 2005. **2**(12): p. 910-919.
44. Valeur, B. and M.N. Berberan-Santos, *Molecular Fluorescence: Principles and Applications*. 2012: John Wiley & Sons.
45. Joseph, R.L. and R. Lakowicz, *Principles of Fluorescence Spectroscopy*. 1999, Kluwer Academic/Plenum Publishers.
46. Turro, N.J., *Modern Molecular Photochemistry*. 1991: University Science Books.
47. Farchioni, R. and G. Grosso, *Organic Electronic Materials: Conjugated Polymers and Low Molecular Weight Organic Solids*. Vol. 41. 2013: Springer Science & Business Media.
48. Klessinger, M. and J. Michl, *Excited States and Photochemistry of Organic Molecules*. 1995: Wiley-VCH.
49. Sternlicht, H., G. Nieman, and G. Robinson, *Triplet—Triplet Annihilation and Delayed Fluorescence in Molecular Aggregates.* The Journal of Chemical Physics, 1963. **38**(6): p. 1326-1335.
50. Luo, Y. and H. Aziz, *Correlation between Triplet‐Triplet Annihilation and Electroluminescence Efficiency in Doped Fluorescent Organic Light‐Emitting Devices.* Advanced Functional Materials, 2010. **20**(8): p. 1285-1293.
51. Zhang, Y. and S.R. Forrest, *Triplets Contribute to Both an Increase and Loss in Fluorescent Yield in Organic Light Emitting Diodes.* Physical review letters, 2012. **108**(26): p. 267404.

52. Adachi, C., *Third-Generation Organic Electroluminescence Materials.* Japanese Journal of Applied Physics, 2014. **53**(6): p. 060101.
53. Förster, T., *Transfer Mechanisms of Electronic Excitation Energy.* Radiation Research Supplement, 1960: p. 326-339.
54. Dexter, D.L., *A Theory of Sensitized Luminescence in Solids.* The Journal of Chemical Physics, 1953. **21**(5): p. 836-850.
55. Arkhipov, V., E. Emelianova, and H. Baessler, *Quenching of Excitons in Doped Disordered Organic Semiconductors.* Physical Review B, 2004. **70**(20): p. 205205.
56. Baldo, M., et al., *Excitonic Singlet-Triplet Ratio in a Semiconducting Organic Thin Film.* Physical Review B, 1999. **60**(20): p. 14422.
57. Vincett, P., et al., *Electrical Conduction and Low Voltage Blue Electroluminescence in Vacuum-Deposited Organic Films.* Thin Solid Films, 1982. **94**(2): p. 171-183.
58. Tang, C. and S. VanSlyke, *Organic Electroluminescent Diodes.* Applied Physics Letters, 1987. **51**(12): p. 913-915.
59. Burroughes, J., et al., *Light-Emitting Diodes Based on Conjugated Polymers.* Nature, 1990. **347**(6293): p. 539-541.
60. Kido, J., M. Kimura, and K. Nagai, *Multilayer White Light-Emitting Organic Electroluminescent Device.* Science, 1995. **267**(5202): p. 1332-1334.
61. Fukuda, Y., et al. *Organic Led Full Color Passive ‐Matrix Display*. in *SID Symposium Digest of Technical Papers*. 1999. Wiley Online Library.
62. Kido, J., *Organic Displays.* Physics World, 1999. **12**(3): p. 27-29.
63. Oh, C.H., et al. *21.1: Invited Paper: Technological Progress and Commercialization of Oled Tv*. in *SID Symposium Digest of Technical Papers*. 2013. Wiley Online Library.
64. Sarma, K. *Recent Progress in Oled and Flexible Displays and Their Potential for Application to Aerospace and Military Display Systems*. in *Display Technologies and Applications for Defense, Security, and Avionics IX; and Head- and Helmet-Mounted Displays XX*. 2015. International Society for Optics and Photonics.
65. Bown, M., et al. *Recent Progress in High Efficiency Blue Emitter Materials for Oleds-Development of Phosphorescent and Tadf Materials*. in *Solid-State and Organic Lighting*. 2014. Optical Society of America.

66. Shin, H.J., et al. *50.1: Invited Paper: Technological Progress of Panel Design and Compensation Methods for Large‐Size Uhd Oled Tvs*. in *SID Symposium Digest of Technical Papers*. 2014. Wiley Online Library.
67. Kahn, A., *Fermi Level, Work Function and Vacuum Level.* Materials Horizons, 2016. **3**(1): p. 7-10.
68. Kahn, A., N. Koch, and W. Gao, *Electronic Structure and Electrical Properties of Interfaces between Metals and Π‐Conjugated Molecular Films.* Journal of Polymer Science Part B: Polymer Physics, 2003. **41**(21): p. 2529-2548.
69. Koch, N., *Organic Electronic Devices and Their Functional Interfaces.* ChemPhysChem, 2007. **8**(10): p. 1438-1455.
70. Oehzelt, M., et al., *Energy-Level Alignment at Organic Heterointerfaces.* Science Advances, 2015. **1**(10): p. e1501127.
71. Silveira, W.R. and J.A. Marohn, *Microscopic View of Charge Injection in an Organic Semiconductor.* Physical review letters, 2004. **93**(11): p. 116104.
72. Braun, D., *Electronic Injection and Conduction Processes for Polymer Devices.* Journal of Polymer Science Part B: Polymer Physics, 2003. **41**(21): p. 2622-2629.
73. Scott, J.C. and G.G. Malliaras, *Charge Injection and Recombination at the Metal–Organic Interface.* Chemical Physics Letters, 1999. **299**(2): p. 115-119.
74. Conwell, E.M. and M.W. Wu, *Contact Injection into Polymer Light-Emitting Diodes.* Applied Physics Letters, 1997. **70**(14): p. 1867-1869.
75. Destruel, P., et al., *Influence of Indium Tin Oxide Treatment Using Uv–Ozone and Argon Plasma on the Photovoltaic Parameters of Devices Based on Organic Discotic Materials.* Polymer International, 2006. **55**(6): p. 601-607.
76. Koch, N., et al., *Photoemission Spectroscopic Investigation on the Interface Formation of a Ladder-Type Poly(Para-Phenylene) with Aluminum.* Applied Physics Letters, 2000. **76**(25): p. 3738-3740.
77. Nakayama, Y., et al., *Origins of Improved Hole‐Injection Efficiency by the Deposition of Moo3 on the Polymeric Semiconductor Poly (Dioctylfluorene‐Alt‐Benzothiadiazole).* Advanced Functional Materials, 2009. **19**(23): p. 3746-3752.
78. Kim, Y.-K., J. Won Kim, and Y. Park, *Energy Level Alignment at a Charge Generation Interface between 4,4′-Bis(N-Phenyl-1-Naphthylamino)Biphenyl and 1,4,5,8,9,11-Hexaazatriphenylene-Hexacarbonitrile.* Applied Physics Letters, 2009. **94**(6): p. 063305.

79. Lee, H., et al., *The Origin of the Hole Injection Improvements at Indium Tin Oxide/Molybdenum Trioxide/N, N'-Bis (1-Naphthyl)-N, N'-Diphenyl-1, 1'-Biphen-Yl-4, 4'-Diamine Interfaces.* Applied Physics Letters, 2008. **93**(4): p. 43308.
80. Kim, Y.-K., J.W. Kim, and Y. Park, *Energy Level Alignment at a Charge Generation Interface between 4, 4′ -Bis (N-Phenyl-1-Naphthylamino) Biphenyl and 1, 4, 5, 8, 9, 11-Hexaazatriphenylene-Hexacarbonitrile.* Applied Physics Letters, 2009. **94**(6): p. 063305.
81. Wu, C., et al., *Surface Modification of Indium Tin Oxide by Plasma Treatment: An Effective Method to Improve the Efficiency, Brightness, and Reliability of Organic Light Emitting Devices.* Applied Physics Letters, 1997. **70**(11): p. 1348-1350.
82. Besbes, S., et al., *Effect of Surface Treatment and Functionalization on the Ito Properties for Oleds.* Materials Science and Engineering: C, 2006. **26**(2): p. 505-510.
83. Endo, J., T. Matsumoto, and J. Kido, *Organic Electroluminescent Devices Having Metal Complexes as Cathode Interface Layer.* Japanese Journal of Applied Physics, 2002. **41**(7A): p. L800.
84. Bässler, H., *Charge Transport in Disordered Organic Photoconductors.* Phys. Status Solidi b, 1993. **175**(1): p. 15-56.
85. Brütting, W., S. Berleb, and A.G. Mückl, *Device Physics of Organic Light-Emitting Diodes Based on Molecular Materials.* Organic Electronics, 2001. **2**(1): p. 1-36.
86. Lampert, M.A. and P. Mark, *Current Injection in Solids*. 1970: Academic Press.
87. Lampert, M.A. and P. Mark, *Current Injection in Solids.* 1970.
88. Shen, Y., et al., *How to Make Ohmic Contacts to Organic Semiconductors.* ChemPhysChem, 2004. **5**(1): p. 16-25.
89. Langevin, P., *Recombinaison Et Mobilites Des Ions Dans Les Gaz.* Ann. Chim. Phys, 1903. **28**(433): p. 122.
90. Blom, P., M. De Jong, and S. Breedijk, *Temperature Dependent Electron-Hole Recombination in Polymer Light-Emitting Diodes.* Applied Physics Letters, 1997. **71**(7): p. 930-932.
91. Kim, B.S. and J.Y. Lee, *Engineering of Mixed Host for High External Quantum Efficiency above 25% in Green Thermally Activated Delayed Fluorescence Device.* Advanced Functional Materials, 2014. **24**(25): p. 3970-3977.

92. Tsutsui, T. and S. Saito, *Organic Multilayer-Dye Electroluminescent Diodes—Is There Any Difference with Polymer Led?*, in *Intrinsically Conducting Polymers: An Emerging Technology*. 1993, Springer.
93. Wilson, J., et al., *Spin-Dependent Exciton Formation in Π-Conjugated Compounds.* Nature, 2001. **413**(6858): p. 828-831.
94. Rothberg, L.J. and A.J. Lovinger, *Status of and Prospects for Organic Electroluminescence.* Journal of Materials Research, 1996. **11**(12): p. 3174-3187.
95. Kim, S.H., J. Jang, and J.Y. Lee, *High Efficiency Phosphorescent Organic Light-Emitting Diodes Using Carbazole-Type Triplet Exciton Blocking Layer.* Applied Physics Letters, 2007. **90**(22): p. 223505.
96. Su, S.-J., et al., *Pyridine-Containing Bipolar Host Materials for Highly Efficient Blue Phosphorescent Oleds.* Chemistry of Materials, 2008. **20**(5): p. 1691-1693.
97. Kessler, F., et al., *High-Performance Pure Blue Phosphorescent Oled Using a Novel Bis-Heteroleptic Iridium (Iii) Complex with Fluorinated Bipyridyl Ligands.* Journal of Materials Chemistry C, 2013. **1**(6): p. 1070-1075.
98. Liu, H., et al., *A Highly Efficient, Blue-Phosphorescent Device Based on a Wide-Bandgap Host/Firpic: Rational Design of the Carbazole and Phosphine Oxide Moieties on Tetraphenylsilane.* Advanced Functional Materials, 2012. **22**(13): p. 2830-2836.
99. Wang, Q., et al., *Harvesting Excitons Via Two Parallel Channels for Efficient White Organic Leds with Nearly 100% Internal Quantum Efficiency: Fabrication and Emission‐Mechanism Analysis.* Advanced Functional Materials, 2009. **19**(1): p. 84-95.
100. Xiao, L., et al., *Nearly 100% Internal Quantum Efficiency in an Organic Blue‐Light Electrophosphorescent Device Using a Weak Electron Transporting Material with a Wide Energy Gap.* Advanced Materials, 2009. **21**(12): p. 1271-1274.
101. Adachi, C., et al., *High-Efficiency Red Electrophosphorescence Devices.* Applied Physics Letters, 2001. **78**(11): p. 1622-1624.
102. Lamansky, S., et al., *Highly Phosphorescent Bis-Cyclometalated Iridium Complexes: Synthesis, Photophysical Characterization, and Use in Organic Light Emitting Diodes.* Journal of the American Chemical Society, 2001. **123**(18): p. 4304-4312.

103. Xie, H.Z., et al., *Reduction of Self‐Quenching Effect in Organic Electrophosphorescence Emitting Devices Via the Use of Sterically Hindered Spacers in Phosphorescence Molecules.* Advanced Materials, 2001. **13**(16): p. 1245-1248.
104. Liu, T.-H. and C.H. Chen, *Organic Light-Emitting Devices Based on a Highly Robust Osmium (Ii) Complex.* Journal of Applied Physics, 2006. **100**(9).
105. Xiao, L., et al., *Recent Progresses on Materials for Electrophosphorescent Organic Light‐Emitting Devices.* Advanced Materials, 2011. **23**(8): p. 926-952.
106. Evans, R.C., P. Douglas, and C.J. Winscom, *Coordination Complexes Exhibiting Room-Temperature Phosphorescence: Evaluation of Their Suitability as Triplet Emitters in Organic Light Emitting Diodes.* Coordination Chemistry Reviews, 2006. **250**(15): p. 2093-2126.
107. Köhler, A., J.S. Wilson, and R.H. Friend, *Fluorescence and Phosphorescence in Organic Materials.* Advanced Engineering Materials, 2002. **4**(7): p. 453.
108. Endo, A., et al., *Efficient up-Conversion of Triplet Excitons into a Singlet State and Its Application for Organic Light Emitting Diodes.* Applied Physics Letters, 2011: p. 083302.
109. Endo, A., et al., *Thermally Activated Delayed Fluorescence from Sn4+–Porphyrin Complexes and Their Application to Organic Light Emitting Diodes—a Novel Mechanism for Electroluminescence.* Advanced Materials, 2009. **21**(47): p. 4802-4806.
110. Berberan-Santos, M.N. and J.M. Garcia, *Unusually Strong Delayed Fluorescence of C70.* Journal of the American Chemical Society, 1996. **118**(39): p. 9391-9394.
111. Berberan-Santos, M. and J. Martinho, *A Linear Response Approach to Kinetics with Time-Dependent Rate Coefficients.* Chemical Physics, 1992. **164**(2): p. 259-269.
112. Baleizão, C. and M.N. Berberan-Santos, *Thermally Activated Delayed Fluorescence as a Cycling Process between Excited Singlet and Triplet States: Application to the Fullerenes.* The Journal of Chemical Physics, 2007. **126**(20): p. 204510.
113. Tanaka, F., M. Okamoto, and S. Hirayama, *Pressure and Temperature Dependences of the Rate Constant for S1-T2 Intersystem Crossing of Anthracene Compounds in Solution.* The Journal of Physical Chemistry, 1995. **99**(2): p. 525-530.
114. BALEIZao, C. and M.N. Berberan‐Santos, *Thermally Activated Delayed Fluorescence in Fullerenes.* Annals of the New York Academy of Sciences, 2008. **1130**(1): p. 224-234.

115. Nakagawa, T., et al., *Electroluminescence Based on Thermally Activated Delayed Fluorescence Generated by a Spirobifluorene Donor–Acceptor Structure.* Chemical Communications, 2012. **48**(77): p. 9580-9582.
116. Reineke, S., et al., *Reduced Efficiency Roll-Off in Phosphorescent Organic Light Emitting Diodes by Suppression of Triplet-Triplet Annihilation.* Applied Physics Letters, 2007. **91**(12): p. 123508.
117. Jeon, W.S., et al., *Ideal Host and Guest System in Phosphorescent Oleds.* Organic Electronics, 2009. **10**(2): p. 240-246.
118. Yimer, Y., P. Bobbert, and R. Coehoorn, *Charge Transport in Disordered Organic Host? Guest Systems: Effects of Carrier Density and Electric Field.* Journal of Physics: Condensed Matter, 2008. **20**(33): p. 335204.
119. Divayana, Y. and X. Sun, *Observation of Excitonic Quenching by Long-Range Dipole-Dipole Interaction in Sequentially Doped Organic Phosphorescent Host-Guest System.* Physical Review Letters, 2007. **99**(14): p. 143003.
120. Lehnhardt, M., et al., *Room Temperature Lifetime of Triplet Excitons in Fluorescent Host/Guest Systems.* Organic Electronics, 2011. **12**(3): p. 486-491.
121. Liu, P., et al., *Energy Transfer in Phosphorescent Dye Doped Polymer Thin Films.* Journal of the Korean Physical Society, 2005. **46**: p. S66-S69.
122. Baldo, M., M. Thompson, and S. Forrest, *High-Efficiency Fluorescent Organic Light-Emitting Devices Using a Phosphorescent Sensitizer.* Nature, 2000. **403**(6771): p. 750-753.
123. Yook, K.S. and J.Y. Lee, *Organic Materials for Deep Blue Phosphorescent Organic Light‐Emitting Diodes.* Advanced Materials, 2012. **24**(24): p. 3169-3190.
124. Tanaka, I., Y. Tabata, and S. Tokito, *Energy-Transfer and Light-Emission Mechanism of Blue Phosphorescent Molecules in Guest-Host Systems.* Chemical Physics Letters, 2004. **400**(1): p. 86-89.
125. Biswas, S., O. Shalev, and M. Shtein, *Thin-Film Growth and Patterning Techniques for Small Molecular Organic Compounds Used in Optoelectronic Device Applications.* Annual Review of Chemical and Biomolecular Engineering, 2013. **4**: p. 289-317.
126. Hall, D.B., P. Underhill, and J.M. Torkelson, *Spin Coating of Thin and Ultrathin Polymer Films.* Polymer Engineering and Science, 1998. **38**(12): p. 2039-2045.

127. Schubert, D.W. and T. Dunkel, *Spin Coating from a Molecular Point of View: Its Concentration Regimes, Influence of Molar Mass and Distribution.* Materials Research Innovations, 2003. **7**(5): p. 314-321.
128. Kyaw, A.K.K., et al., *Efficient Solution‐Processed Small‐Molecule Solar Cells with Inverted Structure.* Advanced Materials, 2013. **25**(17): p. 2397-2402.
129. Steinmann, W., et al., *Thermal Analysis of Phase Transitions and Crystallization in Polymeric Fibers*. 2013: INTECH Open Access Publisher.
130. Gallagher, P.K., M.E. Brown, and R.B. Kemp, *Handbook of Thermal Analysis and Calorimetry*. 1998: Elsevier.
131. Coats, A. and J. Redfern, *Thermogravimetric Analysis. A Review.* Analyst, 1963. **88**(1053): p. 906-924.
132. Shinde, K.N., et al., *Phosphate Phosphors for Solid-State Lighting*. 2012: Springer Science & Business Media.
133. Gfroerer, T.H., *Photoluminescence in Analysis of Surfaces and Interfaces.* Encyclopedia of Analytical Chemistry, 2000.
134. Swinehart, D., *The Beer-Lambert Law.* Journal of chemical education, 1962. **39**(7): p. 333.
135. Ishii, H., et al., *Energy Level Alignment and Interfacial Electronic Structures at Organic/Metal and Organic/Organic Interfaces.* Advanced Materials, 1999. **11**(8): p. 605-625.
136. Braun, S., W.R. Salaneck, and M. Fahlman, *Energy-Level Alignment at Organic/Metal and Organic/Organic Interfaces.* Adv. Mater, 2009. **21**(14-15): p. 1450-1472.
137. Einstein, A., *ber Einem Die Erzeugung Und Verwandlung Des Lichtes Betreffenden Heuristischen Gesichtspunkt.* Annalen der Physik, 1905. **4**.
138. Suga, S. and A. Sekiyama, *Photoelectron Spectroscopy: Bulk and Surface Electronic Structures*. 2013: Springer.
139. Hansson, G.V. and R.I. Uhrberg, *Photoelectron Spectroscopy of Surface States on Semiconductor Surfaces.* Surface Science Reports, 1988. **9**(5): p. 197-292.
140. Fadley, C.S., *X-Ray Photoelectron Spectroscopy: From Origins to Future Directions.* Nuclear Instruments and Methods in Physics Research Section A: Accelerators, Spectrometers, Detectors and Associated Equipment, 2009. **601**(1): p. 8-31.

141. Tanaka, I. and S. Tokito, *Precise Measurement of External Quantum Efficiency of Organic Light-Emitting Devices.* Japanese Journal of Applied Physics, 2004. **43**(11A): p. 7733-7736.
142. Lin, H.-W., et al., *Solution-Processed Hexaazatriphenylene Hexacarbonitrile as a Universal Hole-Injection Layer for Organic Light-Emitting Diodes.* Organic Electronics, 2013. **14**(4): p. 1204-1210.
143. Kroger, M., et al., *Role of the Deep-Lying Electronic States of Moo3 in the Enhancement of Hole-Injection in Organic Thin Films.* Applied Physics Letters, 2009. **95**(12): p. 123301.
144. Zhou, Y., et al., *A Universal Method to Produce Low–Work Function Electrodes for Organic Electronics.* Science, 2012. **336**(6079): p. 327-332.
145. Lee, Y., et al., *Interface Studies of Aluminum, 8-Hydroxyquinolatolithium (Liq) and Alq 3 for Inverted Oled Application.* Organic Electronics, 2008. **9**(3): p. 407-412.
146. Zheng, X., et al., *Efficiency Improvement of Organic Light-Emitting Diodes Using 8-Hydroxy-Quinolinato Lithium as an Electron Injection Layer.* Thin Solid Films, 2005. **478**(1): p. 252-255.
147. Goushi, K., et al., *Triplet Exciton Confinement and Unconfinement by Adjacent Hole-Transport Layers.* Journal of Applied Physics, 2004. **95**(12): p. 7798-7802.
148. Reineke, S., et al., *White Organic Light-Emitting Diodes with Fluorescent Tube Efficiency.* Nature, 2009. **459**(7244): p. 234-238.
149. Su, S.J., et al., *Pyridine‐Containing Triphenylbenzene Derivatives with High Electron Mobility for Highly Efficient Phosphorescent Oleds.* Advanced Materials, 2008. **20**(11): p. 2125-2130.
150. Furukawa, T., et al., *Dual Enhancement of Electroluminescence Efficiency and Operational Stability by Rapid Upconversion of Triplet Excitons in Oleds.* Scientific Reports, 2015. **5**: p. 8429.
151. Zhang, Q., et al., *Efficient Blue Organic Light-Emitting Diodes Employing Thermally Activated Delayed Fluorescence.* Nature Photonics, 2014. **8**(4): p. 326-332.
152. Lee, S.Y., et al., *High-Efficiency Organic Light-Emitting Diodes Utilizing Thermally Activated Delayed Fluorescence from Triazine-Based Donor–Acceptor Hybrid Molecules.* Applied Physics Letters, 2012. **101**(9): p. 093306.

153. Nakanotani, H., et al., *Promising Operational Stability of High-Efficiency Organic Light-Emitting Diodes Based on Thermally Activated Delayed Fluorescence.* Scientific Reports, 2013. **3**: p. 2127.
154. Frisch, M.J., et al., *Gaussian 09, Revision A. 1.* Gaussian Inc., Wallingford, CT, 2009.
155. Lin, M.-S., et al., *Incorporation of a Cn Group into Mcp: A New Bipolar Host Material for Highly Efficient Blue and White Electrophosphorescent Devices.* Journal of Materials Chemistry, 2012. **22**(31): p. 16114-16120.
156. Kim, M. and J.Y. Lee, *Engineering the Substitution Position of Diphenylphosphine Oxide at Carbazole for Thermal Stability and High External Quantum Efficiency above 30% in Blue Phosphorescent Organic Light‐Emitting Diodes.* Advanced Functional Materials, 2014. **24**(26): p. 4164-4169.
157. Tsuboi, T., et al., *Photoluminescence Characteristics of Blue Phosphorescent Ir 3+-Compounds Firpic and Firn4 Doped in Mcp and Simcp.* Optical Materials, 2008. **31**(2): p. 366-371.
158. Tsuboi, T., et al., *Energy Transfer between Organic Fluorescent Cbp Host and Blue Phosphorescent Firpic and Firn4 Guests.* Optical Materials, 2007. **29**(11): p. 1299-1304.
159. Sun, J.W., et al., *A Fluorescent Organic Light‐Emitting Diode with 30% External Quantum Efficiency.* Advanced Materials, 2014. **26**(32): p. 5684-5688.
160. Chu, T.-Y. and O.-K. Song, *Hole Mobility of N, N'-Bis (Naphthalen-1-Yl)-N, N'-Bis (Phenyl) Benzidine Investigated by Using Space-Charge-Limited Currents.* Applied Physics Letters, 2007. **90**(20): p. 203512-203512.
161. Wang, Q., et al., *Manipulating Charges and Excitons within a Single‐Host System to Accomplish Efficiency/Cri/Color‐Stability Trade‐Off for High‐Performance Owleds.* Advanced Materials, 2009. **21**(23): p. 2397-2401.
162. Su, S.-J., C. Cai, and J. Kido, *Three-Carbazole-Armed Host Materials with Various Cores for Rgb Phosphorescent Organic Light-Emitting Diodes.* Journal of Materials Chemistry, 2012. **22**(8): p. 3447-3456.
163. Lee, J., et al., *Stable Efficiency Roll-Off in Blue Phosphorescent Organic Light-Emitting Diodes by Host Layer Engineering.* Organic Electronics, 2009. **10**(8): p. 1529-1533.

164. Kang, J.-W., et al., *Low Roll-Off of Efficiency at High Current Density in Phosphorescent Organic Light Emitting Diodes.* Applied Physics Letters, 2007. **90**(22): p. 223508.
165. Cui, L.-S., et al., *Meta-Linked Spirobifluorene/Phosphine Oxide Hybrids as Host Materials for Deep Blue Phosphorescent Organic Light-Emitting Diodes.* Organic Electronics, 2013. **14**(7): p. 1924-1930.
166. Chopra, N., et al., *Effect of the Charge Balance on High-Efficiency Blue-Phosphorescent Organic Light-Emitting Diodes.* ACS Applied Materials & Interfaces, 2009. **1**(6): p. 1169-1172.
167. Fan, Z., et al., *Tuning Charge Balance in Solution Processable Bipolar Triphenylamine-Diazafluorene Host Materials for Phosphorescent Devices.* ACS applied materials & interfaces, 2015. **7**(18): p. 9445-9452.
168. Chaskar, A., H.F. Chen, and K.T. Wong, *Bipolar Host Materials: A Chemical Approach for Highly Efficient Electrophosphorescent Devices.* Advanced Materials, 2011. **23**(34): p. 3876-3895.
169. Duan, L., et al., *Strategies to Design Bipolar Small Molecules for Oleds: Donor‐Acceptor Structure and Non‐Donor‐Acceptor Structure.* Advanced Materials, 2011. **23**(9): p. 1137-1144.
170. Pan, B., et al., *A Simple Carbazole-N-Benzimidazole Bipolar Host Material for Highly Efficient Blue and Single Layer White Phosphorescent Organic Light-Emitting Diodes.* Journal of Materials Chemistry C, 2014. **2**(14): p. 2466-2469.
171. Zhang, D., et al., *Towards High Efficiency and Low Roll‐Off Orange Electrophosphorescent Devices by Fine Tuning Singlet and Triplet Energies of Bipolar Hosts Based on Indolocarbazole/1, 3, 5‐Triazine Hybrids.* Advanced Functional Materials, 2014. **24**(23): p. 3551-3561.
172. Ban, X., et al., *Bipolar Host with Multielectron Transport Benzimidazole Units for Low Operating Voltage and High Power Efficiency Solution-Processed Phosphorescent Oleds.* ACS Applied Materials & Interfaces, 2015. **7**(13): p. 7303-7314.
173. Seino, Y., et al., *High‐Performance Green Oleds Using Thermally Activated Delayed Fluorescence with a Power Efficiency of over 100 Lm W− 1.* Advanced Materials, 2016: p. 2638-2643.

174. Gong, S., et al., *Highly Efficient Deep‐Blue Electrophosphorescence Enabled by Solution‐Processed Bipolar Tetraarylsilane Host with Both a High Triplet Energy and a High‐Lying Homo Level.* Advanced Materials, 2011. **23**(42): p. 4956-4959.

175. Yang, X., G. Zhou, and W.-Y. Wong, *Functionalization of Phosphorescent Emitters and Their Host Materials by Main-Group Elements for Phosphorescent Organic Light-Emitting Devices.* Chemical Society Reviews, 2015. **44**(23): p. 8484-8575.

176. Zhou, G., et al., *Manipulating Charge‐Transfer Character with Electron‐Withdrawing Main‐Group Moieties for the Color Tuning of Iridium Electrophosphors.* Advanced Functional Materials, 2008. **18**(3): p. 499-511.

Acknowledgements

Many remarkable individuals contributed to the completion of this work over the past six years. First, my sincere thanks to Prof. Dr. Norbert Koch, who provided me the opportunity to pursue my study in the Department of Physics of Humboldt Universtät zu Berlin under his supervision. He is always pleased and patient in guiding me through my research and in sharing his wisdom and experience. In addition, he gave me the opportunity to contact other experts in the field of organic light emitting diodes all over the world. I would also like to thank Prof. Dr. Jürgen P. Rabe and Prof. Dr. Liangsheng Liao for allowing me to access the experimental facilities in their laboratories. I would also like to express my sincere gratitude to Dr. Andreas Optiz, who was very helpful in providing me good advice in both experimental and theoretical physical issues.

I would like to thank all the numbers of the SMS group and PMM group of Humboldt Universtät zu Berlin and Liao's group of Soochow University for fruitful discussions on my experimental results and for their valuable suggestions. Furthermore, my special thanks to Dr. Stefan Rehbein for patterned substrate fabrication, to Manuel Gensler for AFM measurement, to Dr. Philipp Lange for SNOM system fabrication, to Dr. Shoucheng Dong for synthesis of the host materials and to Dr. Melanie Timpel for SEM measurement. I would like to thank Henriette Strahl for all her administrative assistance. Thanks as well to Timo Florian and Paul Zybarth for maintaining the GLAD system. Thank you truly as well to all the people with whom I spent my time in labs.

Finally, I would like to thank my family and friends for their invaluable support throughout this process.

Selbstständigkeitserklärung

Hiermit erkläre ich eidesstatlich, dass ich die Dissertation selbständig und nur unter Verwendung der angegebenen Hilfen und Zitate angefertigt zu haben.

Desweiteren besitze ich keinen weiteren Doktortitel und habe mich nicht anderweitig um einen weiteren Doktortitel beworben.

Ferner erkläre ich, dass ich die Promotionsordnung der Mathematisch-Naturwissenschaftlichen Fakultät I der Humboldt-Universität gelesen und zur Kenntnis genommen habe.

Junming Li

Berlin, 27.08.2016